Studies of the High-Latitude Electric Potential Pattern in the CTIP Model with Radio Tomography Comparisons

by

Emma L. Whittick

The University of Wales, Aberystwyth
2010

THESIS
submitted to The University of Wales
by
Emma Louise Whittick, B.Sc, M.Sc (Wales), PGCE (Oxon)
In Candidature for the Degree of
PHILOSOPHIAE DOCTOR

Declaration

This work has not previously been accepted in substance for any degree and is not being concurrently submitted in candidature for any degree.

Signed . . . . . (candidate)

Date ...13/09/10... . . . . .

Statement 1

This thesis is the result of my own investigations, except where otherwise stated. Where correction services have been used, the extent and nature of the correction is clearly marked in a footnote(s). Other sources are acknowledged by footnotes giving explicit references. A bibliography is appended.

Signed . . . . . (candidate)

Date ...13/09/10... . . . . .

Statement 2

I hereby give consent for my thesis, if accepted, to be made available for photocopying and for inter-library loan, and for the title and summary to be made available to outside organisations.

Signed . . . . . (candidate)

Date ...13/09/10... . . . . .

E-thesis Deposit Agreement

I hereby give consent for my thesis, if accepted, to be deposited in the University's Institutional Research Repository.

Signed . . . . . (candidate)

Date ...13/09/10... . . . . .

Summary

This thesis explores the use of high-latitude electric potential patterns obtained from the Super Dual Auroral Radar Network (SuperDARN) as input to the Coupled Thermosphere Ionosphere Plasmasphere (CTIP) model. By using a new method of high-latitude convection input it is shown that some improvements to the modelling of the spatial distribution of the electron density can be obtained.

In the earlier versions of the CTIP model the high-latitude electric potential input was selected from a restricted library of convection patterns. By introducing the SuperDARN electric potential data as the high-latitude input it is now possible to model a wide range of different convection patterns, notably patterns occurring as a result of Interplanetary Magnetic Field (IMF) B_z positive conditions. In order to begin to validate the use of this technique, images obtained from ionospheric radio tomography experiments were used to form case studies involving periods of time where the IMF B_z component was either stable and positive or stable and negative. This enabled the ion densities from the tomography images to be compared to the ion densities obtained from the CTIP model output. Initially this was done with two case-studies that had mature interpretations in order to prove that the concept of using SuperDARN convection patterns in CTIP was valid. Subsequent case-studies involved using the model with the new convection pattern input method to assist with the interpretation of the tomography images obtained from the Alaskan sector.

This work is dedicated to
Mum & Dad

Acknowledgments

I would like to thank Dr. S. E. Pryse for her supervision of this research project and the Particle Physics and Astronomy Research Council (PPARC) for financial support. Thanks are also due to members of the Solar System Physics group at Aberystwyth, in particular Dr A. Breen and Dr. D. S. Brown.

The following individuals and organisations have assisted me with the provision of data: Dr. J. Secan at NorthWest Research Associates for the provision of the Alaskan radio tomography data, Dr. N. Ness at the Bartel Research Institute for provision of ACE data, via the CDAWeb and The World Data Centre for provision of geomagnetic indices. I would also like to thank Prof. A. D. Aylward at University College London for a number of productive meetings regarding the Coupled Thermosphere Plasmasphere Model.

Contents

Chapter 1

Introduction

The structure of the plasma in the ionosphere at high-latitudes follows from a complex chain of physical interactions that link the outer regions of the Sun and the Earth's atmosphere. The solar wind carries the interplanetary magnetic field that interacts with the Earth's magnetic field to open the terrestrial environment to space-weather effects. The coupling process itself covers vast regions of space, however due to the convergence of the Earth's magnetic field lines near the poles this region essentially maps down to the high-latitude ionosphere. Therefore, investigating the footprints of these interactions in the high-latitude ionosphere enables the coupling process to be understood more clearly. An overview of the high-latitude ionosphere is given in Chapter 2.

This thesis uses the Coupled Thermosphere Ionosphere Plasmasphere (CTIP) model to interpret ionospheric radio tomography data from several chains in the International Ionospheric Tomography Community (IITC). Chapter 3 outlines the main instruments used to obtain data for these studies, in particular, the technique of ionospheric radio

tomography. Chapter 4 is an overview of the CTIP model.

All of the case studies presented were chosen because the tomography passes were obtained during a period of time where the IMF B_z component was either stable and negative or stable and positive for a number of hours prior to the time of interest. By choosing a series of radio tomography passes from times where the IMF was stable, it is possible to identify a representative high-latitude electric potential pattern for that time. The most important work in this thesis is the use of data from the Super Dual Auroral Radar Network (SuperDARN) as the high-latitude input for the CTIP model. This has vastly expanded the range of high-latitude input available to CTIP, in particular the modelling of the plasma distribution under the conditions of IMF B_z positive. The theory of this development to the model is described in detail in Chapter 5. Chapter 6 contains a series of case studies with mature interpretations that aim to verify that the model results obtained using SuperDARN data are valid, using other instruments to assist with the interpretation. Chapter 7 extends this work to look at case studies from the Alaskan tomography chain where there is less additional instrumentation available to aid interpretation of the data and therefore the conclusions drawn rely heavily on the new model developments, especially with regard to interpreting the cause of the plasma distribution under the condition of IMF B_z positive. Finally, Chapter 8 offers some conclusions to this work together with some areas for further study.

Chapter 2

Overview of the High-Latitude Ionosphere

2.1 Introduction

The ionosphere consists of a weakly ionised plasma with about 1% ionisation of the neutral atmosphere. In terms of altitude it extends from around 60km upwards to the outer reaches of the Earth's environment. The ionosphere is important because it significantly influences the propagation of radio waves and therefore understanding its properties is crucial to the operation of navigation devices such as the Global Positioning System (GPS) for navigation and communication radio systems. The ionosphere is considered to comprise four main regions with the following properties in the daytime: The D region exists from about 60 – 90km and has electron densities of about 10^8 – 10^{10} electrons m^{-3}. The E region ranges from 105 – 160km with densities of

about 10^{11} electrons m^{-3}. The F region is divided into two layers, F1 and F2. The F1 layer stretches from $160-180$km with densities of $10^{11}-10^{12}$ electrons m^{-3} with the F2 layer at altitudes above this, reaching a maximum density at about 300km of the order of 10^{12} electrons m^{-3}. At night time, the D and E regions and the F1 layer generally vanish as they are controlled strongly by solar radiation, although some ionisation may persist in the E region known as sporadic E. The F2 layer persists at a much reduced intensity. The ionosphere eventually merges with the protonosphere at an altitude of about 1000km where H^+ is the dominant ion. In the evening the protonosphere drops in altitude leading to charge exchange between the H^+ and ionospheric O^+ contributing the maintaining of the F2 layer at nighttime. Figure 2.1 (Rees, 1989) shows a diagram of the day and night time variation of the electron density in the ionosphere for both solar maximum and minimum.

The vertical distribution of ionisation is governed primarily by the continuity equation that relates the electron density, to production, loss and transport:

$$\frac{\partial N}{\partial t} = q - L - div(N\boldsymbol{v}) \tag{2.1}$$

where $\frac{\partial N}{\partial t}$ is the rate of increase of the electron density with respect to time, q is the production rate of ionisation, L is the loss rate by recombination and $div(N\boldsymbol{v})$ is the rate of loss of ionisation due to transport of plasma, where N is the electron density and $\boldsymbol{v}$ is the mean drift velocity of the plasma. The different processes governing these equation components are outlined below:

2.1.1 Production Processes

Ionisation by solar Extreme Ultra Violet (EUV) radiation is one of the main production mechanism at mid latitudes and is also known as photoionisation. The production rate, q, of solar radiation is proportional to the density of neutral species, n, and the intensity of the incoming radiation, I is given by Equation 2.2:

$$q = \eta\sigma nI \tag{2.2}$$

In order that an atom or molecule is ionised, it must first absorb radiation. The amount of radiation absorbed is expressed by the absorption cross-section, σ. However not all the radiation absorbed by the molecule or atom will go into the ionisation process; this is taken into account by the coefficient η which is the ionisation efficiency, or the fraction of the absorbed radiation that goes into producing ionisation.

From Equation 2.2, S. Chapman developed a formula to predict the form of an ionospheric layer and how it varies throughout the day. The rate of production of ionisation q is known as the Chapman Production Function. Chapman makes four assumptions:

1. The atmosphere is composed of a single species, exponentially distributed with the scale height, H, constant where H is defined by Equation 2.3

$$H = \frac{kT}{mg} \tag{2.3}$$

where k is Boltzman's constant, T is the temperature of the material in Kelvin, m is the mass of the gas and g is the acceleration due to gravity.

2. There is no variation in the horizontal plane

3. Solar radiation is absorbed in proportion to the concentration of gas particles as in Equation 2.2

4. The absorption coefficient η is constant, or equivalently the radiation is monochromatic, having only one wavelength

Equation 2.2 can be normalised to take into consideration the scale height of the ionosphere (Hargreaves, 1992):

$$q = q_0 \exp^{(1-z-\sec\chi\cdot\exp^{-z})} \tag{2.4}$$

where q_0 is the maximum production rate, χ is the solar zenith angle and z, the reduced height of the neutral gas defined as

$$z = \frac{h - h_{mo}}{H} \tag{2.5}$$

with h being the height of interest of the neutral gas and h_{mo} is the height of maximum production rate when $\chi = 0$ which is equivalent to the Sun being directly overhead. Essentially, as χ decreases, q increases for a given z. Thus according to Chapman theory, the sunlit pole in the summer and the dark pole in the winter leads to greater ionisation production in summer than winter. There are three well-known seasonal variations in the ionosphere which affect the electron density. The winter or seasonal anomaly refers to electron densities in the F2 layer at noon being greater in winter than the summer electron densities (Croom et al., 1960). It is thought that this anomaly can be attributed to seasonal changes in the chemical composition in the neutral air (Zou et al., 2000).

In the F2 layer, the production of ions depends on the concentration of atomic oxygen whereas the loss of ions depends on the concentration of molecular nitrogen and molecular oxygen. A higher atomic-molecular ratio in the winter months could account for some of the differences in the electron density. The second anomaly is that the electron density in December is about 20% greater than that in June, which is known as the annual anomaly. Approximately 6% of the difference is attributed to the elliptic nature of the Earth's orbit around the Sun, meaning that the Earth is not always equidistant from the Sun leading to a variation in the intensity of solar radiation. Finally, the semiannual anomaly is when the maximum electron density peaks around the equinoxes and the minimum electron density occurs around the solstices. There have been several suggestions as to the cause of the semiannual anomaly (Zou et al., 2000) including the influence of the solar wind, increased internal thermospheric mixing at the solstice and the large off-set of the geographic and geomagnetic poles in the southern hemisphere, combining with effects of the variability of the solar zenith angle. This last idea was addressed by Millward et al. (1996b) in a paper discussing the seasonal and semiannual variations in the F2 layer.

The other main production process is particle precipitation where energetic particles gyrate down geomagnetic fields and collide with neutral atoms and molecules in the ionosphere. Magnetospheric - ionospheric coupling causes the precipitation of electrons and ions into the ionosphere, causing plasma production in the high-latitude ionosphere. The rate at which the precipitated particles move through the ionosphere was studied by Millward et al. (1999) using the Sheffield High-Latitude (SHL) model. Figure 2.2 shows

the modelled height profiles of the ionisation produced by monoenergetic electrons and Figure 2.3 shows a similar plot for monoenergetic ions. From these plots it can be seen that the greater the energy in either the electrons or ions, the greater the amount of ionisation, with the maximum amount of ionisation produced at a lower level For the F2 layer, typical electron and ion energies would be at least $200eV$. Energies lower than this would not be sufficient to penetrate the F-layer.

2.1.2 Loss Processes

The main loss process in the ionosphere is due to chemical recombination

$$X^+ + Y_2 \rightarrow YX^+ + Y \tag{2.6}$$

$$YX^+ + e \rightarrow Y + X \tag{2.7}$$

This two-stage process is known as disassociative recombination. In the F2 layer, X^+ is predominantly O^+ and Y_2 is either molecular Oxygen O_2 or molecular Nitrogen N_2. The recombination rates of each of the stages in the disassociative recombination reactions are dependent on $\beta[X^+]$ for Equation 2.6 and $\alpha[YX^+]N$ for Equation 2.7 where α is the coefficient of recombination and β is the attachment coefficient, the brackets [] indicates the number densities of the species and N is the electron density. Essentially in the F-region, the first part of the reaction, (Equation 2.6) has a slower reaction rate than Equation 2.7, implying that the overall recombination rate is determined by the

concentrations of X^+ and Y_2. Furthermore, these reactions are temperature sensitive; the rate of reaction is dependent on the effective temperature of the reaction which is governed by both the ion temperature and ion velocity.

2.1.3 Transport

The transport aspect of Equation 2.1 explains the convection of ionisation both into and out of the region of interest. There are two main mechanisms in the high-latitude ionosphere, namely neutral winds and electric fields. At heights below the F-region peak, the collision frequency between the neutrals and the ions is high so the plasma transport is mainly controlled by the neutral winds. The neutral winds push ionisation up or down the magnetic field lines as winds flow equatorward or poleward. However, at F-region heights, the collision frequency between the ions and the neutrals is much smaller and the electric fields control the plasma motion. This motion is controlled by the interaction of free charged particles with the electric field ($\boldsymbol{E}$) and the magnetic field ($\boldsymbol{B}$) through the Lorentz force described in Equation 2.8:

$$\boldsymbol{F} = q(\boldsymbol{E} + \boldsymbol{v} \times \boldsymbol{B}) \tag{2.8}$$

where $\boldsymbol{F}$ is the Lorentz force, q is the electric charge and $\boldsymbol{v}$ is the plasma velocity, resulting in a plasma drift perpendicular to the electric field (Brekke, 1997).

As described by Schunk (2000), ion outflow, where an upward flow of ionospheric ions are moved into the magnetosphere is another transport mechanism that is important at high latitudes.

2.2 Near-Earth and Interplanetary Space Coupling

The Earth's environment is strongly influenced by its interaction with interplanetary space which impacts upon the ionosphere. Overviews of these processes can be found in text books, e.g. Hargreaves (1992).

2.2.1 Solar Wind

The solar wind was discovered by Parker (1958). It consists of a continual stream of predominantly protons (H^+ particles) emitted radially from the solar corona. At the distance of the Earth's orbit the average speed of the solar wind is $200 - 800 kms^{-1}$. The solar wind is the main way in which the activity of the Sun is communicated to the vicinity of the Earth. Consequently it is very important when considering solar-terrestrial relations. The interaction between the solar wind and the near earth environment is characterised by the weak magnetic field carried along by the solar wind plasma known as the Interplanetary Magnetic Field (IMF). This field is frozen into the solar wind plasma because of the large electrical conductivity of the plasma. The IMF, which originates at the Sun is dragged outward by the solar wind sweeping past the planets. The components of the IMF are usually expressed as $\boldsymbol{B_x}, \boldsymbol{B_y}, \boldsymbol{B_z}$ where the Cartesian co-ordinate system is the Geocentric Solar Magnetospheric (GSM) system, i.e. the Earth-to-Sun is the x-axis, the z-axis parallel to the Earth's magnetic dipole and y-axis is positive in the duskward direction.

2.2.2 Magnetosphere

The magnetosphere is the cavity formed when the solar wind meets the geomagnetic field. Figure 2.4 (Hargreaves, 1992) shows a simplified diagram of the magnetosphere as seen from the dawn-dusk meridian. The solar wind is unable to penetrate the geomagnetic field so it is swept around it, forming a bow shock and distorting the dipole magnetic field of the Earth. On the sunward side, the dipole is compressed by the solar wind; on the nightside the field is extended forming a magnetotail due to the solar wind flowing anti-sunward from the Earth. Basic models of the magnetosphere predict two neutral points on the boundary between the magnetosphere and the solar wind where the total magnetic field is zero. These points connect at about ±78°MLAT to the Earth's surface via field lines. At these regions, known as polar cusps, solar wind particles can enter the magnetosphere without having to cross field lines.

2.2.3 Viscous Interactions

It was suggested by Axford and Hines (1961) that momentum is transferred from the solar wind into the magnetosphere by means of viscous interactions which cause the whole system to circulate. Typically this circulation process involves the positive ions moving with the neutral air while the magnetic field carries the electrons. This results in the magnetic field lines circulating over the poles from the day to the night sectors of the Earth with the return flow around the dawn and dusk sides.

2.2.4 Reconnection

An alternative mechanism for solar wind-Earth coupling is magnetic reconnection. This coupling process is known as the Dungey Cycle (Dungey, 1961) and explains how the Interplanetary Magnetic Field interacts with the Earth's geomagnetic field. The key component of the IMF for this process is its B_z component, though the B_y and B_x components also have an effect on the reconnection (Cowley, 1998). With a southward IMF, (i.e. $B_z < 0$), neutral points are formed in the equatorial plane with the IMF connecting to the geomagnetic field near the plane. As the IMF is frozen into the solar wind and therefore carried along with it, the field lines are dragged across the polar cap from the dayside to the nightside. A second reconnection site occurs in the magnetotail when the geomagnetic field and the IMF are separated. In consequence, field lines over the poles are open in the sense that they do not link with the other hemisphere. With northward IMF (i.e. $B_z > 0$) the neutral points are in the solar-ecliptic plane so that the reconnection sites occur in the lobe regions, as shown in Figure 2.4.

2.2.4.1 Reconnection under IMF Bz Southward

When the IMF B_z component has a negative or southward component then reconnection can occur near to or at the the equatorial magnetopause, as shown in Figure 2.5 (Lockwood, 1995). As the magnetic field lines of the IMF meet with the magnetic field lines of the magnetopause, the field lines merge or reconnect at the reconnection site (marked by X in Figure 2.5) causing the newly reconnected field lines to be accelerated away from the reconnection site by a magnetic tension force. This results in the field

lines being stretched out into the magnetotail by the anti-sunward flow of the solar wind as illustrated by field lines 2-5. A further reconnection takes place in the magnetotail, closing the field lines (not shown in figure). A magnetic tension force pulls the field lines Earthwards and round to the dayside. The ionospheric signature of this process is a symmetrical two-cell pattern of F-region plasma flow which can be identified by in-situ or ground-based instruments. The plasma motion or convection becomes more complicated when other components of IMF are considered, most particularly a non-zero IMF B_y. When IMF $B_y < 0$, the resulting effect on the convection cells is for the dawn cell to be reduced in size while the dusk cell forms an expanded crescent shape, where the convergence of the anti-sunward flow enters in the pre-noon sector. The reverse is true for IMF $B_y > 0$ where the flow convergence enters in the post-noon sector and the polar cap is dominated by the crescent-shaped dawn cell. The top panel of Figure 2.6 (Cowley et al., 1992) shows a schematic of the ionospheric convection patterns for IMF B_z negative with three different B_y scenarios taken from Cowley (1998). These diagrams are generic views of the effect of IMF B_y component on IMF $B_z < 0$ that have been condensed from may periods of ground and space-based observations. Each diagram is drawn as seen from the northern polar region in a fixed magnetic latitude (MLAT) - magnetic local time (MLT) frame. The Earth rotates under this fixed frame with the 12MLT (Magnetic noon) facing sunwards at the centre of the dayside and the 24MLT (magnetic midnight) on the nightside. For the European sector observations that are discussed in this thesis, magnetic noon occurs at around 0900UT.

2.2.4.2 Reconnection under IMF Bz Northward

When the IMF B_z component has a positive or northward direction then the reconnection site can be at a lobe of the geomagnetic tail. Figure 2.7 (Lockwood, 1995) shows the evolution of the field lines following a lobe reconnection event. In this configuration the open field lines follow a path through points 1 to 6 which results in the formation of two convection cells rotating anti-clockwise and clockwise within the polar cap. Under these conditions the open polar cap region is bounded by an adiaroic boundary between open and closed field lines across which there is no transfer of magnetic flux. The magnetic tension force initially pulls the field lines sunward before they are returned to the geomagnetic tail by the anti-sunward flow of the solar wind. As described in Crooker (1992), different configurations of IMF B_z northward reconnection are possible. Indeed both lobe and magnetopause reconnection may occur simultaneously (Cowley, 1998). The bottom panel of Figure 2.6 shows some suggested scenarios of inferred plasma flow for different IMF B_y conditions, though these 4-cell patterns that are depicted in the diagrams may not always be representative of the true plasma motion (Ruohomiemi and Baker, 1998). Depending on the direction of B_y, there may be two lobe cells of circulation within the polar cap as shown in Figure 2.6. However it is thought that a single lobe cell may be prevalent during periods where $B_y \gg 0$ (for example, Ruohomiemi and Baker (1998)). Outside the polar cap region, crescent-shaped viscous cells are depicted on the dawn and dusk flanks of the polar cap. These are thought to represent flow cells located wholly on closed field lines.

2.2.4.3 Effect of IMF B_x on Reconnection

Very little is known about the effect of IMF B_x on reconnection. It is thought that a negative B_x gives rise to reconnection in the northern hemisphere lobe whereas a positive B_x component favours reconnection with the southern hemisphere lobes (Crooker, 1992).

2.2.4.4 Clock Angle and Reconnection

The clock angle is a useful parameter for categorising the IMF B_y and B_z components. It is defined as

$$\arctan \frac{\mid By \mid}{Bz} \tag{2.9}$$

for IMF B_z positive, and

$$180^\circ - \arctan \frac{\mid By \mid}{Bz} \tag{2.10}$$

for IMF B_z negative. Clock angles greater than 90° correspond to IMF B_z negative and are associated with equatorial reconnection. Clock angles less than 90°, corresponding to IMF B_z positive are generally associated with lobe reconnection. However, for clock angles between approximately 45° and 90° which corresponds to B_z positive and $\mid B_y \mid > B_z$, it has been suggested by Sandholt et al. (1998) that both lobe and equatorial reconnection could occur simultaneously.

2.3 Particle Precipitation

As outlined in Section 2.1.1, particle precipitation is a mechanism whereby ionospheric ionisation is created in-situ. The magnetosphere provides the source of particles which precipitate into the ionosphere. The location of this source in the magnetosphere directly influences the energy and number density of the particles, which in turn determines the energy and flux of the particles as they precipitate. Siscoe (1991) identified the principal regions of the magnetosphere as shown in Figure 2.8. The cusp region is where the plasma has direct entry into the ionosphere following the reconnection process. Tailward of the cusp is mantle plasma comprising de-energised magnetosheath plasma. Equatorward of the cusp is a region known as the lower-latitude boundary layer (LLBL). Surrounding the earth is the plasma sheet (PS), which extends down the magnetotail and is bounded by the plasma sheet boundary layer (PSBL) and the LLBL. The boundary plasma sheet (BPS) includes the plasma sheet boundary layer and a part of the plasma sheet. However, the central plasma sheet (CPS) is the part of the plasma sheet that excludes the BPS. These magnetospheric regions have been related to observed particle precipitation using the Defence Meterological Satellite Programme (DMSP) satellites to record and categorise precipitating particles according to energy and particle flux (Newell and Meng, 1992).

2.3.1 Aurora

The aurora is the optical manifestation of the precipitation of energetic particles into the ionosphere. Electron and ion precipitation into the ionosphere excites neutral at-

mospheric species which emit photons as they return to their ground state. Typical locations are poleward of 75°MLAT dayside and 70°MLAT on the nightside under quiet conditions. However in disturbed conditions the aurora can extend to as low as 60°MLAT and can be visible in the UK. The auroral emissions have been classified according to their magnetospheric source by Sandholt et al. (1998).

2.4 Density Enhancements and Depletions

A variety of plasma density enhancements and depletions can be found in the ionosphere. Some of these are detailed below.

2.4.1 Density Enhancements

Density enhancements fall into three categories based on location: those located inside the polar cap, those located outside the polar cap e.g. boundary blobs (Crowley, 1996) and those located within the cusp region.

2.4.1.1 Cusp Region

The cusp is the region of direct entry of solar wind particles into the polar cap. Here soft precipitation causes F-region density structure. Processes in this region depend on IMF orientation as this affects the location of the reconnection site and high-latitude convection (Smith et al., 2000; Pryse et al., 2000).

2.4.1.2 Polar Patches and Tongue-of-Ionisation

Polar patches are regions of enhanced F-region electron density which are observed mainly under IMF southward conditions. In an extensive review of polar cap plasma, Crowley (1996) defined a polar patch as where the enhancement is at least twice the density of the background level. Patches are not produced by in-situ precipitation (Weber et al., 1984), rather they are transported by the tongue-of-ionisation (TOI) and anti-sunward convection, which is an effect of IMF orientation. Patches have horizontal scales of the order of 100km-1000km and are moved at speeds of up to around $1000 ms^{-1}$.

2.4.1.3 Auroral Arcs

Auroral arcs are an optical feature observed within the polar cap under the IMF northward conditions (Buchau et al., 1983). Small arcs have lengths of the order of 100km and large arcs of about 1000km with widths being around 100km. They are formed by soft particle precipitation (i.e. energies less than 500eV) and are associated with enhanced electron densities.

2.4.1.4 Blobs

There are three types of blobs, depending on the location: sub auroral, boundary and auroral. Boundary blobs are found outside the polar cap. Tsunoda (1987) and Schunk and Sojka (1996) have suggested that the equatorward edge of the auroral oval could be the poleward wall of the main trough. There are two suggested production mechanisms:

Rino et al. (1983) suggested soft precipitation near equatorward edge was the cause but de la Beaujardiere et al. (1985) suggested that long-lived plasma could be convected across the polar cap. Sub auroral blobs are equatorward of boundary blobs (Tsunoda, 1987; Schunk and Sojka, 1996) whereas auroral blobs are to be found within the latitudinal constraints of the auroral latitudes. Crowley (1996) suggests that they are formed by precipitation.

2.4.2 Density Depletions

Density depletions in the ionosphere essentially comprise troughs and polar holes. They have different names depending on the author (Rodger et al., 1992).

2.4.2.1 Trough

The main trough occurs at sub-auroral latitudes though it could occur at high latitudes on the dayside. It is more predominant on the night-side and referred to as the mid-latitude trough, observed from around 18-09UT and located between $50-60^{\circ}$MLAT under quiet geomagnetic conditions, (Kersley et al., 1997). It moves equatorward with increasing Magnetic Local Time (MLT) and increasing geomagnetic activity as observed by Kersley et al. (1997) and Pryse et al. (2000).

2.4.2.2 Polar Hole

A polar hole is a particular high latitude trough that is formed by stagnation of plasma in the dark winter ionosphere (Brinton et al., 1978). More recent observations have been detailed in Kersley et al. (1997).

2.5 Conclusion

The sections of this chapter have introduced the basic processes that govern the structure of the high-latitude ionosphere. Ionisation can be created by solar radiation and/or through the impact of particles entering the upper atmosphere as a result of some type of coupling or disturbance of the Earth's magnetic environment, such as particle precipitation or reconnection. Interactions between the IMF and the magnetosphere cause plasma convection in the polar cap. In addition, detectable signatures of localised enhancements and depletions of plasma in the polar regions can be used to as a diagnostic tool for investigating the effects of particular orientations the IMF has on the ionospheric structure.

Chapter 3

Instrumentation

3.1 Introduction

The instruments described in this chapter have been used in two ways: some have been used to provide input parameters for subsequent modelling work and others have been used to interpret and validate the model results obtained, most notably the Ionospheric Radio Tomography experiment which was used to provide measurements of the ionospheric electron content.

3.2 Tomography

Kak and Slaney (1987) defined tomography as "the cross-sectional imaging of an object or parameter using the data collected by the illumination of the target from many different directions". A large number of one-dimensional projections are combined in a reconstruction algorithm to produce a tomographic image of the object or parameter.

Radon (1917) was the first person to solve the mathematical problem of reconstructing a function from its separate projections though it was not until the more wide-spread use of computers that the importance of this technique in both medical and scientific applications was realised. Godfrey Houndsfield developed the first computer-aided tomography (CAT) scanner in 1972 which was designed to measure the attenuation of X-rays through the human body form a wide range of angles. After applying tomographic reconstruction technique a two-dimensional image of the section of the area of the body under investigation was produced. Other applications of radio tomography include oceanography and in the seismic surveying of the Earth's structure but the main geophysical interest for this thesis is in probing the upper atmosphere.

3.3 Ionospheric Radio Tomography

Radio tomography is a technique used to image the large-scale spatial distribution of ionospheric electron density on horizontal scales of tens to hundreds of kilometers. The technique involves measuring the line integral of electron density between a satellite and a receiver station. This gives what is known as the Total Electron Content (TEC). Many such measurements are taken over a large number of intersecting satellite to receiver ray paths and these data are inverted to produce a spatial distribution of electron density over the region of interest, which is determined by the location of the ground receiver stations. Mathematically the total electron content I_s is defined as the line integral of the electron density along a radio-wave propagation path from a satellite, S, to a receiver, R. The TEC may be expressed by Equation 3.1.

$$I_S = \int_S^R N(r, \theta, \phi)\, ds \tag{3.1}$$

where N is the electron density, r is the radial distance from the centre of the Earth, θ is the latitude, ϕ is the longitude and s is the distance along the satellite to receiver ray path.

The first proposed use of tomography in ionospheric physics was detailed by Austen et al. (1986) which presented a method involving the use of radio transmissions from the Navy Navigational Satellite System (NNSS) now known as Navy Ionospheric Monitoring System (NIMS) to get a 2D image of the ionosphere. Currently, other satellites are now available, e.g. ARGOS, GFO, Radcal and PICOsat. The International Ionospheric Tomography Community (IITC) has had a number of chains of receiver station spaced out across the globe. Those used in this study are located in the UK, Scandinavia, Alaska and Greenland. The first experimental tomography image was presented by Andreeva et al. (1990) and the first study whereby ionospheric radio tomography was verified by incoherent-scatter radar was detailed by Pryse and Kersley (1992). A review of the early tomography experimental results was presented by Kersley and Pryse (1994). A more recent overview of the capabilities and potential of radio tomography was given by Pryse (2003).

One of the main difficulties with ionospheric radio tomography is the reconstruction of the vertical electron density profile. This is because of the necessary geometry with the satellites being above the ionosphere and the receiver stations being below it, which results in the lack of near-horizontal ray paths and limits the information on the

ionospheric structures. The electron density of the vertical profile is consequently less reliable than the horizontal distribution. To counter this, a priori information is inserted into the reconstruction as described by Raymund et al. (1990), which highlighted the importance of a background ionosphere. There are three main types of tomographic algorithm: iterative, quadratic optimisation and non-iterative. Iterative algorithms include the Simultaneous Arithmetic Reconstruction Technique (SART) (Austen et al., 1986) and the Multiplicative Algebraic Reconstruction Technique (MART) (Raymund et al., 1990). These methods involve the use of a tomographic grid covering the region of ray path intersections whereby the electron densities can be obtained by weighting the TEC between the pixels intersected by a particular ray path in proportion to the length of the ray path within that pixel. Quadratic optimisation algorithms include methods such as the Simultaneous Iterative Reconstruction Technique (SIRT), (Austen et al., 1988; Pryse and Kersley, 1992; Pryse et al., 1993) and more recently Spencer et al. (1998). Non iterative techniques, for example the Discrete Inversion Theory (DIT) (Fremouw et al., 1992, 1994), with a subsequent extension by Pryse et al. (1998a) incorporated a second stage which used a MART algorithm to image small-scale features.

A comparison of these different tomographic methods and algorithms can be found in Raymnund (1995). The need for a background ionosphere was highlighted by Raymund et al. (1990) with the use of a back-projected Chapman layer. Pryse et al. (1998b) showed that careful choice of a priori information to initialise the reconstruction procedure may be as important as the actual method used to perform the inversion. Further developments to the radio tomography technique incorporated the use of data from the

International Reference Ionosphere (IRI) model (Bilitza, 1990; Raymund et al., 1993), ionosonde data (Kersley et al., 1993) to provide spot-values for ionospheric densities with topside profiles developed by Heaton et al. (1995).

3.3.1 Aberystwyth University Ionospheric Radio Tomography Experiment

The Aberystwyth University ionospheric radio tomography experiment was deployed in Summer 1996 and consists of a chain of 4 satellite receiver stations located in Northern Scandinavia. Figure 3.1 shows the location of the respective stations, with Ny-Ålesund and Longyearbyen in Svalbard at 78.9°N, 11.9°E and 78.2°N, 15.3°E respectively, Bjørnøya at 74.5°N, 19.0°E and Tromsø at 69.8°N, 19.0°E in northern Norway. The chain of stations receive signals from polar orbiting satellites of the Navy Ionospheric Monitoring System (NIMS) which are formerly known as the Navy Navigational Satellite System (NNSS). These satellites move in an approximately polar orbits at an altitude of about 1100km. The satellites transmit two phase-coherent signals with the lower frequency of about 150MHz which is three-eights of the upper frequency of 400MHz. The satellites do not pass directly overhead of the chain line due to the Earth's orbital motion and the chain line not being exactly in a straight line. To account for this, Mitchell et al. (1997) developed a longitude correction whereby the longitudinal component of the measured TEC is removed by projecting the measurements onto the vertical plane. However if a large longitudinal gradient exists this correction factor may still be insufficient to compensate for the longitudinal offset of the satellite. This is

why high-elevation ($\geq 40^{\circ}$) passes are chosen; other passes of lower elevation ($30-40^{\circ}$) can be useful but need to be treated with caution.

3.4 DMSP

The Defence Meteorological Satellite Programme (DMSP) monitors meteorological, oceanographic and solar-terrestrial environments. It consists of a number of satellites in near polar, sun, synchronous orbits at an altitude of approximately 830km with an orbital period of about 101 minutes. The Special Sensor-Ions, Electrons, and Scintillation (SSIES) instruments aboard all the satellites enables the cross-track plasma drift to be obtained. A polar plot of the ion density and the satellite's path is useful for obtaining the amount of ions present at a particular time. This can be compared with the SuperDARN convection pattern to infer information about the location of the ion densities in the polar cap.

3.5 ACE

The Advanced Composition Explorer (ACE) spacecraft is designed for studying and monitoring the interplanetary medium. ACE orbits the L1 libration point, which is a point of Earth-Sun gravitational equilibrium situated about 1.5 million kilometers from Earth and 148.5 million kilometers from the Sun. For this study the MAG instrument has been used to obtain the vector components of the Interplanetary Magnetic Field.

3.6 SuperDARN

Super Dual Auroral Radar Network (SuperDARN) is an international radar network for studying the Earth's upper atmosphere, ionosphere and connection into space. It consists of 12 HF radars in the Northern Hemisphere and 7 in the Southern Hemisphere. Each radar is made up of a primary array of 16 antennae and an interferometer array of 4 antennae. Each individual radar can be electronically steered to one of 16 different beam directions enabling a large geographical area to be covered. The radars transmit a sequence of pulses and the returning echoes are sampled. This enables three main parameters to be determined: the back-scattered power, spectral width and the Doppler velocity of the plasma density irregularities in the ionosphere. Usually, for each 3.25° beam, 75 spatial ranges are resolved with a 45km separation (Greenwald et al., 1995; Chisham et al., 2007). The convection pattern is reconstructed using SuperDARN data to find a functional form for the distribution of electrostatic potential in the ionosphere which bests fits all the line-of-sight velocity measurements available at the time of interest (Ruohomiemi and Baker, 1998). Figure 3.2 shows an example of such a reconstruction with the contours of constant electrostatic potential shown by the solid and dashed black lines. These lines also represent the flow streamlines and the small black arrows represent the individual velocity vectors. The velocity measurements are supplemented by the use of data from the model developed by Ruohomiemi and Greenwald. The IMF orientation and magnitude at the magnetopause at the time of interest determines the choice of model data, which are weighted so that the impact of the modelled data is minimised over the real data. Continual developments in the SuperDARN network

reduces the reliance of the maps on the model data. Global convections maps can be generated at one or two minute resolution of the radar scans. This resolution is suitable for observing the ionospheric convection changed in the solar wind and the IMF. Some of these data plots at 10-minute resolution are available on the SuperDARN website (`http://superdarn.jhuapl.edu/`).

3.7 Conclusion

While the main instrumentation used in this thesis is the ionospheric radio tomography experiment, the other instruments are used to assist the interpretation of the electron density distribution in the observed images. Further, the CTIP model requires certain parameters obtained by these instruments, notably the high-latitude electric potential pattern data from SuperDARN.

Chapter 4

The CTIP Model

4.1 Introduction

The Coupled Thermosphere Ionosphere Plasmasphere (CTIP) model is a computer model of the global higher atmosphere consisting of three separate components which run concurrently, a global thermosphere model, a high-latitude ionosphere model and a mid and low latitude ionosphere/plasmasphere model. The three are fully coupled with respect to energy, momentum and continuity. The model is based upon many magnetic flux tubes which gives it its global coverage, with open flux tubes providing the framework for the high-latitude ionosphere component. The model provides a time-dependent three-dimensional structure of neutral wind vectors and temperature, the number density of the three major neutral species, O, O_2 and N_2 and the mean molecular mass. For the ions, H^+, and O^+ number densities and temperatures are determined over a height range from $100 - 10,000$km with the parameters for N_2^+, O_2^+ and

N^+ being determined below 400km. The height and number density of the ionospheric F2 peak is also determined.

4.2 Model History and Development

The CTIP model was developed from three separate models, the University College London (UCL) Thermosphere model (Fuller-Rowell and Rees, 1980), the Sheffield University ionospheric model (Quegan et al., 1982) and the Plasmasphere model (Bailey, 1983).

The UCL thermosphere model is a global, non-linear, time-dependent thermospheric model which includes the thermosphere's response to geomagnetic forcing with a polar convective field using the global, empirical ionospheric model developed by Chiu (1975). This model has no terms relating to the high-latitude response to geomagnetic activity therefore the model is limited to low geomagnetic activity because the global energy budget is insufficient at times of moderate geomagnetic activity.

The Sheffield University ionospheric model provides a representation of the behaviour of the ionised atmosphere at high and mid latitudes, including the interaction between the solar photoionisation, auroral precipitation, plasma convection and thermospheric chemistry and dynamics. This is achieved by solving equations of continuity and momentum for O^+ and H^+ ions within the high-latitude ionosphere and mid-latitude plasmasphere. The coupling of the UCL thermospheric and Sheffield ionosphere model is described by Quegan et al. (1982) and Fuller-Rowell et al. (1984). Fuller-Rowell et al. (1984) compared this coupled model with the original UCL thermospheric model

in terms of electron density, ion drag and neutral winds at high latitudes and established that the stand-alone UCL thermospheric model was unable to predict the asymmetry seen within the auroral oval, whereas the coupled model was able to predict an asymmetry. This illustrated the importance of a self-consistent ionosphere within the thermospheric model.

The UCL thermosphere and the Sheffield ionosphere are collectively known as the Coupled Thermosphere Ionosphere Model or CTIM (Fuller-Rowell et al., 1987). More recently the Chui low-latitude ionosphere model was replaced by a new low and mid latitude ionosphere and plasmasphere model (Millward et al., 1996a) which was based in an earlier model of Bailey (1983). The low latitude ionosphere was further modified to include the low-latitude drifts such as those observed at the Jicamarca radar (Millward et al., 2001). In this form the new model is known as the Coupled Thermosphere Ionosphere Plasmasphere (CTIP) model (Millward et al., 1996a).

4.2.1 Thermospheric Code

The thermospheric element of the CTIM model is designed to simulate the time-dependent structure of the wind vector, temperature and density of the neutral atmosphere. This is achieved by the numerical solution of non-linear equations of momentum, energy and continuity on a three dimensional grid of latitude, longitude and pressure. The resolution of the model is 2° in latitude, 18° in longitude with a vertical pressure distribution of 15 levels divided logarithmically from a lower boundary of 1Pa at an altitude of 80km. The upper vertical boundary varies in altitude depending on the temperature

profile but typically is within the range of $300 - 700$km, covering the E and F regions of the ionosphere.

The momentum equation is non-linear and its solutions describe the transport of the momentum in both the horizontal and vertical directions. The momentum equation also includes the horizontal pressure gradients, horizontal and vertical viscosity and ion drag. The non-linear energy equation is solved self-consistently with the momentum equation and it describes the three dimensional transfer of energy between internal, kinetic and potential energy. The solutions also describe the horizontal and vertical heat conduction by both molecular and turbulent diffusion, heating as a result of solar UV and EUV radiation, cooling due to infrared radiation and frictional heating caused by the dissipation of ionospheric currents.

Solving the time-dependent mean mass equation was built into the model by Fuller-Rowell and Rees (1983) which assumes that the upper atmosphere can be represented by atomic oxygen and the sum of molecular oxygen and nitrogen. Further developments of the model have subsequently included the solutions of the species O, O_2 and N_2 with reference to chemistry, transport and the mutual diffusion between these species.

The equation of motion is essentially the Navier-Stokes expressions which can be applied to the system assuming that the thermosphere is collision-dominant and isotropic. The four main forces acting on a unit element of neutral gas are pressure, Coriolis, ion drag and viscosity. The equation of motion and the resulting rate of change of velocity of a unit element or parcel of neutral gas is given by:

$$\frac{\mathrm{D}\boldsymbol{V}}{\mathrm{D}t} = -\frac{1}{\rho}\nabla p - 2\Omega \wedge \boldsymbol{V} - \nu_{ni}(\boldsymbol{V} - \boldsymbol{U}) + \frac{1}{\rho}\nabla(\mu\nabla\boldsymbol{V}) \tag{4.1}$$

where $\boldsymbol{V}$ is the neutral velocity, p is the gas pressure, Ω is the angular rotation rate of the Earth, $\boldsymbol{U}$ is the ion drift velocity, ν_{ni} is the neutral-ion collision frequency, ρ is the gas density and μ is the sum of the molecular and turbulent drift velocities. Equation 4.1 is in the Lagrangian frame of reference, i.e. the element of gas moves with respect to the Earth. To represent the equation in the Eulerian frame of reference, i.e. where latitude and longitude are the independent variables, the following transformation is required:

$$\frac{\mathrm{D}\boldsymbol{X}}{\mathrm{D}t} = \frac{\partial X}{\partial t} + (\boldsymbol{V} \cdot \nabla)\boldsymbol{X} \tag{4.2}$$

where $\boldsymbol{X}$ is any property of the fluid, such as temperature or velocity. Further details of the derivations of the equations in Eulerian form, particularly the equation of energy, are given in Fuller-Rowell et al. (1996).

4.2.2 The Ionospheric Code

The equations of the ionosphere and the thermosphere are solved self-consistently poleward of 23° latitude in both hemispheres. While it could be desirable to express the ionospheric code in the Eulerian frame, ionospheric codes are traditionally in Lagrangian frame allowing elements of plasma to be tracked as they progress along their convection patterns. A compromise of a semi-Lagrangian frame (Fuller-Rowell et al., 1987) enabled a rotating frame of reference for the ionosphere, thus eliminating the need for

a “co-rotating potential” Fuller-Rowell et al. (1996). The equation of ion continuity is given by Equation 4.3:

$$\frac{\partial n_i}{\partial t} = P_i - L_i - \nabla \cdot (n_i v_i) \tag{4.3}$$

which expresses the rate of change of concentration n_i of species i, where P_i and L_i are the ionospheric production and loss rates respectively, and v_i is the bulk ion velocity. Equations for ion diffusion, ion temperature and molecular ions are detailed in Fuller-Rowell et al. (1996).

4.2.3 From CTIM To CTIP

The Coupled Thermosphere Ionosphere Plasmasphere (CTIP) model is based on CTIM so it contains a global thermosphere model and a high-latitude ionosphere model but with the addition of a mid and low-latitude ionosphere/plasmasphere model. This third component of the CTIP model is based on a series of flux tubes separated in magnetic longitude where the tube can move outwards or inwards to a different L-value which determines the equatorial crossing height of the flux-tube above the Earth (McIlwain, 1961). Each flux-tube contains a finite distribution of points with the base-height of each tube at 130km. The model is essentially described in terms of 300 separate tubes, grouped in 20 bunches of 15 tubes, one bunch for each longitude and one tube for each pressure level at that particular longitude. The flux tubes move under the influence of $\boldsymbol{E} \times \boldsymbol{B}$ drift with the velocity of each tube given by

$$\boldsymbol{v} = \frac{\boldsymbol{E} \times \boldsymbol{B}}{||\boldsymbol{B}||^2} \tag{4.4}$$

where $\boldsymbol{E}$ is the electric field and $\boldsymbol{B}$ is the magnetic field. In order to prevent the flux-tubes from moving further and further away from the Earth which would have a negative influence the spatial resolution of the model, over a 24-hour simulation period the flux-tubes return exactly to their starting positions as described in Millward et al. (1996a).

The equations of continuity, momentum and energy balance given in Millward et al. (1996a) are solved along each field-line to give the densities and field-aligned velocities of O^+ and H^+ and the temperatures for both of these ions and the electrons. Of particular importance to this thesis is the calculation of the O^+ densities, as in the F_2 region of the ionosphere the O^+ density is equivalent to the electron density which is measured by ionospheric radio tomography and it is these tomography measurements that have been used to validate the improvements made to the CTIP model.

4.3 Inputs

CTIP model runs are specific to each day so as to account for the changing geometry and activity of the Sun. It is therefore necessary to enter a day of year number and an associated solar flux number, F10.7, obtained from on-line resources such as the UK Solar System Data Centre (`http://www.ukssdc.ac.uk/`). There are several additional options for inputs for the CTIP model, notably a precipitation input and a high-latitude

convection input as outlined below.

4.3.1 Precipitation

Two options are available for auroral precipitation in CTIP: the first uses data taken from the Defense Meteorological Satellite Program (DMSP) and the second uses data from the Television and Infrared Observation Satellites (TIROS). The main difference between these two forms of precipitation input is that the DMSP precipitation is linked to a Kp index which is closely linked to the high-latitude convection input as outlined in Foster et al. (1986). It is the DMSP precipitation option that has been used in this thesis.

4.3.2 High-Latitude Convection

The original high-latitude input in the CTIP model comprises 8 distinct high-latitude convection patterns that can be loaded into each model run as required. Each convection pattern consists of an array of electric potential values spaced at 18° longitude and 2° latitude. These values are read into the model and used to implement the convection routine. The Sheffield version of the CTIP model which is used at Aberystwyth University contains an expansion of the original 8 convection patterns comprising 36 different patterns based on data from the Millstone Hill radar. This gave a wider range of convection patterns from which the single pattern used in each model run could be selected. Combined with the link between convection the Kp-driven DMSP precipitation (Foster et al., 1986) it was possible to simulate a variety of conditions including a range of Kp

values and cross-polar cap potentials.

There are two draw-backs of the convection pattern system in CTIP: first, the library of convection patterns contained only convection patterns representative of the IMF B_z negative condition. Secondly, while the library of patterns had been expanded from 8 to 36 it is still a long way from being representative of the large variations of conditions that occur in the ionosphere and with the high-latitude convection changing minute by minute it is unrealistic to expect just 36 patterns to be representative of all conditions.

The goal of this thesis is to address these two limitations to the high-latitude convection pattern system in CTIP. Subsequent chapters will address how the model has been modified to accept high-latitude input from the Super Dual Auroral Radar Network (SuperDARN) which enables a measured convection pattern to be used as input, including those representative of IMF Bz positive conditions. The SuperDARN convection patterns are available on the internet (`http://superdarn.jhuapl.edu/`) at 10-minute intervals this also allows the use of a convection pattern pertinent to the day and time of interest for a particular model simulation.

4.4 Alternative Models

The CTIM-CTIP type models are just two of the available ionospheric models. This section discusses some of the alternatives. Within the ionosphere-thermosphere system three different types of models can be identified each with their own characteristics:

1. semi-empirical and empirical models

2. physical models

3. ionospheric profilers: models based on routinely scaled ionospheric data

One of the best known empirical models that is widely used for a range of different applications is the International Reference Ionosphere (IRI) (Bilitza, 1990) which, for a given location, time and date, describes the electron concentration, electron temperature, ion temperature and ion composition in the altitude range from about $50-2000$km. It also measures the Total Electron Content (TEC), which is the line integral of the electron density between the satellite and the receiver. IRI uses data from a wide range of ground-based ionosondes in addition to incoherent scatter radars such as Jicamarca and Millstone Hill as well as data from in situ instruments.

D. N. Anderson and colleagues of the Phillips Laboratory of the USA have developed a range of semi-empirical models whereby a combination of databases of coefficients that reproduce theoretically calculated profiles based on existing physical data are used. Examples of such models include the Semi-Empirical Low-Latitude Model (SLIM) (Anderson et al., 1987) which determines the electron concentration profiles for different latitudes by solving the continuity equation for O^+ ions and the Parameterised Real-time Ionospheric Specification Model (PRISM) (Daniell et al., 1995) which consists of both a Parameterised Ionospheric Model (PIM) and near-real time-data obtained from ground and satellite sensors.

Probably the best know semi-empirical thermospheric model is the Mass Spectrometer and Incoherent Scatter (MSIS) model which was developed by the Goddard Space Flight Centre (GSFC). It is based on satellite mass spectrometer data and ground inco-

herent scatter data. GSFC have also developed an empirical thermospheric Horizontal Wind Model (HWM) and these two thermospheric models are often used as inputs for physical modelling (Lathuillre et al., 2002).

Physical models depend on describing the general behaviour of ionospheric ions using a set of transport equations for continuity, momentum, energy and heat flow which are derived from Schunk (1977). However there is also the need to model particles such as precipitating electrons that move along the magnetic field lines, producing heat and ionisation. These particles are modelled by a kinetic approach, using data sets as input for parameters such as auroral precipitation or high-latitude convection. the result is a need for a fully-coupled model using both the physical and empirical approaches to completely describe the ionosphere. In addition to the CTIP model, other models that follow this approach include the Utah State university Model of the global ionosphere Schunk and Sojka (1996), FLIP, the University of Alabama Field Line Integrated Plasma model (Richard and Torr, 1996), GTIM, the Phillips Laboratory Global Theoretical Ionospheric Model (Anderson et al., 1996) and the TRANSCAR model (Lilensten and P.L. Blelly, 2002). All of these models are suitable for being used to investigate the influence of different physical processes on the ionosphere. Typical outputs from these types of model include electron concentration distribution, electron and ion temperatures and ion velocity.

The final type of ionospheric model under discussion in this section is known as "ionospheric profiler". These models use data assimilation techniques to estimate the variation of electron concentration distribution with height. One of the early profilers

by Bradley and Dudeney (1973) describes the electron concentration profile up to the peak of the F2-region. A more recent model by Di Giovanni and Radicella (1990) is able to describe the electron profile in the E, F1 and F2-regions of the ionosphere.

4.5 Previous CTIP Results Relevant to this Thesis

A number of prior results are outline in this section: The importance of convection on the winter high-latitude ionosphere density structure was highlighted by Fuller-Rowell et al. (1987, 1998, 1991b) and Millward et al. (1993). Fuller-Rowell et al. (1987, 1998) showed that the plasma convection was dominant in the formation of the dayside trough in winter whilst during the summer months, plasma up-welling is cited as the dominant formation mechanism. Enhanced electric fields can also lead to the depletion of the electron density causing the formation of the trough as described by Millward et al. (1993). Fuller-Rowell et al. (1991b) also illustrated the importance of the tongue-of-ionisation and precipitation in producing the poleward wall of the trough.

Millward et al. (1993) modelled the effects of introducing localised enhancements in the high-latitude dawn convection electric field similar to electric field spikes described and analysed by Winser et al. (1990). The effect of the enhanced electric field was to increase the eastward velocities which heat the neutrals and ions via frictional heating. These increased temperatures affects recombination rates to reduce the electron density which causes a trough in the ion density.

Schoendorf et al. (1996) studied the effectiveness of the statistical magnetospheric inputs in predicting the high-latitude ionosphere with CTIM. Observations from 9 days

of EISCAT data under solar maximum and 4 different Kp conditions were averaged hourly and compared to two latitudes: 68°GLAT and 72°GLAT at altitudes of 140km and 300km. High latitude inputs of convection and auroral precipitation were altered to determine how they effect the high-latitude ionosphere. It was found that the auroral precipitation input was too wide latitudinally when it was compared to the EISCAT data. Care needs to be taken in attempting to improve the model and it is vital that the model is in no way "tweaked" to suit the observations. However the model is able to predict the general behaviour of the high latitude ionosphere when compared to EISCAT data for a specific three-day period.

Pryse et al. (2005) used the CTIP model to investigate the electron density in the high-latitude ionosphere over a continuous range of latitude and compared these results to those obtained by ionospheric radio tomography over a similar latitudinal range. The time of interest for this work was a 6-hour period in the post-noon sector. The results of this study revealed that the model tends to over-predict the electron densities at high latitudes and that the complex interplay between the different ionospheric processes is not yet fully understood.

4.6 Conclusion

This Chapter has sought to outline the basic workings of the CTIP model. Some of the key model results that are relevant to this thesis have been discussed. Finally, the CTIP model has been placed in context with other types of ionospheric model.

Chapter 5

Modifications to the CTIP Model

5.1 Introduction

As has been outlined in Chapter 4, one of the weaknesses of the original CTIP model is the lack of scope for a range of high-latitude convection patterns. It is also well-established that the polarity of the IMF B_z component influences the form of the high-latitude plasma convection pattern. This in turn affects the distribution of ionospheric plasma at polar and auroral latitudes, drawing dayside plasma anti-sunwards across the polar cap in a tongue-of-ionisation. Therefore, the ability to model the ionised density distributions under a wide range of different electric potential patterns is particularly useful in the study of how the high-latitude convection influences the distribution of plasma in the polar regions.

Before the modified method of inputting electric potential patterns into the CTIP model can be used to assist with the interpretation of data from sources such as the

Aberystwyth University Radio Tomography Experiment it is important in the first instance, to check that the technique works and second, use the modelling results to confirm that the new method agrees with mature interpretations of existing data studies. Once these two things have been established it is possible then to go on to use the modified electric potential inputs to assist with the interpretation of new data. This Chapter covers the first of these issues and subsequent chapters will extend the validation process to include comparing the new electric potential pattern method with a study by Middleton et al. (2008) and finally the technique will be used to interpret data from the Alaskan tomography chain.

5.2 Structure of the CTIP Convection Pattern

If an electric field $\boldsymbol{E}$ is applied perpendicular to the magnetic field $\boldsymbol{B}$ then the plasma particles drift at velocity $\boldsymbol{v}$ given by Equation 5.1

$$\boldsymbol{v} = \frac{\boldsymbol{E} \times \boldsymbol{B}}{||\boldsymbol{B}||^2} \tag{5.1}$$

which is normal to both $\boldsymbol{E}$ and $\boldsymbol{B}$. The electric field is obtained from the gradient of the electric potential and the high-latitude convection pattern in the CTIP model consists of an array of such electric potential values. Before any changes can be made to the CTIP convection pattern, it is important to have a good understanding of how the electric potential values are used by the model. The high-latitude convection pattern in CTIP is identified with an array of values that defines the electric potential in kV over a range of

latitudes and longitudes. As the CTIP model has a grid pixel dimension of 2° in latitude and 18° in longitude, there is an electric potential value for each of these grid-points as shown in Figure 5.1.

The convection pattern is made up of 20 groups of electric potential values, one group for each of the 18° longitude or 1.2 hours in MLT. Within each longitude group there are 23 different electric potentials, one for each latitude extending from 89° to 45°MLAT in 2° intervals, so one electric potential pattern consists of 460 distinct values, with, in the case of the IMF B_z negative condition as found in the original library of convection patterns, the negative electric potentials on the duskward side and the positive electric potentials on the dawnward side. Clearly, it is important that this structure is kept when different patterns are used in the CTIP model. By looking at the model code and plotting various electric potential patterns it was possible to determine exactly which positions in the array of numbers correspond to the 460 different grid-points and by using different electric potential values for each of the grid-points it is possible to custom-design a convection pattern. While the adaptations to the convection pattern in the CTIP model are interesting in their own right, the whole purpose of this work is to then go on to use the CTIP model with its new range of convection patterns to interpret some of the ionosphere's large-scale features detected by radio tomography instrumentation. It was decided to make use of the SuperDARN electric potential patterns which have the advantage of being real convection patterns based on real data so they can be used to represent the high-latitude convection at any given time, in particular at the time of interest of the ionospheric radio tomography passes that were used in this thesis.

5.3 SuperDARN Electric Potential Patterns

SuperDARN electric potential patterns at 10-minute intervals are available on the internet (`http://superdarn.jhuapl.edu/`) both as images and as raw data. While it is possible for a greater level of accuracy and more frequent images to be obtained by contacting the Principal Investigator in the UK, the idea behind using the images and data directly from the internet is to enable the convection patterns to be readily available to use as input to CTIP. Typically it is possible to browse through the images on any given day and select one that is suitable for the study being undertaken, taking care to use a pattern with many data points as the larger the number of data points the more the electric potential lines are shaped by real data. Initially this was done by selecting a pattern that was IMF B_z negative similar to a pattern from the original library of Millstone Hill convection inputs so that the technique of inputting the data into the model could be verified. By examining the downloaded electric potential file from the SuperDARN website, it was clear that the resolution of the SuperDARN data was much higher than the 460 electric potential values required for a CTIP convection input file. Given that the intention was to use CTIP for the large-scale modelling of features in the order of tens to hundreds of kilometers (for example, to look at the tongue-of-ionisation), it was not deemed necessary or time-efficient to recode the entire CTIP model to take into account of the enhanced SuperDARN data resolution. Instead, a short IDL routine was written to take the SuperDARN data file, extract the required 460 electric potential values and output a file that could be loaded directly into CTIP. This code searches the electric potential file for the electric potential value that corresponds to each MLT and

magnetic latitude point required to represent the convection pattern.

5.4 Using SuperDARN Input in CTIP

To check that the new method of inputting high-latitude electric potential patterns works, two days in December 2002 were chosen where the IMF B_z component was in the first case, stable and negative and in the second case, stable and positive. This means that it was possible to choose a representative convection pattern for each of the two IMF cases. Figure 5.2 shows that the IMF was stable and, on average, negative during the period between 25 December 2002 and about 16UT on 26 December 2002.

Figure 5.3 shows that the IMF B_z component remained positive throughout 17-19 December 2002.

5.4.1 Modelling Parameters

CTIP model simulations were run for 21 December (day 355) which is a day chosen to be representative of the two days from which the convection patterns were taken and also representative of winter solstice. The geomagnetic index was $Kp = 2$ and the solar index $F10.7 = 150$, the average solar condition for December 2002. The model was run without particle precipitation. Representative high-latitude convection input for IMF B_z negative as obtained from the SuperDARN website is shown in Figure 5.4. Figure 5.5 shows a similar plot for the condition of IMF B_z positive.

Both of these electric potential patterns were chosen because they represent the typical convection cell for the day of interest as shown on the SuperDARN website.

5.4.2 CTIP Model Output

To illustrate the difference between the tongue-of-ionisation under IMF B_z negative and IMF B_z positive, selected plots are shown in Figure 5.6 and Figure 5.7. These two figures clearly show the difference that the convection pattern has on the tongue-of-ionisation. Figure 5.6 shows the tongue of ionisation growing to a peak at 18UT under IMF B_z negative conditions as plasma is drawn anti-sunward across the polar cap. In the 18UT plot, the tongue-of-ionisation is drawn towards the duskward side, following the shape of the convection pattern used for this model run (see Figure 5.4).

In contrast, the IMF B_z positive electric potential patterns prevent the tongue-of-ionisation from being drawn across the polar cap. This is clearly shown by comparing the red ($4.0 \times 10^{11} m^{-3}$ contour) from the 18UT plot in Figures 5.6 and 5.7. This is because the positive convection pattern is of a very different nature to the negative pattern. Instead of the classic two-cell convection pattern as seen in the IMF B_z negative plot (Figure 5.6), there are lobe cells present as shown in Figure 5.7. This alters the convection pattern especially with regard to the anti-sunward flow, which in the case of positive convection patterns occurs at lower latitudes than with the IMF B_z negative case, as the anti-sunward flow is located more at the periphery of the polar cap.

5.5 Variable Convection

One major flaw in the CTIP model is that the convection pattern chosen needs to be representative of the entire day that is being modelled. In reality, high-latitude convection is changing on a moment-by-moment basis. The use of varying the convection

pattern with time goes a small way towards addressing the need for continuously changing electric potential patterns. Within the coding of the CTIP model there is scope to introduce up to 7 different high-latitude convection patterns, enabling the pattern to be changed at 12-minute intervals throughout the day being modelled. Once the validity of the technique of using SuperDARN convection patterns and the high-latitude input had been established, it was possible to include any of the patterns found on the SuperDARN website and introduce these different patterns into the CTIP model every 12 minutes. Clearly this is an improvement on just having one electric potential pattern held at steady-state for the modelling day, but it is far from the continuously changing convection patterns that occur in the high-latitude ionosphere. Ideally it would be possible to take all the SuperDARN electric potential data for a given day and read it into the CTIP model continuously so that the convection pattern routine resembles as closely as possible what is physically happening in the ionosphere at that time. However there are issues here with model stability: CTIP has been coded to enable changes in convection every 12 minutes so varying the convection pattern more frequently than this would first require substantial re-coding of the model and secondly potentially create problems in the convergence of some of the equations that are solved. The model is further limited to 7 different convection patterns and again, expanding this number would call for a substantial re-write of the code.

Now that work has been done to validate the use of SuperDARN convection patterns in CTIP, one way in which the scope for variable convection has been used is to investigate the results of using two very different high-latitude convection patterns: one

IMF B_z negative and one IMF B_z positive. By showing that it is possible to successfully change the convection pattern in CTIP it would then be possible to use ionospheric radio tomography data taken from a time where the IMF changes from a stable IMF B_z negative pattern to a stable IMF B_z positive pattern to validate the use of this technique.

5.5.1 Results

The two SuperDARN IMF B_z negative and positive convection patterns that were used in Section 5.4.1 were put into the CTIP model so that the model would read each convection pattern in turn. The electric potential patterns are called in CTIP every 12 minutes so it would be possible to change the convection pattern much more quickly. However as this work is aimed at eventually using CTIP to assist with the interpretation of tomography data taken from a period of time where the IMF has switched from one stable IMF B_z orientation to another, for a first attempt at variable convection it was decided to change the convection only once, half-way through the day for which the model is run. The CTIP modelling day commences at 13UT, therefore in each case the first convection pattern is introduced at this time and the second convection pattern 12 hours later at 1UT, so by examining UTs $8-15$ it is possible to observe the change in convection produced by the model.

Figure 5.8 shows the response of the modelled electron density as a result of the convection changing from IMF B_z negative to positive with time. The dial plots from 8UT to 12UT show the negative convection pattern causing the tongue-of-ionisation to build up as plasma is swept anti-sunwards across the polar cap. Once the positive

convection pattern is introduced at 13UT, instead of the tongue-of-ionisation continuing to increase and to a peak at 18UT as in Figure 5.6, the new convection pattern begins to draw plasma anti-sunward at lower latitudes while the plasma from the tongue-of-ionisation decays.

Figure 5.9 shows the convection changing in the other direction, from IMF B_z positive to negative with time. The dial plots from 8UT to 12UT show the positive convection pattern causing very little in the way of plasma being moved across the polar cap. After the negative convection pattern has been introduced at 13UT, very quickly the tongue-of-ionisation begins to establish itself as the convection drags the plasma across the polar cap.

Both of these modelling examples show that it is possible to use the SuperDARN electric potential patterns to represent time-varying convection, though much more work needs to be done on this aspect of the CTIP model before it can be reliably used to interpret data.

5.6 Conclusion

This chapter has outlined the methodology of using SuperDARN electric potential patterns as the convection input in the CTIP model. The model results presented here show that it is technically possible to use SuperDARN data to greatly enhance the scope of the high-latitude convection routine in CTIP by using real convection patterns rather than those determined by statistical data. At this stage, no attempt has been made to verify the technique against data - this is done in subsequent chapters with the use of

ionospheric radio tomography.

Chapter 6

CTIP Modelling with SuperDARN Electric Potential Input: Verification by Radio Tomography

6.1 Introduction

In Chapter 5, the method for using SuperDARN electric ptential input for the CTIP model was outlined. This work is now verified by the use of radio tomogrpahy data from the European sector. As in the polar and auroral latitudes the ionised atmosphere is a highly structured plasma, the technique of radio tomography (see Section 3.3) is particularly useful for studying the larger electron density structures of the ionosphere. Such features are on scales of tens to hundreds of kilometres, which are reviewed by Crowley (1996). A prominent example is the tongue-of-ionisation (TOI), where pho-

toionisation from sub-auroral latitudes on the dayside is drawn anti-sunward by the high-latitude plasma convection pattern towards the polar cap (Valladares et al., 1994). At high F-region altitudes the lifetime of the plasma is long enough for the ionisation to be drawn through the polar region and into the nightside sector. A modelling study by Bowline et al. (1996) indicated that the TOI is expected to be prominent at Ny-Ålesund in the European sector in the evening. During its transit through the polar cap the TOI may be modulated into polar patches and various processes have been proposed for this (for example Anderson et al. (1988), Sojka et al. (1993), Rodger et al. (1994) and Milan et al. (2002)). Observations of the remnants of the TOI and polar patches on the nightside are reported by Middleton et al. (2008) and Pryse et al. (2006b).

Large-scale high-latitude ionisation enhancements have been observed by several experimental techniques including ionospheric sounders, radiotomography and incoherent scatter radar. However, there are very few direct comparisons of the ionospheric observations with modelled distributions. Middleton et al. (2008) presented multi-instrument observations of a cold high-altitude plasma enhancement on the nightside, interpreted as plasma produced on the dayside and transported across the polar cap in the convective flow and into the auroral region. The interpretation was supported by model runs of the CTIP model, although there were disparities in the location and density levels of the observations and model output. Schoendorf et al. (1996) compared electron densities measured in the auroral region by the European incoherent scatter radar (EISCAT) with CTIP model output. This study also showed the potential of the model to reproduce the observed densities, but also highlighted the important role of

the high-latitude input parameters to the model to obtain agreement at all geographic locations and UTs. One way to begin to address the disparities between the location and density levels of the observations and the model output is to use the modified CTIP model with SuperDARN high-latitude electric potential patterns used as input. The aim of this study is to use radio tomography images in order to validate the use of SuperDARN electric potential data in the CTIP model.

6.2 Method

Two particular case studies are considered in this work with contrasting IMF conditions. The first is under IMF B_z negative with the SuperDARN radar showing a classic two-cell convection pattern characteristic of the condition. The other is a case under IMF B_z positive with the convection pattern likely to include polar lobe cells. The modelled output is compared with radio tomography observations made by the International Ionospheric Tomography Community (IITC), which give the latitudinal variation of the electron density on a spatial scale appropriate for comparison with the model output. The two case studies with different IMF orientations were chosen to coincide with well-studied radiotomography investigations. Tomographic reconstructions from three chains of the International Ionospheric Tomography Community (IITC) were used: two operated by Aberystwyth University, in the Scandinavian sector and the UK, and the third in Greenland operated by the Applied Research Laboratories, University of Texas. The locations of the receivers in the three chains are shown in Figure 6.1. The tomography results have already formed the focus of two previous works into the different

physical processes at high latitudes (Middleton et al., 2005, 2008) where the observed features were interpreted by multi-instrument investigations. By choosing these studies with with mature interpretations, ambiguity in the comparisons of observations with the model output was less likely.

For the model runs presented in this Chapter, the day number and solar flux F10.7 index were set in accord with the time of observations. The auroral precipitation input was switched off, so as to focus on effects of the transport of plasma at polar and auroral latitudes. Of particular interest was the electric potential pattern input, where the library input was substituted by an electric potential pattern from the SuperDARN radar network. This pattern was selected to be appropriate for the time of the tomography observations and obtained from the SuperDARN website `http://superdarn.jhuapl.edu/`.

6.3 Results

6.3.1 IMF B_z negative: 12-13 December 2001

6.3.1.1 Experimental observations

The period of interest spanned an interval from about 23UT on 12 December 2001 to 03UT on 13 December 2001. The IMF governing the high-latitude plasma flow had been negative at about -5nT for more than 10 hours prior to the time interval and remained negative throughout the period of observations. By looking at the online SuperDARN electric potentials patterns at 10-minute intervals showed the characteristic two-cell pattern which is consistent with antisunward plasma flow over the polar cap

from the day to nightside and return sunward flows at lower latitudes on the dawn and dusk flanks. The electric potentials showed the inevitable small variations in the detail of the cells from frame-to-frame, but on the large scale their general form remained essentially unchanged throughout the time interval with the dawn cell being slightly smaller than the dusk cell. This is an important consideration to the modelling of the experimental observations with CTIP as one electric potential pattern is required to represent the day of interest so large variations of the convection patterns over the time of interest would lead to less representative model output.

Tomographic reconstructions from five satellite passes during the interval, three monitored by the Scandinavian chain and two by the chain in the UK, showed a clear, persistent density enhancement that formed the poleward wall of the main ionisation trough in the post-magnetic midnight local time sector. Figure 6.2 shows three of the reconstructions as examples, two obtained from the Scandinavian chain and the other from the UK chain. The locations of the maximum density of the enhancement in all five reconstructions are also shown mapped onto a magnetic latitude (MLAT) versus magnetic local time (MLT) polar plot. Comparisons of the tomographic observations with measurements by the EISCAT UHF radar on mainland Tromsø showed that the enhanced densities were cold and at high altitudes. This supports the interpretation of the features being cross-sections through ionisation that had originated at an earlier time and different location, possibly on the dayside, and had been carried by the plasma flow in a tongue-of-ionisation into the region of observations. Further details of the observational results and their interpretation are given by Middleton et al. (2008).

6.3.1.2 CTIP model output

The model was run for 13 December and an F10.7 index of 230. The SuperDARN electric potentials for 0240UT were taken to be representative of the interval, and showed clearly the two-cell pattern with the dawn cell being slightly smaller than the dusk cell (Figure 6.3). The ion density output from the model at an altitude of 320km, near the peak of the modelled nighttime F-region peak, is shown at 3-hourly intervals of UT in the polar plots of Figure 6.4. Magnetic noon is at the top of each panel, with 18MLT on the left-hand-side and 06MLT on the right-hand-side. Magnetic latitude extends from 50°MLAT on the outer circumference to the magnetic pole at the centre. The small white region near the pole encompasses the geographic pole, a region where the model is unable to produce reliable output due to the convergence of the lines of longitude. A prominent plasma feature in most of the panels is the tongue-of-ionisation (TOI) comprising photoionisation drawn from the dayside into the nightside post-midnight sector by the convective flow. A UT dependency is clear in the TOI, with the feature being most prominent in the 18UT panel but with only remnants visible at 06UT. This variation is attributed to the offset of the geomagnetic and geographic reference systems, with a larger proportion of the magnetically controlled convective flow being in sunlight when the geomagnetic pole is closer to the Sun than the geographic pole, for example near 18UT. The white line shows the position of the 18°E meridian, near the location of the Scandinavian receiver chain. The interception of the tongue by this line in the bottom panels suggests that the European sector is is the right place to observe the effects of the tongue on the nightside.

Figure 6.5 shows the ion density output in the same format as Figure 6.4 but at hourly intervals spanning the time of interest for the study. The panels for 22UT and 23UT are strictly for 13 December rather than 12 December when the observations were made, however this is not of significance as there is very little variation in the model output from day-to-day near the winter solstice when all other conditions are kept identical. A TOI is prominent in the panels for the earlier times, being drawn over the polar region into the nightside and then towards the dawn sector at auroral latitudes. The 300km intersections of the satellite trajectories for each of the five tomography reconstructions are shown on the respective panels. Those for the two reconstructions at 0150UT (UK chain) and 0156UT (Scandinavian chain) are for the same satellite pass, but are shown on different model panels for clarity.

6.3.1.3 Comparison between model output and radio tomography observations

Comparisons of the modelled output and the tomography reconstructions are shown in Figure 6.6. The first column shows the latitude-versus-altitude modelled distributions given at 18°E for hourly intervals from 22UT to 03UT, where the main feature in each of the panels is the intersection through the TOI drawn into the dusk side. The colour scale used for the latitude-versus-altitude plots are slightly different to those of the polar plots to allow direct comparison with the tomography reconstructions. The density of the TOI intersection decreases with UT as a consequence of ionisation recombination in winter darkness, and its latitude decreases as it is drawn further towards dawn by the convective flow. The second column shows the corresponding tomography images. As there is a difference latitudinal coverage of the UK and Scandinavian reconstruc-

tions, the images have been offset accordingly to ensure consistency in the latitudinal location of the enhancement in the column. The large density enhancement forming the poleward wall of the main ionisation trough is a prominent feature of each reconstruction. The smaller-scale density features seen poleward of the large enhancement and generally at lower altitude in the images from Scandinavia are likely to be in the auroral region, and caused by soft particle precipitation. However, these are outside the scope of the current study and will not be considered further. The discontinuity in the equatorward field of view of the reconstruction at 0156UT occurs because of the satellite signal being lost at this location, and the image to the left of the discontinuity reverts to the initial background ionosphere for the inversion process. In general, the observed densities in the large enhancement are in good agreement with those modelled. A general trend of decreasing densities with increasing UT is also revealed in the observations, although there are some slight deviations in the trend, in particular an increase in the reconstruction at 0007UT. Possible reasons for this deviation are small temporal variations in the convection or particle precipitation upstream at an earlier time, which would not be taken into account in the CTIP model. There is also reasonable agreement in the location of the modelled and observed enhancement. For example in the model panel for 00UT and tomography reconstruction at 0007UT, the maximum density is near 70°N and 69°N for the observations and model respectively. The observed equatorward and poleward edges as defined by the $5 \times 10^{11} m^{-3}$ contour are at 64°N and 74°N respectively, while the corresponding equatorward edge in the model is also at 64°N, but the northern most edge extends to almost 80°N. Similarly, the extremes for

the enhancement in the bottom row are 62° and 65°N for the reconstruction at 0243UT and 63° and 67°N for the model at 03UT. In both examples the modelled enhancement extends over a larger latitude range than that observed, with a tendency for the modelled latitudinal gradients of the walls to be less steep than observed. The difference in the gradient is a likely consequence of the different latitudinal spatial resolutions of the model and observations, with the latitudinal dimension of the pixels being 0.25° in the tomography reconstruction but 2° in the model. There are also differences in the vertical profiles of the observations and model, however, since there is some ambiguity in the vertical distribution of tomographic images, arising due to a limited observing geometry (Pryse, 2003), it is not possible to draw definitive conclusions here.

Energy deposition by particle precipitation has been excluded from the main study, with the auroral input in general being switched off in the model runs. However, output from a run corresponding to that in Figure 6.4, but with the precipitation switched on and with a Kp index of 2 appropriate for 00-03UT on 13 December, is shown in Figure 6.7. The first panel for 06UT, when the TOI is absent, shows the effect of the precipitation with a partial ring of enhanced ionisation representing the auroral oval. This reaches a latitude of about 80°MLT near noontime but extends to lower latitudes on the nightside. Comparison with the corresponding panel in Figure 6.4 reveals that the density level in the auroral postmagnetic midnight sector is increased from about $2 - 4 \times 10^{11} m^{-3}$ to about $5 - 7 \times 10^{11} m^{-3}$ when precipitation is included. Increased density levels also occur in regions removed from the immediate region of the auroral precipitation, with values in the region of smallest nightside density increasing from

$2-3\times10^{11}m^{-3}$ to $3-4\times10^{11}m^{-3}$. Care is needed in the interpretation of the colour scales in the comparisons, as the highest red level has been increased from greater than $8\times10^{11}m^{-3}$ to greater than $9\times10^{11}m^{-3}$ in the precipitation model output in order to clearly show the features of interest. The TOI remains a dominant feature of the panels of 12UT to 00UT (Figure 6.7), maximising at 18UT to 21UT. The densities in the tongue are enhanced by the precipitation, for example the maximum density at 00UT in the absence of precipitation was some $6-7\times10^{11}m^{-3}$, whilst with precipitation it is in excess of $8\times10^{11}m^{-3}$ and more in line with those in the enhancement observed at 0007UT. Fuller treatment of the precipitation is outside the scope of this investigation. However, it has a marked effect that needs consideration in future as indicated by Schoendorf et al. (1996) and Pryse et al. (2005).

6.3.2 IMF B_z positive: 26 November 2001

6.3.2.1 Experimental observations

The IMF B_z very stable between about 11UT and 16UT on 26 November 2001, being positive with values essentially between 0nT and 1nT. During the interval six satellite passes were monitored by the Scandinavian chain and six by the chain in Greenland displaced by some 70° longitude to the west. Collectively, the reconstructions showed a stable ionosphere with spatial rather than temporal variation. The images consistently showed evidence of a localised density enhancement poleward and distinct from the main photoionisation. Figure 6.8 shows the trajectories of all twelve passes, which were mostly in the 12-18MLT time sector. A dot on each trajectory, with the exception

of the two trajectories nearest to 12MLT, indicates the location of the maximum electron density of the localised enhancement observed during the pass. Three sample tomography reconstructions are also shown, showing the enhancement apparently becoming increasingly detached from the photoionisation with increasing MLT. The full set of reconstructions was presented and interpreted by Middleton et al. (2005) with the enhanced densities being identified as cross-sections through a TOI (shown schematically by the purple curve in Figure 6.9) drawn antisunward around the periphery of a polar cap closed to plasma inflow under the condition of northward IMF. The interpretation was supported by satellite horizontal cross-track plasma drift measurements.

6.3.2.2 CTIP model output

The CTIP model was run for 26 November 2001 with an F10.7 value of 175, appropriate for the day but significantly lower than in the previous study. There were only limited plasma drift measurements by the SuperDARN radar for this particular interval, which lacked the large scale coverage required to shape the electric potential patterns. As a result of this, the SuperDARN electric potentials from another time were used. The example chosen was for 0130UT on 18 December 2002 (Figure 6.10), where the flow measurements were abundant and showed a sunward flow on lobe cells in the polar cap. This pattern was chosen because its general form was broadly similar to that inferred from DMSP cross-track observation shown in Middleton et al. (2005), comprising sunward flow on the dayside near 12MLT, and antisunward flow at lower latitudes on both the dawn and dusk sides. However, given the general variations between plasma convection patterns there were inevitably differences in the details. The IMF B_z influencing

the chosen SuperDARN pattern was also positive and stable, but with values between about 8nT and 9nT, significantly larger than those corresponding to the tomographic images. At this stage no attempt was made to compare the chosen electric potential pattern directly with the tomographic observations.

The modelled ion density at 3-hourly UT intervals is shown in Figure 6.11. The panels take the same format as those in Figure 6.4, but are for an altitude of 270km which was more appropriate for the height of the nighttime F-region peak in this instance. The white line shows the 18°E meridian near the Scandinavian chain and the black line the 54°W meridian near the chain in Greenland. The modelled densities are substantially less than those for the B_z negative case, which can be attributed to the lower F10.7 index value. The variation of dayside photoionisation with UT is again clearly seen, but in this case there is no TOI over the central polar cap. Careful inspection reveals two less intense TOIs drawn antisunward between about 70°MLAT and 80°MLAT in the panels centred on a universal time of 18UT, one on the afternoon side and the other on the dawn side. A hint of the features can be seen in the panel for 12UT and remnants at 00UT, but it is absent in the panels for 03UT, 06UT and 09UT.

Corresponding model outputs at hourly intervals between 11UT and 18UT are shown in Figure 6.12, encompassing the time of interest. The sequence shows the growth phase of the TOIs, with the white line at the 18°E meridian intersecting the afternoon tongue. At the later UTs the line has almost "overtaken" the TOI and intersects the lower densities at its nose. The 54°W meridian shown by the black line lags the 18°E through the early stages of the development of the afternoon tongue. The satellite trajectories, indi-

cated in MLT in Figure 6.7, were broadly in the vicinities of the two meridians shown in Figure 6.10.

6.3.2.3 Comparison between model output and radiotomography observations

Latitude-versus-altitude intersections through the model output at 18°E (Figure 6.13) clearly show the TOI starting to separate from the main photoionisation at 13UT and becoming increasingly distinct with increasing UT. A high-latitude afternoon trough develops in-between the two enhancements, and by 16UT the two regions of larger densities are completely separated on the contouring scale used.

It is not appropriate to make a one-to-one comparison between the details of the model and tomography images in this case as was done in the previous case study, owing to the convection pattern not corresponding directly to the time of observations. However, the similarities of the observed and model plasma distributions are clearly seen, with both the panels of Figure 6.11 and the three tomography reconstructions in Figure 6.8 showing a TOI near 70°−80°MLAT separating from the main photoionisation as UT and MLT increase. Decreasing density levels with increasing time also occur in both model and observations, attributed to ionisation recombination in the absence of sunlight. Despite differences in the finer details, such as in the absolute density levels, the comparison shows the capability of CTIP model to reproduce the spatial structure of the polar cap ionisation distribution under steady IMF conditions even under IMF B_z positive.

6.4 Discussion

The large-scale spatial structure of the polar and auroral ionosphere is governed strongly at high latitudes by the electric potentials. The underlying physics is relatively well understood, however the variability that the electric potentials demonstrate because of solar wind and magnetospheric influences remains to be addressed. It is not possible at present to predict the detail of the size and strength of the electric potential pattern at any given time. The CTIP model uses the electric potentials as an input driver. A limitation of the model is the restricted set of electric potential patterns available to describe the horizontal transport of plasma within the polar and auroral regions. Those available are provided from a library of potential patterns derived from observations by the Millstone Hill incoherent scatter radar at mid-latitudes (Foster et al., 1986). The set comprises patterns of various sizes and strength, but of a form usually associated with IMF B_z negative. It does not contain patterns to describe sunward lobe-cell flow within the polar cap as is often the case under IMF B_z positive. An unsuitable electric potential input for a given situation leads to significant limitations in the ability of the CTIP model to predict the plasma distribution. The current study aims to address this shortcoming by using electric potentials obtained from the SuperDARN radar that are readily available from the SuperDARN website. Whilst it is appreciated that second level SuperDARN data is available on request, this was not deemed necessary for the proof-of-concept study where the IMF conditions and electric potentials were stable over an extended period of time. Use of the on-line potentials was also regarded in-keeping with “near-real-time” modelling and prediction of the ionosphere.

Two examples were considered, the first under stable IMF B_z negative and the latter under stable B_z positive. The examples were chosen to coincide with radiotomography reconstructions that had mature interpretations from multi-instrument studies. Radiotomography imaging, with a latitudinal pixel dimension of 0.25° for the reconstruction grid, was particularly well suited for verification of the CTIP model which has a latitudinal step dimension of 2° latitude. The stable conditions were essential for the model in its current form, where only steady convection is supported. The chosen potential patterns were therefore regarded as representative of the entire intervals of interest.

The electric potential pattern used in the model for B_z negative was obtained from measurements made during the interval of interest, and was representative of the patterns observed throughout the interval. In this case the effects of the TOI were clearly observed in the model output in the post-magnetic midnight sector. The densities of the modelled feature were only slightly smaller than those observed, with the exception of the pass at 0007UT, with the differences being generally about $1 \times 10^{11} m^{-3}$ or less. Both observations and model showed the trend of decreasing density with UT, attributed to ionisation recombination in winter darkness. The latitudinal location and extent of the feature also compared well, although the model failed to reproduce the observed gradients on the walls of the enhancement, a likely consequence of the resolution of the model being lower than that of the tomography. The model output in the study showed significant improvement over that obtained by Middleton et al. (2008) using the Millstone Hill library potential patterns, with the modelled density enhancement generally matching that observed both in latitude and absolute density.

There were no SuperDARN measurements at the time of the B_z positive case, and an electric potential pattern from a different time period was used. IMF B_z was also positive and stable during this interval, albeit larger in magnitude. The flow pattern was representative of that anticipated for the IMF conditions and in-keeping with the form of the DMSP horizontal drift measurements in Middleton et al. (2005). The model output yielded an ionospheric distribution broadly similar to that observed, with a tongue-of-ionisation being drawn around the periphery of the polar cap. However, there were differences in the latitude of the modelled and observed tongue with the modelled location being slightly equatorward of that observed and the model densities being smaller, discrepancies that could have arisen because of the convection pattern not being that for the exact interval of interest. Nevertheless, it is important to note that the model in this instance was able to reproduce a TOI being drawn around the periphery of the polar cap in keeping with the processes inferred from the observations. This was not possible with the previous standard electric potential input to the model.

The results of the study pave the way for comparisons of the modelled ionosphere with radiotomography reconstructions and observations by other experimental techniques under a range of different geophysical conditions, in particular IMF orientation and magnitude, season, and solar cycle. The dependency of the spatial distribution of ionisation on the longitude of observation, attributed to the offset of the geographic and geomagnetic reference systems, also requires further consideration, and future comparisons between the model and radiotomography observations in different longitude sectors have the potential to establish the complementary distributions of different re-

gions of the globe. The morphology of plasma distribution in different sectors is not only of interest to the understanding of the physics of the density structuring, but is also of relevance to radio applications where latitudinal gradients on the walls of plasma enhancements and troughs are of concern to practical radio systems.

6.5 Conclusions

The presented investigation has focussed on the modelling of the ionospheric plasma distribution in the polar and auroral regions using the CTIP model. The new aspect has been the use of electric potentials obtained from the SuperDARN network as input. Two cases were considered, both under stable conditions of IMF B_z negative and positive respectively, where there were radiotomography reconstructions available for comparisons. Both sets of tomography reconstructions had been the focus of previous multi-instrument studies and had mature interpretations. The modelled plasma distributions were compared with those observed by radiotomography. No attempt was made to tweak the model for better agreement with the observations.

Good agreement was obtained between the modelled and observed densities under conditions of B_z negative with both revealing the effect of the tongue-of-ionisation drawn from the dayside, over the pole and into the nightside. In this instance the SuperDARN electric potentials were derived from measurements made during the time of interest and the convection was representative of the flows throughout the interval. SuperDARN measurements were not available for the time period of radiotomography observations under B_z positive, and electric potentials for a period under similar, stable

conditions were used where the flow resembled that anticipated for B_z northward. In this case a TOI drawn antisunward around the periphery of the polar cap was both modelled and observed. Both cases illustrate the potential of SuperDARN electric potential patterns to improve agreement between the CTIP model and observations.

Chapter 7

Application of the CTIP Model to Interpret Tomographic Imaging from Two Longitude Sectors

7.1 Introduction

Electron density enhancements in the polar cap are observed by a number of techniques such as ionospheric radio tomography, the use of riometers and ionosondes. However with just one technique it is difficult to establish the source of the ionisation so multiple instrumental techniques are used for observation. The exception is when one of a few expensive incoherent scatter radar (e.g. EISCAT) is used as with such instruments it is possible to obtain a large number of different parameters. The disadvantage of these instruments is the limited field of view.

Two main sources of ionisation have been identified: photoionisation and precipitation but these can be further complicated by ionisation being transported from the region of origin to a different region. The ionisation can be modulated by other mechanisms such as in regions of fast flow and when change in the high-latitude convection pattern reconfigures the ionisation. Also the offset in the geomagnetic and geographic reference systems cause different proportions of the convection pattern to be in sunlight at a particular time of interest.

Physical models have been built using physical process that underlie the observations. These models are far from perfect but nevertheless they contain the main physical and chemical processes. Such models are particularly useful in assisting in the interpretation of data especially when multi-instrument data is not available. Recent changes to the CTIP model as described in Chapter 5 allow the high latitude convection patterns to be put in from SuperDARN electric potential data. This means that any SuperDARN convection pattern can be used as input to CTIP rather than relying on a restricted library of patterns. In particular it is now possible to model a wider range of IMF conditions including IMF B_z positive convections. This work has been described in detail in Chapter 6 where tomography images with mature interpretations involving multi-instrument studies were used to validate the use of SuperDARN IMF B_z negative convection patterns and to extend this to IMF B_z positive patterns. The verification of the model with SuperDARN input in the European sector has been given by Whittick et al. (2009) and Pry. The next stage in this process is to use the model to assist in the interpretation of observed data made by a single instrument and in this Chapter this will be done for

observations both in the European sector and the northern high-latitude regions of the Alaskan sector. Alaskan tomography data was taken from the online data index found at `http://www.haarp.alaska.edu/`.

Tomography images were chosen from both the Scandinavian and Alaskan sectors under the conditions of IMF B_z negative and B_z positive where in both cases the IMF had been stable for at least 6 hours prior to the time of interest. To minimise the solar effect the tomography passes were chosen from a time close to the winter solstice. Patches of ionisation are prominent in these tomography images and the CTIP model was used to attempt to identify the source of this ionisation. The two main ionisation production mechanisms considered by the CTIP model are ionisation caused by solar radiation and ionisation formed by precipitation. The ionisation created by both these mechanismns may be transported by the high-latitude convection pattern. By executing a series of model runs using appropriate variables it is possible to determine the likely cause of the ionisation patches seen in the tomography images.

The model was run for day 347, which is the same day that the tomography images were obtained. The solar input or F10.7 value was set to 230, which is representative of the month. The Kp index was kept at 2 throughout the model runs, though it is only relevant to the DMSP precipitation as the Kp index gives an indication of the strength of the precipitation (Foster et al., 1986).

Figure 7.1 shows the main features of the CTIP model with just the solar F10.7 input at 00UT, 06UT, 12UT and 18UT, plotted at a height of 320km. The precipitation input and the high-latitude convection were both switched off. The white line represents the

position of the Scandinavian tomography chain line at 18°E. The 06UT plot shows the least amount of ionisation and as the Sun rises ionisation increases with time as shown in the plots by the red colour. At 18UT, the ionisation levels reach to just below 80°MLAT. However this set of plots show that while the Sun is responsible for an increase in the ionisation levels it is not responsible for any increase that could be observed in radio tomography images in the 0-6UT time sector. This is because in this particular time sector the Scandinavian chain line does not intersect with the increase in ionisation caused by the Sun.

Figure 7.2 is a similar plot but with precipitation turned on. A feature of the CTIP model is that precipitation is either on or off throughout the whole model run. This is in contrast to the known sporadic nature of precipitation in the ionosphere. Previous work (Pryse et al., 2005) has shown that on the whole, precipitation in CTIP produces a higher level of ionisation than in corresponding tomography images. With this in mind, the precipitation and solar plots (i.e. without any high-latitude convection input) for the time of interest would be expected to produce higher levels of ionisation. However, the model is particularly useful for identifying the likely region of precipitation and Figure 7.2 shows this. Once again the lowest level of photoionisation is shown in the 6UT plot with the auroral ionisation being essentially distinct from the ionisation caused by the solar effect. By 18UT, the photoionisation and the auroral ionisation join at the $8.0 \times 10^{11} m^{-3}$ contour level. This time, the Scandinavian chain in the 0-6UT sector clearly intersects a region of precipitation and this indicates that precipitation may be the cause of any enhancements seen in the Scandinavian tomography images from this

time period.

The third element of the CTIP model is the use of SuperDARN high-latitude convection patterns as input which was discussed in detail in Chapter 5. In practical terms, it is the electron potential values defined on a grid that are put into the model. These values represent the convection pattern in CTIP. For each tomography pass, a representative convection pattern, i.e. one taken from the SuperDARN website that best represents the general shape of the convection at the time of interest, is taken and used as input for the CTIP model. In the results section, the effect of each of these convection patterns together with the interaction with the precipitation is discussed in detail.

7.2 IMF B_z Negative

7.2.1 Scandinavia

Figure 7.3 shows each component of the IMF as measured by the ACE spacecraft. The plot indicates that the IMF B_z component was stable and negative for the six hours prior to the time of interest, from 18UT on 12 December 2001. The tomography images were taken at 0007UT, 0156UT and 0243UT on 13 December 2001, where the IMF continued to be stable and negative. This is important because the stability of the B_z component of the IMF is related to the stability of a particular convection pattern. To provide a clear-cut case for modelling purposes it was necessary to choose a period of time that provided a stable IMF in order for the convection pattern to remain as similar as possible during the time of interest. In addition, it was necessary to find such a time

of interest which contained a number of tomography passes so that it would be possible to trace the particular features of the image over time.

The three Scandinavian tomography images are shown in Figure 7.4. In each of the three passes there is a clear enhancement suggesting that the enhancement is real rather than an anomaly in the data. The location of the major enhancement in the 0007UT pass is between 64 – 74°GLAT with a maximum density of $8 \times 10^{11} m^{-3}$ at between 66 – 73°GLAT. With the second pass taken at 0156UT the major enhancement spans 6.5° starting at 63.5° and finishing at 71°GLAT with a maximum electron density of $6 \times 10^{11} m^{-3}$ at between 65 – 67°GLAT. Finally the third pass at 0243UT shows a maximum enhancement at a level of $5 \times 10^{11} m^{-3}$ at about 62–65°GLAT. So it can be seen from the data that there is a consistent enhancement occurring in the time of interest. The aim of the modelling is to see what is the cause of this enhancement. The theory tells us that it the main possibilities are either solar production, in-situ precipitation or some combination of both with the convection pattern moving around ionisation created by either by the sun as photoionisation or by precipitation transported to the site of interest. By isolating each factor in the model it is possible to show the extent to which each of these components influence the overall electron density. It should be noted here that the tomography images measure electron density but the CTIP model calculates the O^+ density, which is equivalent to the electron density in the F-region of the ionosphere.

Figure 7.5 shows the CTIP model output with just the solar input set at an F10.7 value of 230 for the time of interest. The white line shown on each dial plot represents

the approximate location of the Scandinavian radio tomography chain. As, during the time of interest, the position of the tomography chain does not at any point coincide with the increased ionisation due to the solar effect, these plots show that the solar input alone is not responsible for the enhancements shown in the tomography images.

To examine the effect of the convection, a suitable SuperDARN convection pattern was chosen to provide the high-latitude electric potential CTIP input. As the IMF B_z component is negative and stable both prior to and during the time of interest the actual shape of the convection pattern as determined by SuperDARN during the time of interest is very similar. Therefore, the convection pattern for 0240UT was picked as a representative pattern. It is shown in Figure 7.6. Clearly there are a number of key features of this pattern, but most obviously it is a two-cell convection pattern causing the flow to move anti-sunward across the polar cap with the return flow being at lower latitudes.

Figure 7.7 shows the CTIP model output for the time of interest with both solar and convection pattern inputs. By looking at where the Scandinavian chain line (marked in white) intersects with the regions of enhanced ionisation, it can be seen that the tomography chain is in the right place to observe the plasma being swept across the polar cap by the high-latitude convection pattern. However the third key input to the CTIP model, the precipitation input, needs to be considered before crediting the enhancements in the tomography to the convection pattern alone.

Figure 7.8 shows a similar set of model plots with the solar input and the DMSP precipitation input. The plots show different regions of enhancements based on the

model's positioning of the auroral oval.

In general the region of enhancement in the tomography images is at latitudes lower than the altitude of precipitation identified in the model run. This suggests that it is important to look at the effect of convection as it is not possible for the enhancements to be caused by in-situ precipitation; however it might be the case that the enhancement has been caused by precipitation being convected into the region of interest. The latitude scale has been extended down to 50°MLAT for interpretation purposes. On the duskward side of each plot there are some angular lines that are associated with the coupling of the open and closed flux tubes. However as this region is not coincident with the region of interest as marked in white by the chain line it does not affect the reliability of the model densities obtained for the purposes of this study.

7.2.2 Alaska

Figure 7.9 is a plot of IMF starting at about 03UT on 11 December 2001 showing that the IMF B_z component is stable and negative. While it would have been ideal to have used exactly the same day as in the Scandinavian case study, there was insufficient Alaskan tomography data for the 11-12 December 2001. As we are looking at a different longitude, the time where it is expected that we see a tongue of ionisation is around 09-15UT and so the IMF was checked for stability 6 hours prior to this, as with the European case study. The convection pattern used was the same as with the Scandinavian case study. The justification for this is that B_z negative convection patterns are very similar in that they consist of two cells with the flow being brought across the polar cap

forming the tongue of ionisation and the flow returning at lower latitudes.

Three Alaskan tomography images were used in this part of the study taken at 0927UT, 1147UT and 1424UT as shown in Figure 7.10. The 0927UT image has a maximum enhancement at about 64°MLAT. The 1147UT image has a maximum slightly poleward of this, at about 67°MLAT and the 1424UT plot again has another enhancement at about 67°MLAT. Both the 1147UT and 1124UT plots show E-region precipitation characterised by the ionisation at around 100km. The CTIP model run that deals with precipitation and solar effects enables the region of precipitation in the Alaskan chain to be determined.

Figure 7.11 shows the CTIP model output for the solar effect plotted at the time of interest for the Alaskan tomography. As with the Scandinavian tomography, the approximate location of the Alaskan tomography chain line at 216°E is marked on each dial plot. These plots show that it is not possible for the enhancements seen in the tomography to be caused solely by photoionisation as the region of interest indicated by the chain line on the polar plots is not coincident with the region of increased ionisation seen in the tomography images. This means that the enhancements seen in the tomography must be caused by either precipitation or convection or a combination of both.

Figure 7.12 shows the CTIP model output with solar input and high-latitude convection at the time of interest. Again, the white line represents the approximate position of the Alaskan chain line and by looking at where this intersects the enhanced region of ionisation formed by the tongue of ionisation being swept anti-sunward across the

polar cap as a result of the convection input it is possible to indicate whether or not the convection component of the CTIP model makes a contribution to the density enhancements observed by the radio tomography experiment. The 09UT and 10UT dial plots show that the chain line does not intersect with the tongue of ionisation whereas later in the day the 11UT and 12UT plots indicate a possible intersection with the $2.0 \times 10^{11} m^{-3}$ contour level approaching the location of the chain line at 85°MLAT in the 13UT plot suggesting that the enhancement observed in the 1147UT tomography pass could be due in part to convection. The final dial plot in this group shows that by 14UT the Alaskan chain is in the ideal position to observe the tongue of ionisation being swept across the polar cap, as in this image the $2.0 \times 10^{11} m^{-3}$ contour level of electron density coincides with the Alaskan chain line poleward of 75°MLAT.

To determine whether or not the enhancement at $63 - 64.5$°MLAT in the 0927UT tomography plot is produced in-situ or transported by the convection flow, the location of the auroral oval and the Alaskan chain line at the time of interest can be examined. Figure 7.13 shows a series of CTIP model plots showing the electron density for the combined effect of the solar input and the DMSP precipitation. By comparing the location of the aurora oval at the Alaskan chain position at 09UT and 10UT it is clear that as the chain line representing the location of the Alaskan chain does not intersect with the position of the auroral oval. This indicates that the precipitation in this pass is not created in-situ, rather it is transported. This can be confirmed by looking at the 09UT and 10UT plots for the precipitation, convection and solar model run in Figure 7.13 which shows that the precipitation has been transported by the convection into the re-

gion where the Alaskan chain is situated. The 1147UT tomography pass contains some evidence of E-region precipitation, shown by the enhanced ion densities polewards of 67°MLAT. The corresponding model plots for 11UT and 12UT showing the solar and precipitation effect indicate that the Alaskan chain line intersects the auroral oval and which suggests that the enhancement seen in the tomography is partly due to precipitation. Examination of Figure 7.14 which shows the CTIP model output with solar, precipitation and convection included suggests that it is possible that the convection has transported some of the plasma to the location observed by the tomography image. The 1424UT tomography pass has larger F-region electron densities than in the other two tomography passes as well as some E-region precipitation. It is likely that this has been produced in-situ as the Alaskan tomography chain is in the right place to observe enhancements cause by the auroral oval. However the adding in the convection input as shown in Figure 7.14 suggests that since the 14UT polar plot shows the Alaskan chain line very close to intersecting the tongue of ionisation it is possible that some of this plasma has been transported to its final location as observed in the tomography image.

7.3 IMF B_z Positive

The third case study is the start of extending this work into looking at the condition of IMF B_z positive. As the use of SuperDARN electric potential patterns has been established as a possible method of expanding the number and type of convection patterns in the CTIP model, it is now possible to use SuperDARN patterns to model any type of convection pattern, specifically IMF B_z positive.

7.3.1 Scandinavia

As Figure 7.15 shows, the IMF B_z component is stable and positive from 18UT on 17 December 2002. The time of interest for this study is 00UT-06UT on 18 December 2002. It would have been better to have had data from December 2001 to match more closely with the IMF B_z negative case studies however none was available close to the 2002 dates. The next best thing is to look at data from the same time of the year but in an adjacent year. This ensures that the solar effect is similar both in the time of year and in the position of the solar cycle.

Three Scandinavian tomography images were used from the 18 December 2002, 0050UT, 0240UT and 0615UT. These are shown in Figure 7.16. The main enhancement in the 0050UT image is poleward of 79.5°GLAT at an electron density contour level of $2.0 \times 10^{11} m^{-3}$. This feature is seen in the 0240UT image poleward of 73°GLAT with peak electron density of $5.0 \times 10^{11} m^{-3}$ at between $80.5 - 83.5$°GLAT. Finally in the 0615UT image the enhancement is observed poleward of 73°GLAT with a peak electron density of $6.0 \times 10^{11} m^{-3}$ between $79 - 80$°GLAT.

Figure 7.17 shows the CTIP model output covering the range of times where tomography images were obtained. The location of the Scandinavian tomography chain is show by the white line and it is clear that there is no contribution from photoionisation in the model as the chain line position is in the wrong place to observe the solar effect in the model.

The position of the auroral oval at the time of interest is given in Figure 7.18. The position of the Scandinavian tomography chain indicated by the white line intersects the

position of the auroral oval at the time of interest suggesting that in-situ precipitation contributes to the density enhancements observed in the tomography images.

As the high-latitude convection patterns for the time of interest are for IMF B_z positive, there is a lot of variation in the different electric potential patterns, as shown in Figure 7.19. Each of these three convection patterns were used in turn as the high-latitude CTIP model input because the variability of the patterns means that it was difficult to choose any one representative pattern with confidence.

Figures 7.20, 7.21, and 7.22 show CTIP model output for the time corresponding to the tomography passes obtained. In each case, in addition to the solar F10.7 input, a different convection pattern is used, demonstrating that even quite small changes in the electric potential values result in changes to the electron density distribution. This suggests that selecting the correct convection pattern from the SuperDARN database is important when specific model runs are being done to assist with the interpretation of tomography data.

Figures 7.23, 7.24 and 7.25, show CTIP model output with a different convection pattern but this time with DMSP precipitation added. With the convection effect included, the effect of direct precipitation is naturally reduced, but the combined effect of the precipitation and convection gives a maximum on the dawn side for all the convection patterns. This geographical intensification is seen in the Scandinavian images with the largest density being the 0615UT plot.

7.3.2 Alaska

Figure 7.26 show two Alaskan tomography images taken from 18 December 2002 where the IMF B_z component was stable and positive. In both images a consistent enhancement is seen poleward of 69°MLAT. Corresponding CTIP model output with just the solar input is shown in Figure 7.27 shows that the Alaskan chain line does not intersect with the solar ionisation suggesting that the enhancements shown in the tomography must be cause by something other than the solar effect alone.

Figure 7.28 shows the added effect of the DMSP precipitation with $Kp = 1$. The Alaskan chain intersects the auroral oval suggesting that precipitation may be the cause of the enhancements seen in the tomography images. To examine the impact of the high-latitude convection, a different convection pattern was used as with the Scandinavian modelling, again because of the high amount of variability in the IMF B_z positive convection patterns. Figure 7.29 shows a comparison of the two different convection patterns. By looking at the red contour level which is an electron density of $8.0 \times 10^{11} m^{-3}$, it can be seen that the amount of plasma being convected across the polar cap is much reduced when compared to modelled electron densities under IMF B_z negative conditions. Further, the difference between the two IMF B_z positive convection patterns used in Figure 7.29 is responsible for the differing amounts of plasma visible at later UTs. For example, at 15UT, the red contour level (representing an electron density of $8.0 \times 10^{11} m^{-3}$) is much more angular with the 1138UT convection than in the 1500UT convection.

Finally Figure 7.30 shows the impact of adding DMSP precipitation again, one

row of plots for each of the two convection patterns. The DMSP precipitation level is $Kp = 1$. Here the different convection patterns account for the change in the plasma distribution. Figures 7.29 and 7.30 show that even with small variations in the SuperDARN electric potential patterns that are used as the high-latitude convection input in CTIP, there is a marked difference in the modelled plasma distribution.

7.4 Conclusion

This work has shown that it is possible to use the CTIP model with SuperDARN high-latitude input in order to assist with the interpretation of radio tomography data where there is a lack of alternative instrumentation. It is clear from the variation in the nature of the IMF B_z positive convection that this has an impact on the modelled electron densities in the CTIP model. The extension of the CTIP model to include SuperDARN electric potentials has expanded the number of situations where the model can be used to interpret data in several different longitudes.

Chapter 8

Conclusion

8.1 Conclusion

The studies presented in this thesis have shown that the interpretation of the high latitude plasma density distribution can be greatly enhanced by using the CTIP model with SuperDARN electric potentials as the high-latitude input. This development to the model has enabled both IMF B_z negative and positive conditions to be represented. Initially this method was verified by comparing tomography data that has a mature multi-instrument interpretation with the CTIP model output obtained by using SuperDARN input. It was found that there was a good agreement between the modelled and observed densities under the conditions of IMF B_z negative with both showing the effect of the tongue-of-ionisation drawn from the dayside over the polar cap and into the nightside. In the IMF B_z positive case, both the CTIP model output and the data observations showed the tongue-of-ionisation being drawn anti-sunward around the pe-

riphery of the polar cap. These two case studies serve to illustrate the potential of the use of SuperDARN electric potential patterns to improve the agreement between the CTIP model and the observations. As a result of this, the CTIP model has been used to interpret the high-latitude plasma distribution in locations such as Alaska where additional instrumentation is less widely available to assist with the interpretation of the radio tomography data. Systematic use of the CTIP model involving isolating the three key input parameters, solar flux, precipitation and high-latitude convection represented by electric potential values, made it possible to determine the likely cause of some of the density enhancements observed in the data.

8.2 Future Work

There are three possible areas of future work that arise directly from this thesis: First, there is scope for further case studies involving other sets of tomographic images taken from periods of stable IMF B_z, perhaps from times of the year other than the winter solstice, which has been the focus for this work. While there is nothing in the modelling side of the work that would suggest that the new development would be less effective at other times of the year, the addition of more sunlight to the polar cap creates different challenges in interpreting the data. Also the model could be used to investigate the influence of the solar cycle by looking at winter solstice data from a variety of points in the solar cycle to see if changing the F10.7 value has any impact on how the convection pattern redistributes the plasma in the polar cap. All of the studies in this thesis have been under quiet geomagnetic conditions (Kp values of 1 or 2) so choosing case studies

with more active geomagnetic conditions would be an interesting comparison with the studies presented in this thesis.

The second area of further study is to collect a large number of tomographic images over a number of months and seek to classify them by IMF B_z component and identify particular patterns in the images. For example, in a particular month all the tomography images that occur under a certain stable IMF condition may contain similar characteristics that could be parameterised in a similar way to the study conducted by Pryse et al. (2006a) where the main ionospheric trough was parameterised so that the experimental observations can be used for direct comparison and validation of ionospheric models. Once the tomography data has been parameterised, the different conditions of IMF, solar flux and precipitation can be modelled with CTIP to identify the likely cause of the particular features identified in each IMF condition.

The third area of further study resulting from this thesis has more of a modelling slant: all the high-latitude convection patterns in the form of electric potentials in this thesis have been inputted into CTIP in "steady state", that is, one set of electric potential patterns is deemed sufficient to represent the entire day of interest. In the ionosphere, the electric potential values and with it the corresponding convection patterns change moment by moment. Reference has been made in Chapter 5 to the potential of the CTIP model to vary the high-latitude input every 12 minutes, by loading 7 different electric potential patterns into the model and using a grid to call a different pattern every 12 minutes. This is not completely time-varying but it goes some way towards a system of high-latitude convection input that is more realistic than the present one. Using several

different convection patterns as described in Chapter 5 would enable a clear-cut switch in the IMF B_z orientation to be modelled. With suitable tomography data this technique could be verified. Ultimately the best way to get genuine time-varying high-latitude input into the CTIP model is to find a method of extracting the SuperDARN electric potential data from the internet and loading it into CTIP every few minutes. This would probably warrant a fairly major re-write in the CTIP code to enable the model to process such a large volume of data but this enhancement would take the model from being used as a forecasting tool to a model that is potentially able to simulate the ionosphere near to real time. Even if this is too ambitious a project, it would be very useful to assist with interpretation of older data sets for the CTIP model to be able to accept a large sequence of electric potential patterns.

Finally, one further area for modelling development is that of particle precipitation. The weakness of the particle precipitation routine in CTIP is that it is either switched on or switched off. In the ionosphere, precipitation is much more sporadic. Using a similar technique to that of including SuperDARN electric potential patterns, it would be possible to investigate the inclusion of a more realistic precipitation input, perhaps using data from the auroral Oval Variation, Assessment, Tracking, Intensity and Online Nowcasting (OVATION) system (`http://sd-www.jhuapl.edu/Aurora/ovation/index.html`) which could be read in at regular intervals by CTIP.

Both the studies presented in this thesis and the suggestions for future work indicate that the development of the CTIP model to include high-latitude input from SuperDARN is an important step in the progress of large-scale ionospheric modelling. While

there is much work left to do in testing this technique across a range of different geophysical conditions as outlined above, it has the potential to be a useful addition to assist with the interpretation of ionospheric data.

Bibliography

Anderson, D. N., Mendillo, M., and Herniter, B., A semi-empirical low-latitude ionospheric model, *Radio Sci.*, *22*, 292–306, 1987.

Anderson, D. N., Buchan, J., and Heelis, R. A., Origin of density enhancements in the winter polar cap ionosphere, *Radio Sci.*, *23*, 513–519, 1988.

Anderson, D. N., Decker, D. T., and Valladares, C. E., Global Theoretical Ionospheric Model (GTIM), pp. 133–150, 1996.

Andreeva, E. S., A. V. Galinov, A. V., V. E. Kunitsyn, V. E., Mel'nichenko, Y. A., Tereshchenko, E. D., Filimonov, M. A., and Chernykov, S. M., Radiotomographic reconstruction of ionisation dip in the plasma near the earth, *J. Exp. Theor. Phys. Lett.*, *52*, 145–148, 1990.

Austen, J., Franke, S., Liu, C., and Yeh, K., Application of computerised tomography techniques to ionospheric research, in *International Beacon Satellite Symposium, University of Oulu, Finland,*, edited by A. Tauriainen, pp. 25–35, 1986.

Austen, J. R., Franke, S. J., and Liu, C. H., Ionospheric imaging using computerised tomography, *Radio Sci.*, *23*, 299–307, 1988.

Axford, W. I. and Hines, C., A unifying theory of high-latitude geophysical phenomena and geomagnetic storms, *Canadian Journal of Physics*, *39*, 1433, 1961.

Bailey, G., The effect of a meridional ExB drift on the thermal plasma at l=1.4, *Planetary and Space Science*, *31*, 389–409, 1983.

Bilitza, D., International reference ionosphere 1990, *National Space Science Data Centre*, *Ref. 90-20*, 1990.

Bowline, M. D., Sojka, J. J., and Schunk, R. W., Relationship of theoretical patch climatology to polar cap patch observations, *Radio Sci.*, *31*, 635–644, 1996.

Bradley, P. A. and Dudeney, J. R., A simple model of the vertical distribution of electron concentration in the ionosphere, *J. Atmos. Terr. Phys.*, *35*, 21312146, 1973.

Brekke, A., *Physics of the Upper Polar Atmosphere*, John Wiley and Sons Ltd in association with Praxis Publishing Ltd, 1997.

Brinton, H., Grebowsky, J., and Brace, L., The high-latitude winter F region at 300km: Thermal plasma observations from AE-C, *J. Geophys. Res.*, *83*, 47674776, 1978.

Buchau, J., Reinisch, B. W., Weber, E. J., and Moore, J. G., Structure and dynamics of the winter polar cap F-region, *Radio Sci.*, *18*, 995–1010, 1983.

Chisham, G., Lester, M., Milan, S. E., freeman, M. P., Bristow, W. A., Grocott, A., MacWilliams, K. A. Ruohoniemi, J. M., Yeoman, T. K., Dyson, P., Greenwald, R. A., Kikuchi, T., Pinnock, M., Rash, J., Sato, N., Sofko, G., Villain, J.-P., and Walker, A. D. M., A decade of the Super Dual Auroral Radar Network (SuperDARN): Scientific achievements, new techniques and future directions, *Surveys in Geophysics*, *28*, 33–109, 2007.

Chiu, Y., An improved phenomenological model of ionospheric density, *J. Atmos. Terr. Phys.*, *37*, 1563, 1975.

Cowley, S. W. H., Excitation of flow in the Earth's magnetosphere-ionosphere system: observations by incoherent scatter radar, in *Polar Cap Boundary Phenomena*, edited by J. Moen, vol. 509 of *NATO Advanced Study Institude Series*, pp. 127–140, Kluwer Academic Press, The Netherlands, 1998.

Cowley, S. W. H., Morelli, J. P., and Lockwood, M., Dependence of convective flows and particle precipitation in the high-latitude dayside ionosphere on the x and y components of the interplanetary magnetic field, *J. Geophys. Res.*, *10*, 103–115, 1992.

Crooker, N. U., Reverse convection, *J. Geophys. Res.*, *97*, 19 363–19 372, 1992.

Croom, S., Robbins, A., and Thomas, J. O., Variation of electron density in the ionosphere with magnetic dip, *Nature*, *185*, 902–903, 1960.

Crowley, G., Critical review of ionospheric patches and blobs, in *URSI Review of Radio Science 1993-1996*, edited by W. R. Stone, pp. 619–648, 1996.

Daniell, R. E., Brown, L. D., Anderson, D. N., Fox, M. W., Doherty, P. H., Decker, D. T., Sojka, J. J., and Schunk, R. W., Parameterized ionospheric model: A global ionospheric parameterization based on first principles models, *Radio Sci.*, *30*, 1499–1510, 1995.

de la Beaujardiere, O., Wickwar, V. B., Kelly, J. D., and King, J. H., Effect of the interplanetary magnetic field y component on the high-latitude nightside convection, *Geophys. Res. Lett.*, *12*, 461–464, 1985.

Di Giovanni, G. and Radicella, S. R., An analytical model of the electron concentration profile in the ionosphere, *Adv. Space Res.*, *10*, 27–30, 1990.

Dungey, J. W., Interplanetary magnetic field and the auroral zones, *Phys. Rev. Lett.*, *6*, 47, 1961.

Foster, J. C., Holt, J. M., and Musgrove, R. G., Ionospheric convection associated with discrete levels of particle precipitation, *Geophys. Res. Lett.*, *13*, 656–659, 1986.

Fremouw, E., Secan, J., and Howe, B., Application of stochastic inverse theory to ionospheric tomography, radio science, *Radio Sci.*, *27*, 721732, 1992.

Fremouw, E., Secan, J., Bussey, R., and Howe, B., A status report on applying discrete inverse theory to ionospheric tomography, *Int. J. Imag. Syst. Tech*, *5*, 97–105, 1994.

Fuller-Rowell, T. and Rees, D., A three dimensional, time-dependent, global model of the thermosphere, *J. Atmos. Sci.*, *37*, 2545–2567, 1980.

Fuller-Rowell, T., Rees, D., Quegan, S., Bailey, G., and Moffett, R., The effect of realistic conductivities on the high-latitude neutral thermospheric circulation, *Planetary Space Sciences*, *32*, 469–480, 1984.

Fuller-Rowell, T., Rees, D., Quegan, S., and Moffett, R., Numerical simulations of the sub-auroral F-region trough, *J. Atmos. Terr. Phys.*, *53*, 529–540, 1991b.

Fuller-Rowell, T., Rees, D., Quegan, S., Moffett, R., and Bailey, G., Simulations of the seasonal and universal time variations of the high-latitude thermosphere and ionosphere using a coupled, 3-dimensional, model, *Pure and Applied Geophysics*, *127*, 189–217, 1998.

Fuller-Rowell, T. J. and Rees, D., Derivation of a conservative equation for mean molecular weight for a two-constituent gas within a three-dimensional, time-dependent model of the thermosphere, *Planet. Space Sci.*, *31*, 1209–1222, 1983.

Fuller-Rowell, T. J., Rees, D., Quegan, S., Moffett, R. J., and Bailey, G. J., Interactions between neutral thermospheric composition and the polar ionosphere using a coupled ionosphere-thermosphere model, *J. Geophys. Res.*, *92*, 7744–7748, 1987.

Fuller-Rowell, T. J., Moffett, R. J., Quegan, S., Rees, D., Codrescu, M. V., and Millward, G. H., A coupled thermosphere-ionosphere model (CTIM), pp. 217–233, 1996.

Greenwald, R. A., Baker, K. B., Dudeney, J. R., Pinnock, M., Jones, T. B., Thomas, E. C., villain, J. P., Cerisier, J. C., Senior, C., Hanuise, C., Hunsucker, R., Sofko, G., Koehler, J., Nielsen, E., Pellinen, R., Walker, A. D. M., Sato, N., and Yamagishi, H., Darn/Superdarn: a global view of the dynamics of high-latitude convection, *Space Sci. Rev.*, *71*, 761–796, 1995.

Hargreaves, J. K., *The Solar-Terrestrial Environment*, Cambridge, 1992.

Heaton, J., Pryse, S. E., and Kersley, L., Improved background representation, ionosonde input and independent verification in experimental ionospheric tomography, *Ann. Geophysicae*, *13*, 1297–1302, 1995.

Kak, A. C. and Slaney, M., *Principles of computerised tomographic imaging*, IEEE Press, New York, 1987.

Kersley, L. and Pryse, S. E., Development of experimental ionospheric tomography, *Int. J. Imaging Syst. Technol.*, *5*, 141–147, 1994.

Kersley, L., Heaton, J., Pryse, S. E., and Raymund, T., Experimental ionospheric tomography with ionosonde input and EISCAT verification, *Ann. Geophysicae*, *11*, 1064–1074, 1993.

Kersley, L., Pryse, S. E., Walker, I. K., Heaton, J. A. T., Mitchell, C. N., Williams, M. J., and Wilson, C. A., Imaging of electron density troughs by tomographic techniques, *Radio Sci.*, *32(4)*, 1607–1621, 1997.

Lathuillre, C., Menvielle, M., Lilensten, J., Amari, T., and Radicella, S. M., From the Suns atmosphere to the Earths atmosphere: an overview of scientific models available for space weather developments, *Annales Geophysicae*, *20*, 1081–1104, 2002.

Lilensten, L. and P.L. Blelly, P. L., The TEC and F2 parameters as tracers of the ionosphere and thermosphere, *J. Atmos. Terr. Phys.*, *64*, 775–793, 2002.

Lockwood, M., Solar wind-magnetosphere coupling, in *Proceedings of the EISCAT International School*, Cargése, Corsica, 1995.

McIlwain, C. E., Coordinates for mapping the distribution of magnetically trapped particles, *J. Geophys. Res.*, *66*, 3681–3691, 1961.

Middleton, H. R., Pryse, S. E., Kersley, L., Bust, G. S., Fremouw, E. J., Secan, J. A., and Denig, W. F., Evidence for the tongue of ionisation under northward IMF conditions, *J. Geophys. Res.*, *110*, A07 301, 2005.

Middleton, H. R., Pryse, S. E., Wood, A. G., and Balthazor, R. L., The role of the tongue-of-ionisation in the formation of the poleward wall of the main trough in the European post-midnight sector, *J. Geophys. Res.*, *113*, 2008.

Milan, S. E., Lester, M., and Yeoman, T. K., Polar patch formation revisited, summer and winter variations in dayside plasma structuring, *Ann. Geophysicae*, *20*, 487–499, 2002.

Millward, G., Quegan, S., Moffett, R., Fuller-Rowell, T., and Rees, D., A modelling study of the coupled ionospheric and thermospheric response to an enhanced high-latitude electric-field event, *Planetary and Space Science*, *41*, 45–56, 1993.

Millward, G., Mller-Wodarg, I., Aylward, A., Fuller-Rowell, T., Richmond, A., and Moffett, R., An investigation into the influence of tidal forcing on F-region equatorial vertical ion drift using a global ionosphere-thermosphere model with coupled electrodynamics, *J. Geophys. Res*, *106*, 24 733–24 744, 2001.

Millward, G. H., Moffett, R. J., Quegan, S., and Fuller-Rowell, T. J., A coupled thermosphere-ionosphere-plasmasphere model (CTIP), pp. 239–279, 1996a.

Millward, G. H., Rishbeth, H., Fuller-Rowell, T. J., Aylward, A. D., Quegan, S., and Moffett, R. J., Ionospheric F2 layer seasonal and semiannual variations, *J. Geophys. Res.*, *101*, 51495156, 1996b.

Millward, G. H., Moffett, R. J., and Balmforth, H. F., Modelling the ionospheric effects of ion and electron precipitation in the cusp, *J. Geophys. Res.*, *104*, 24 603–24 612, 1999.

Mitchell, C. N., Pryse, S. E., Kersley, L., and Walker, I. K., The correction for the satellite-receiver longitude difference in ionospheric tomography, *J. Atmos. Terr. Phys.*, *59*, 2007–2087, 1997.

Newell, P. T. and Meng, C.-I., Mapping the dayside ionosphere to the magnetosphere according to particle precipitation characteristics, *Geophys. Res. Lett.*, *19*, 609–612, 1992.

Parker, E. N., Dynamics of the interplanetary gas and magnetic fields, *J. Astrophys.*, *128*, 664, 1958.

Pryse, S. E., Radiotomography: A new experimental technique, *Surveys in Geophysics*, *24*, 1–38, 2003.

Pryse, S. E. and Kersley, L., A preliminary experimental test of ionospheric tomography, *J. Atmos. Terr. Phys.*, *54*, 1007–1012, 1992.

Pryse, S. E., Kersley, L., Rich, D., Russell, C., and Walker, I., Tomographic imaging of the ionospheric midlatitude trough, *Ann. Geophysicae*, *11*, 144–149, 1993.

Pryse, S. E., Kersley, L., Mitchell, C. N., Spencer, P. S. J., and Williams, M. J., A comparison of reconstruction techniques used in ionospheric tomography, *Radio Sci.*, *33*, 1767, 1998a.

Pryse, S. E., Kersley, L., Mitchell, C. N., Spencer, P. S. J., and Williams, M. J., A comparison of reconstruction techniques used in ionospheric tomography, *Radio Sci.*, *33*, 1767–1779, 1998b.

Pryse, S. E., Smith, A. M., Walker, I. K., and Kersley, L., Multi-instrument study of footprints of magnetopause reconnection in the summer ionosphere, *Ann. Geophysicae*, *18*, 1118–1127, 2000.

Pryse, S. E., Dewis, K. L., Balthazor, R. L., Middleton, H. R., and Denton, M. H., The dayside high-latitude trough under quiet geomagnetic conditions: Radiotomography and the CTIP model, *Ann. Geophysicae*, *23*, 1199–1206, 2005.

Pryse, S. E., Kersley, L., Malan, D., and Bishop, G. J., Parameterization of the main ionospheric trough in the european sector, *Radio Sci.*, *41*, 2006a.

Pryse, S. E., Wood, A. G., Middleton, H. R., McCrea, I. W., and Lester, M., Reconfiguration of polar-cap plasma in the magnetic midnight sector, *Ann. Geophysicae*, *24*, 2201–2208, 2006b.

Quegan, S., Bailey, G. J., Moffett, R. J., Heelis, R. A., Fuller-Rowell, T. J., Rees, D., and Sprio, R. W., A theoretical study of the distribution of ionisation in the high-latitude ionosphere and the plasmasphere: first results on the mid-latitude trough and the light-ion trough, *J. Atmos. Terr. Phys.*, *44*, 619–640, 1982.

Radon, J., ber die bestimmung von funktionen durch ihre integralwerte lngs gewisser mannigfaltigkeiten, *Berichte ber die Verhandlungen der Schsische Akademie der Wissenschaften*, *69*, 262–277, 1917.

Raymnund, T. D., Comparisons of several ionospheric tomography algorithms, *Ann. Geophysicae*, *13*, 1241–1330, 1995.

Raymund, T., Austen, J., Franke, S., Liu, C., Klobuchar, J., and Stalker, J., Application of computerised tomography to the investigation of ionospheric structures, *Radio Science*, *25*, 771789, 1990.

Raymund, T., Pryse, S., Kersley, L., and Heaton, J., Tomographic reconstruction of ionospheric electron-density with European Incoherent-Scatter radar verification, *Radio Science*, *28*, 811–817, 1993.

Rees, M. H., *Physics and chemistry of the upper atmosphere*, Cambridge University Press, 1989.

Richard, P. G. and Torr, D. J., The Field Line Interhemispheric Plasma Model, pp. 207–216, 1996.

Rino, C. L., Livingston, R. C., T., T. R., Robinson, R. M., Vickrey, J. F., Senior, C., Owen, J., and Klobuchar, J. A., Recent studies of the structure and morphology of auroral zone F region irregularities, *Radio Sci.*, *18(6)*, 1167–1180, 1983.

Rodger, A. S., Moffett, R. J., and Quegan, S., The role of ion drift in the formation of ionospheric troughs in the mid- and high-latitude ionosphere - a review, *J. Atmos. Terr. Phys.*, *54*, 1–30, 1992.

Rodger, A. S., Pinnock, M., Dudeney, J, R., Baker, K. B., and Greenwald, R. A., A new mechanism for polar patch formation, *J. Geophys. Res.*, *99*, 6425–6436, 1994.

Ruohomiemi, J. M. and Baker, K. B., Large-scale imaging of high-latitude convection with Super Dural Auroral Radar Network HF radar observations, *J. Geophys. Res.*, *103*, 20 797–20 811, 1998.

Ruohomiemi, J. M. and Greenwald, R. A., Statistical patterns of high-latitude convection obtained from Goose Bay HF radar observations., *J. Geophys. Res.*, *101*, 21 74321 763.

Sandholt, P. E., Farrugia, C. J., Moen, J., Noraberg, O., Lybekk, B., Sten, T., and Hansen, T., A classification of dayside auroral forms and activities as a function of interplanetary magnetic field orientation, *J. Geophys. Res.*, *103*, 23 325–23 345, 1998.

Schoendorf, J., Aylward, A. D., and Moffett, R. J., Modelling high-latitude electron densities with a coupled thermosphere-ionosphere model, *Ann. Geophysicae*, *14*, 1391–1402, 1996.

Schunk, R. W., Mathematical structure of transport equations for multispecies flows, *Reviews of Geophysics*, *15*, 429–445, 1977.

Schunk, R. W., Theoretical developments on the causes of ionospheric outflow, *J. Atmos. Terr. Phys.*, *62*, 399–420, 2000.

Schunk, R. W. and Sojka, J. J., Ionosphere-thermosphere space weather issues, *J. Atmos. Terr. Phys.*, *58*, 1527–1574, 1996.

Siscoe, G., The magnetosphere: A union of independent parts, *Eos Trans. AGU*, *72(45)*, 494–498, 1991.

Smith, A. M., Pryse, S. E., and Kersley, L., Polar patches observed by ESR and their possible origin in the cusp region, *Ann. Geophysicae*, *18*, 1043–1053, 2000.

Sojka, J. J., Bowline, M. D., Schunk, R. W., Decker, D. T., Valladares, C. E., Sheehan, R., N., A. D., and Heelis, R. A., Modelling polar-cap F-region patches using time-varying convection, *Geophys. Res. Lett.*, *20*, 1783–1786, 1993.

Spencer, P. S. J., Kersley, L., and Pryse, S. E., A new solution to the problem of ionospheric tomography using quadratic programing, *Radio Sci.*, *33*, 607–616, 1998.

Tsunoda, R. T., High-latitude F region irregularities: A review and synthesis, *Rev. Geophys.*, *26*, 719760, 1987.

Valladares, C. E., Basu, S., Buchau, J., and Friis-Christensen, E., Experimental evidence for the formation and entry of patches into the polar cap, *Radio Sci.*, *29*, 167–194, 1994.

Weber, E. J., Buchau, J. G., Moore, J. R., Sharber, R. C., Livingstone, J. D., Winningham, J. D., and Reinisch, B. W., F-layer ionisation patches in the polar cap, *J. Geophys. Res.*, *89*, 1683–1694, 1984.

Whittick, E. L., Pryse, S. E., Middleton, H. R., Lotinga, A. R., and Aylward, A. D., The CTIP model with SuperDARN electric potential patterns as input: first comparison of modelled ion densities with radio tomography observations, *Earth, Moon and Planets*, *104(1)*, 45–49, 2009.

Winser, K. J., Lockwood, M., Jones, G. O. L., Rishbeth, H., and Ashford, M. G., Measuring ion temperatures and studying the ion energy balance in the high-latitude ionosphere, *J. Atmos. Terr. Phys.*, *52*, 501–517, 1990.

Zou, L., Rishbeth, H., Muller-Wodarg, I. C. F., Aylward, A. D., Millward, G. H., Fuller-Rowell, T. J., W., I. D., and Moffett, R. J., Annual and semiannual variations in the ionospheric F2-layer. I. modelling, *Ann. Geophysicae*, *18*, 927–944, 2000.

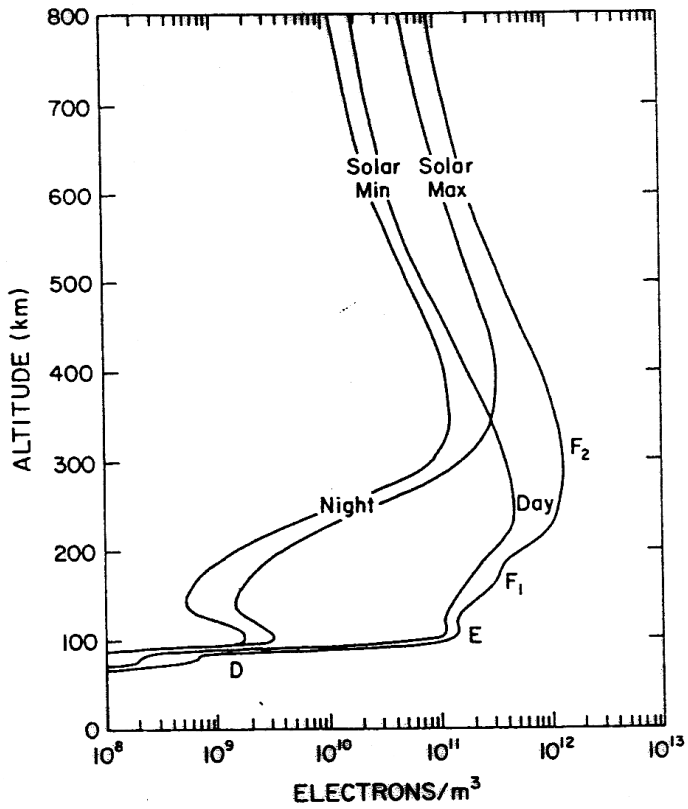

Figure 2.1: The variation of electron density with altitude for both day and night-time under conditions of high and low solar activity with the D, E and F regions labelled. From Rees (1989).

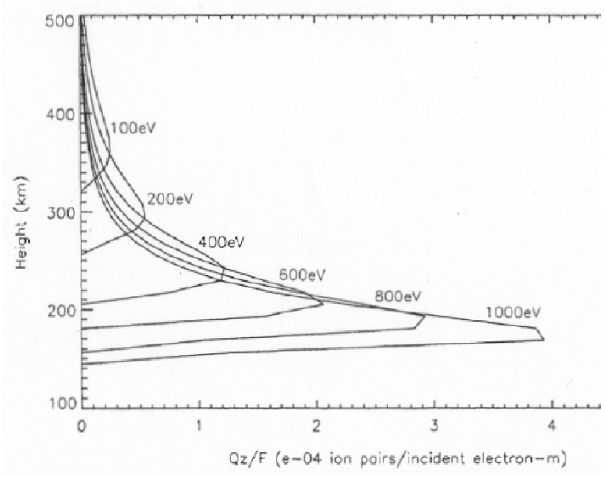

Figure 2.2: Ionisation produced by monoenergetic electron of energy 100, 200, 400, 600, 800 and 1000eV, plotted as a function of height. From Millward (1999)

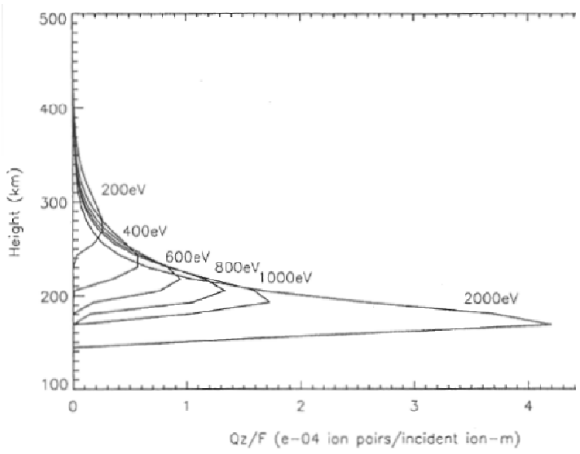

Figure 2.3: Ionisation produced by monoenergetic ions of energy 200, 400, 600, 800, 1000 and 2000eV, plotted as a function of height. From Millward (1999).

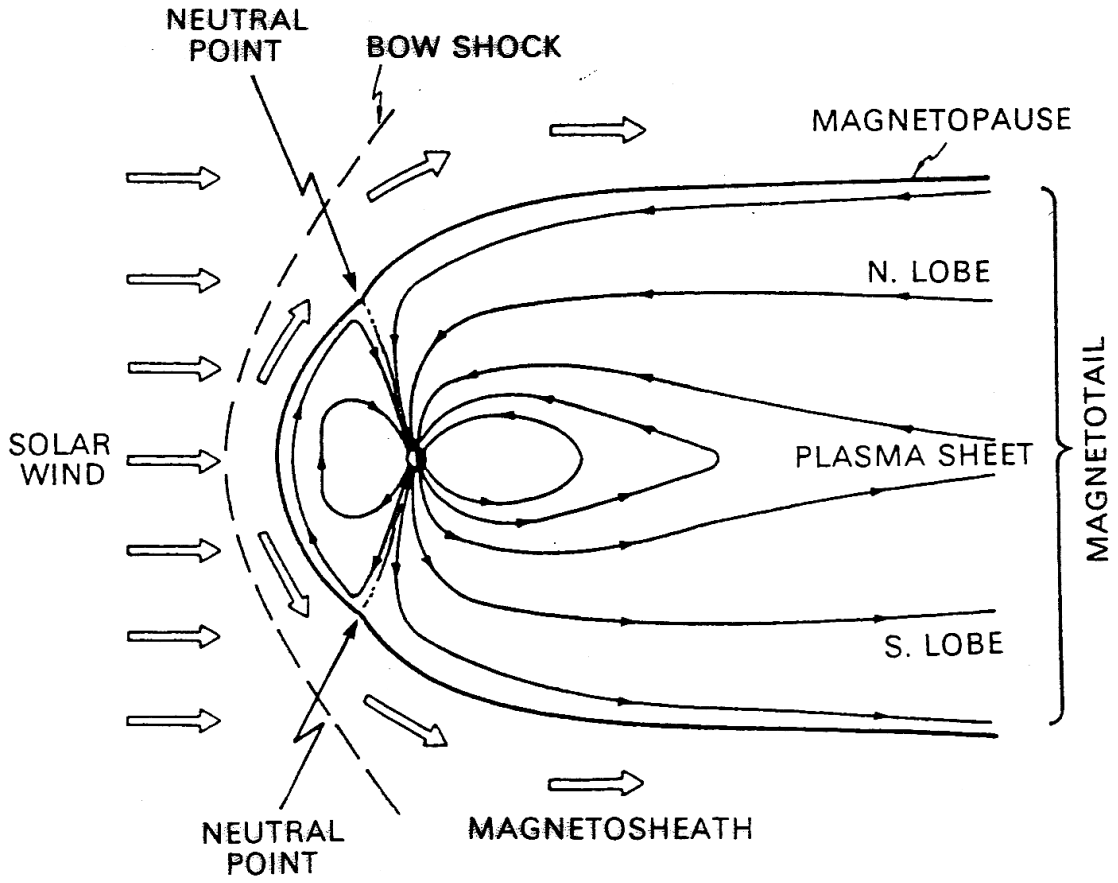

Figure 2.4: Schematic view of the magnetosphere showing the magnetopause and the bow shock. From Hargreaves (1992).

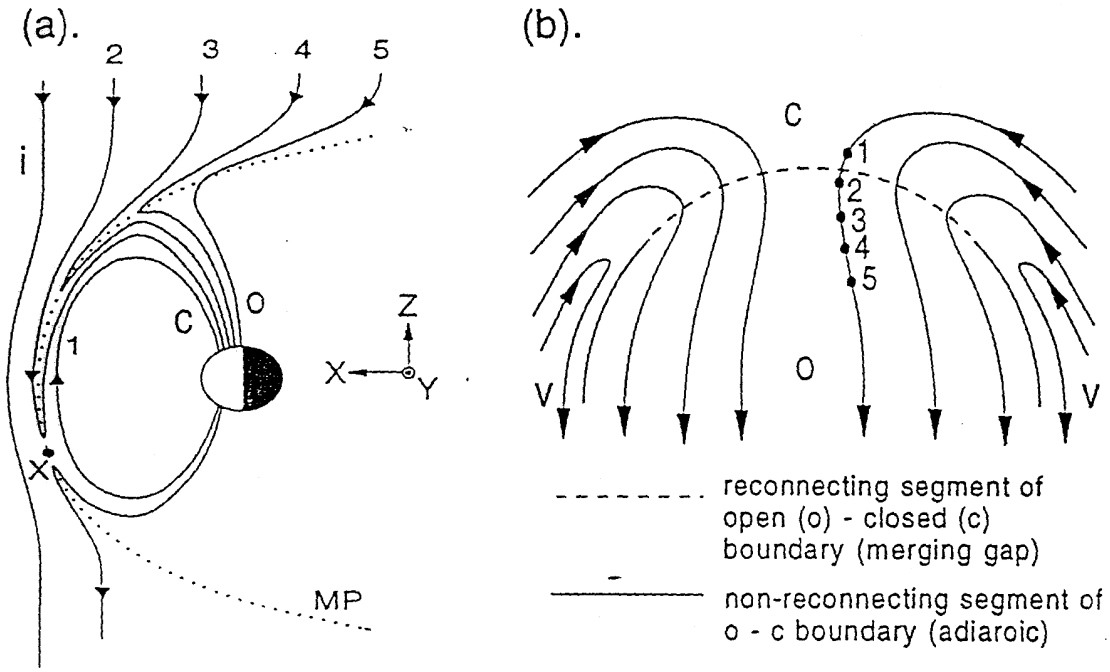

Figure 2.5: Schematic diagram of magnetopause reconnection under the condition of IMF Bz<0. Diagram (a) shows the site of reconnection marked by X which opens the magnetospheric field line marked 1 to interplanetary field lines. Field lines marked 2-5 show the development of this reconnection event over the polar cap. Diagram (b) shows the motion of field lines looking down from the northern polar cap region. The anti-sunward motion and subsequent lower-latitude return flow is shown. From Lockwood (1995).

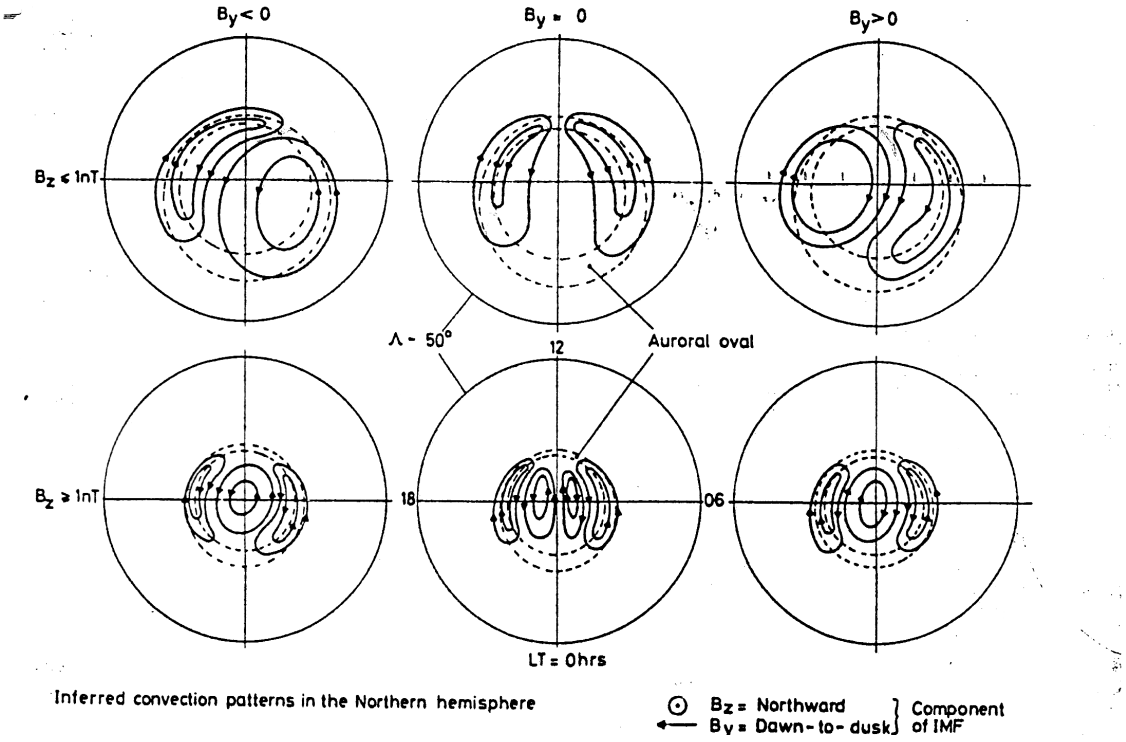

Figure 2.6: Sketch showing the nature of the high-latitude ionospheric flow in the Northern Hemisphere for different orientations of IMF. From Cowley (1991).

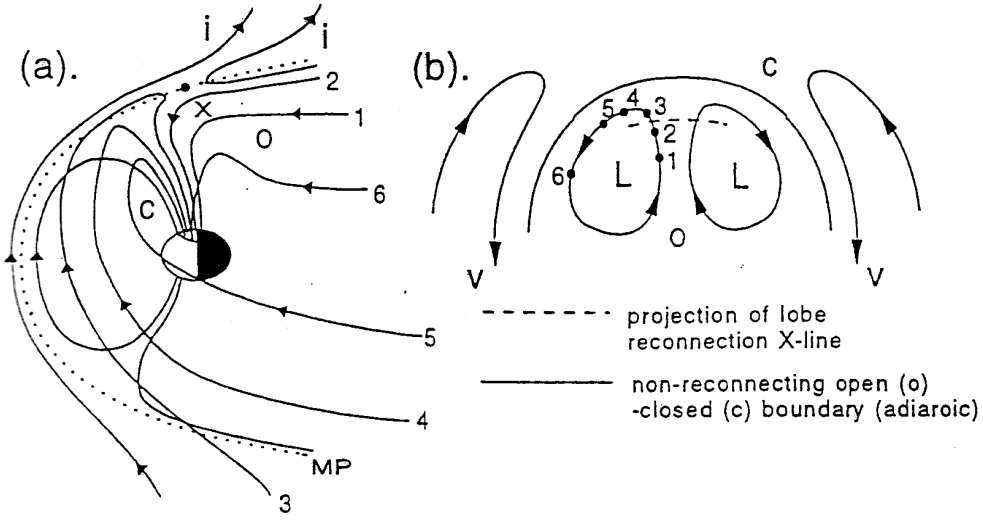

Figure 2.7: Schematic diagram of lobe reconnection under the condition of IMF Bz>0. Diagram (a) shows the site of high-latitude reconnection marked by X which occurs in the tail lobe. Field lines marked 2-5 show the development of this reconnection event over the polar cap. Diagram (b) shows the motion of field lines looking down from the northern polar cap region. In this case there are two smaller cells sweeping plasma in the sunward direction with the viscous-driven cells (V) shown at the periphery of the polar cap. From Lockwood (1995).

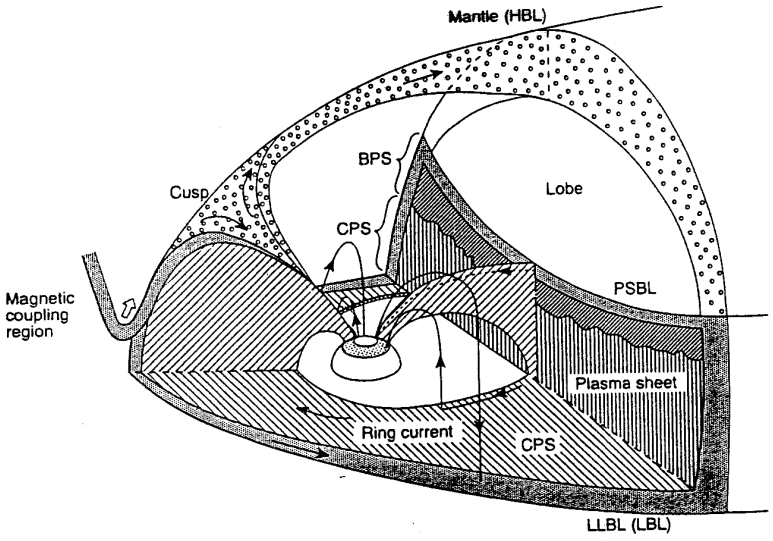

Figure 2.8: Schematic diagram of the regions of the magnetosphere based on a categorisation of plasma characteristics, from Siscoe (1991).

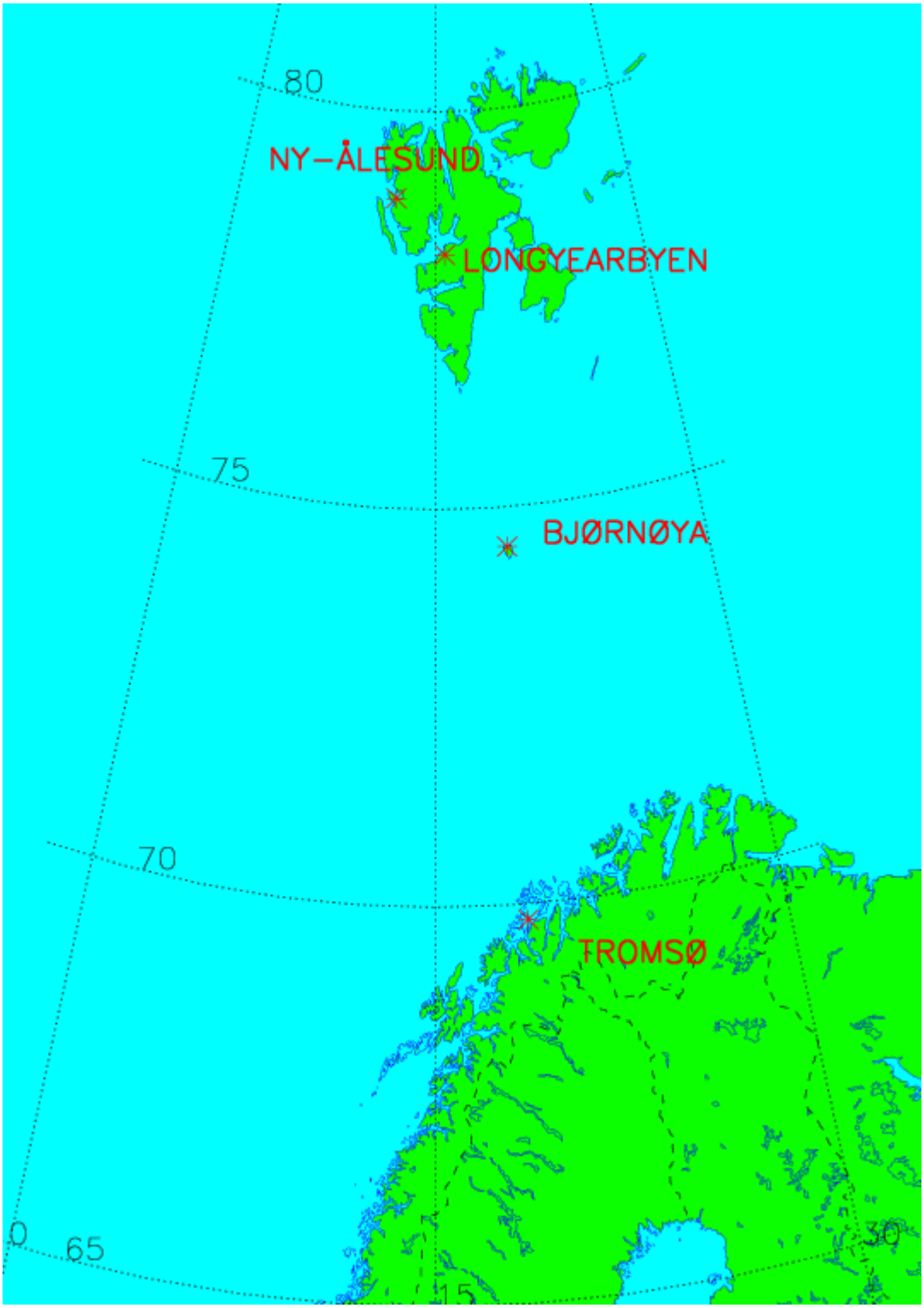

Figure 3.1: Map showing the location of the radio receivers of the Aberystwyth University tomography chain in Scandinavia.

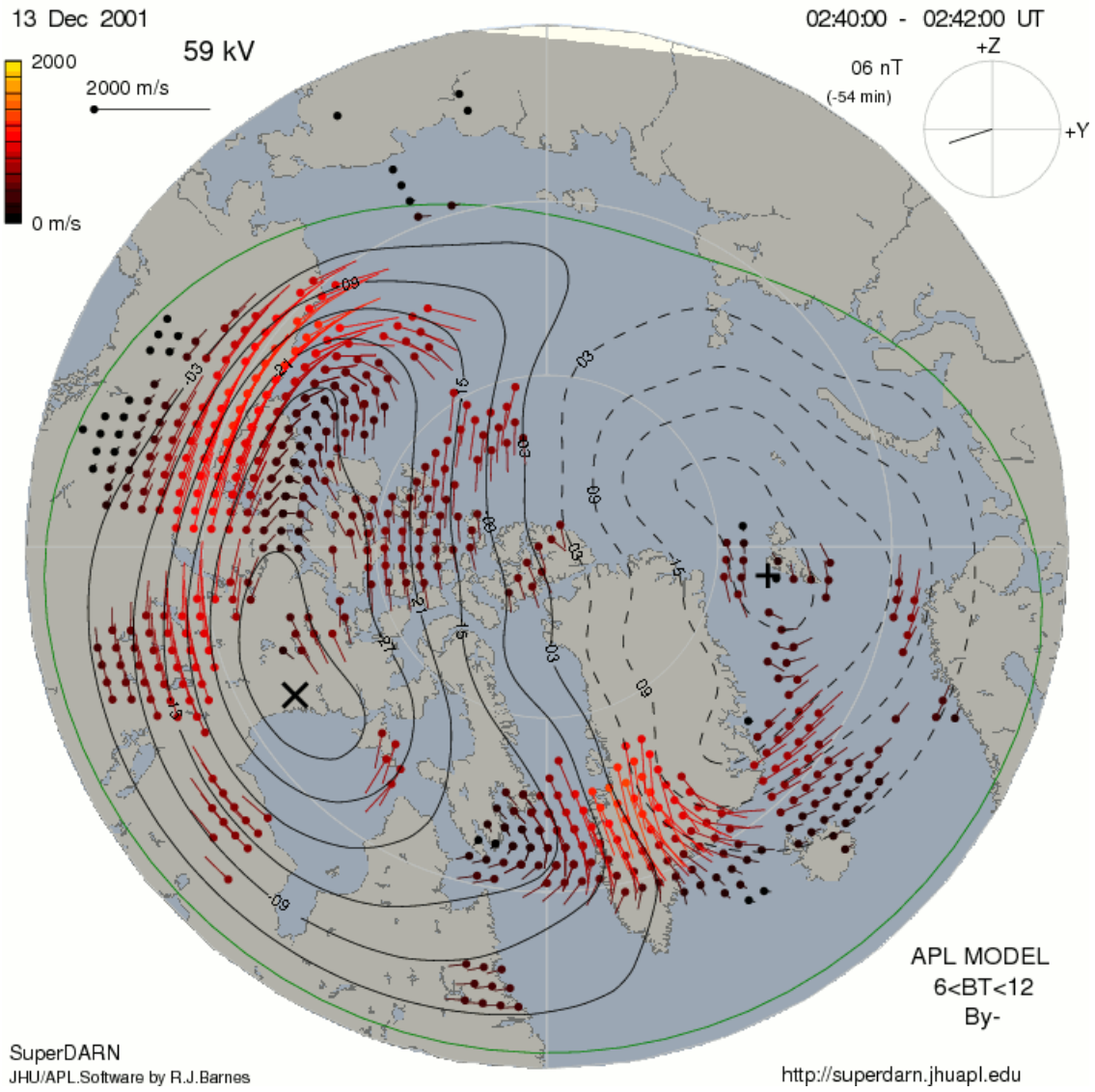

Figure 3.2: Contours of the SuperDARN electric potential pattern for 0240UT on 13 December 2001. The short lines indicate the ionospheric drift velocities measured by the radars with their lengths and colours representing the drift magnitude and their orientations indicating the direction of flow.

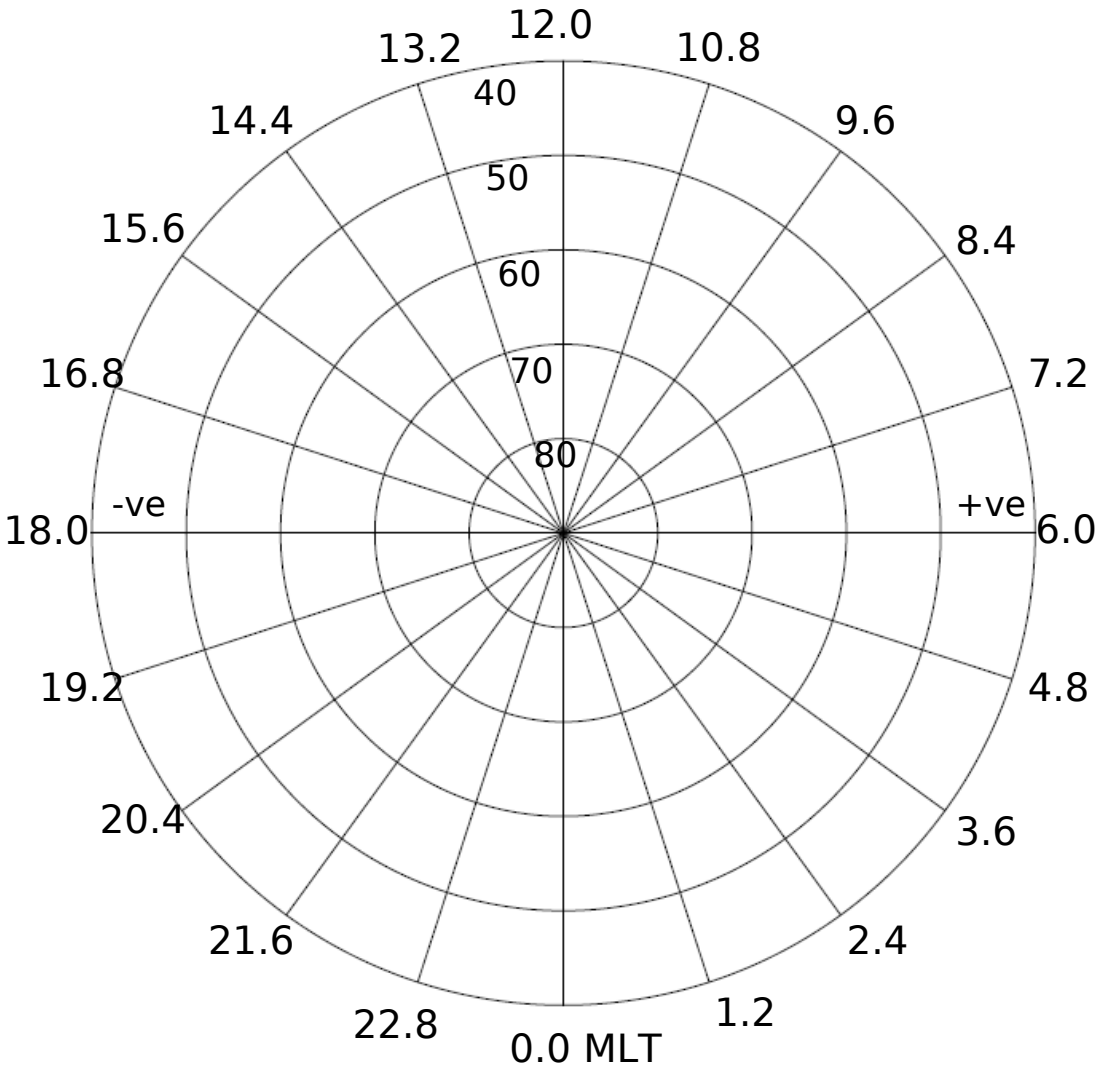

Figure 5.1: Diagram showing the polar grid in geomagnetic latitude and MLT used for the CTIP electric potential patterns. See text for details.

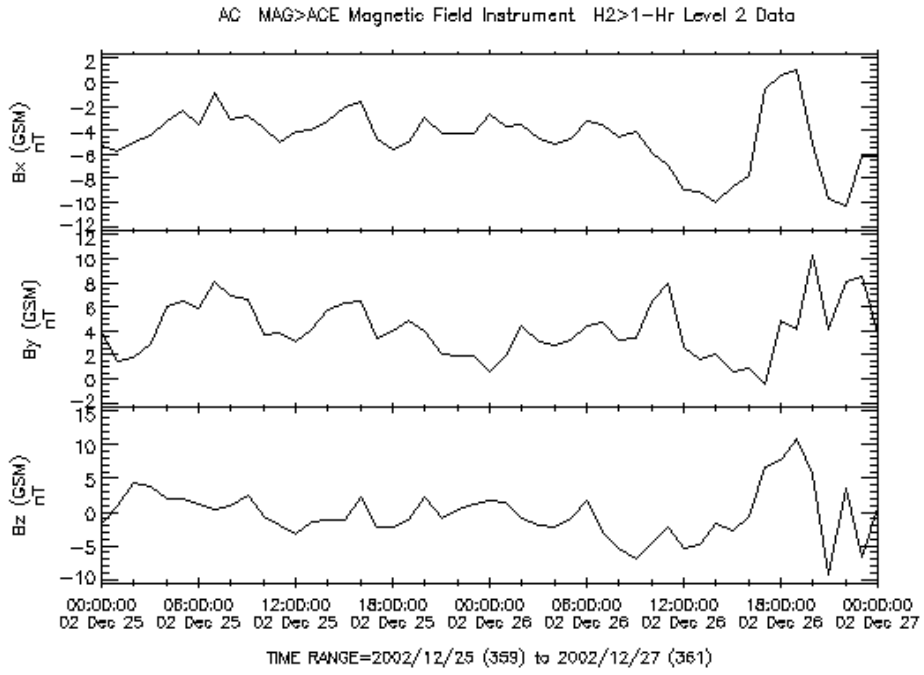

Figure 5.2: ACE data showing the IMF B components for 25-27 December 2002. IMF Bz is predominantly stable and negative during this period. *Data courtesy of N. Ness at Bartol Research Institute and CDAWeb.*

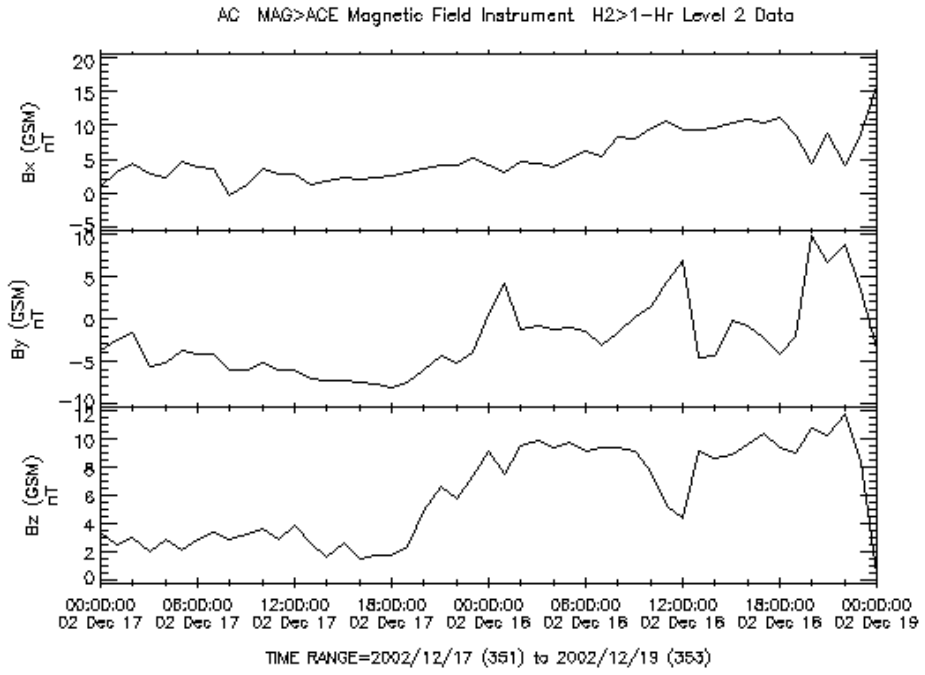

Figure 5.3: ACE data showing the IMF B components for 17-19 December 2002. IMF Bz is stable and positive during this period. *Data courtesy of N. Ness at Bartol Research Institute and CDAWeb.*

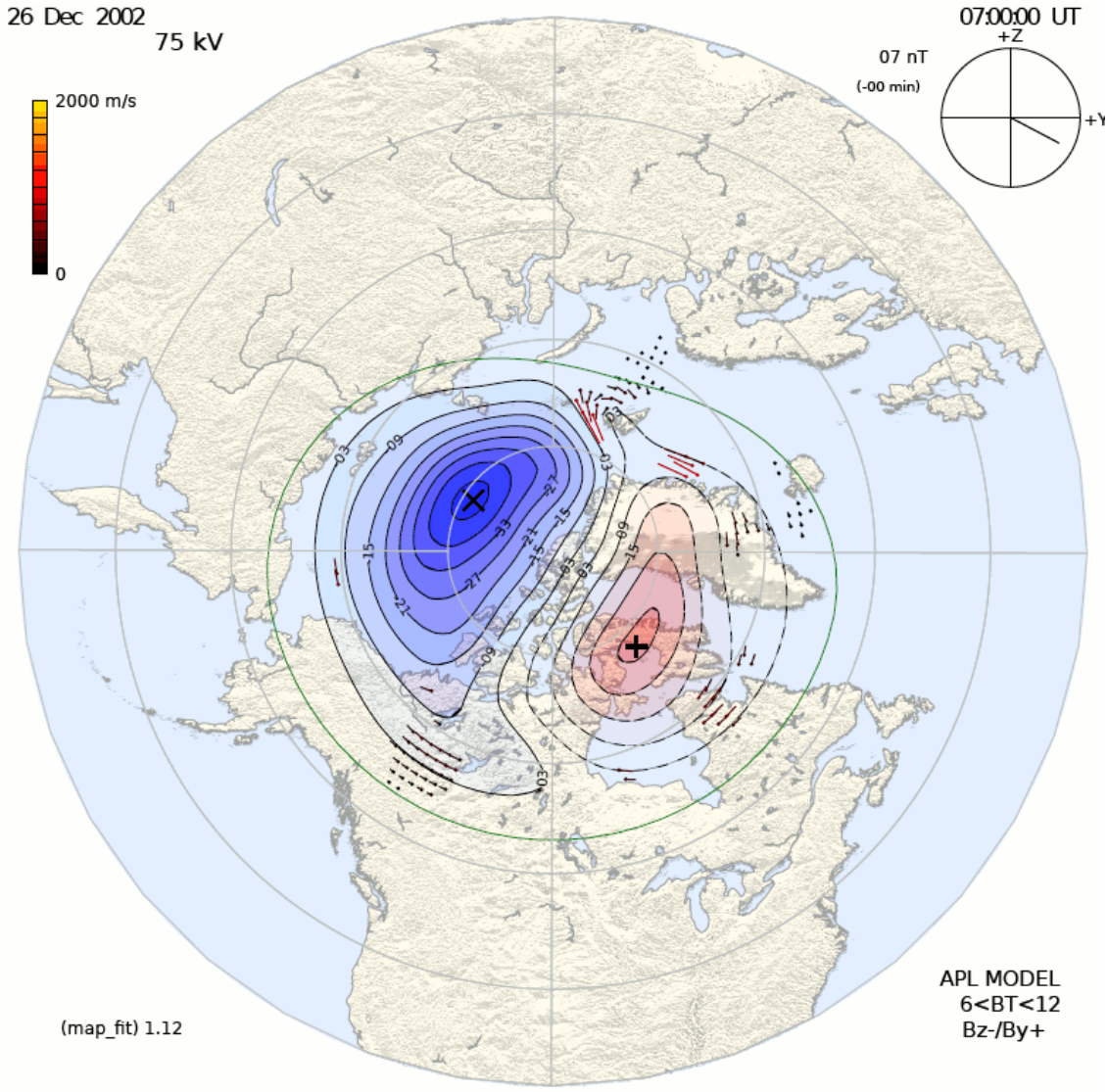

Figure 5.4: IMF Bz negative electric potential pattern from the SuperDARN website. This is the 0700UT electric potential pattern. The latitudinal scale is in 10°MLAT steps.

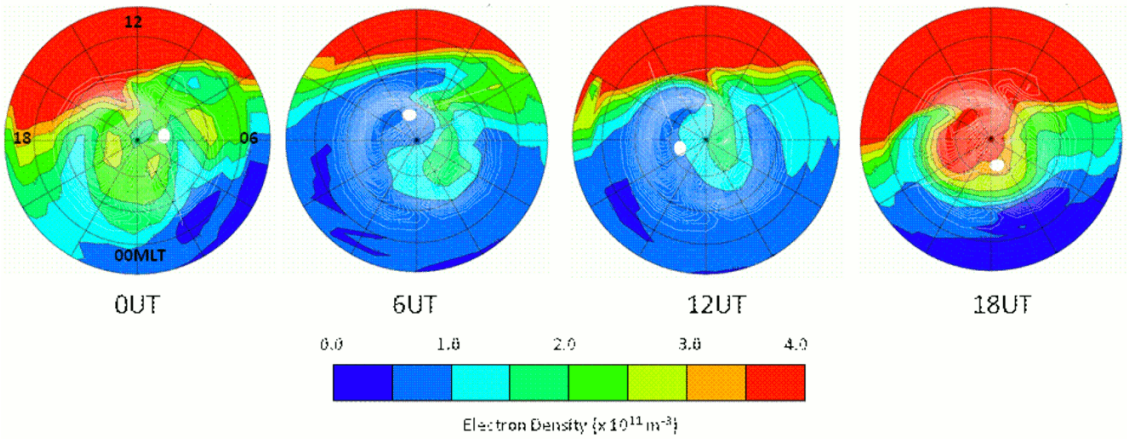

Figure 5.6: IMF Bz negative CTIP output for selected UTs. Each UT is plotted on a magnetic grid at an altitude near the F2 region peak at 270km. Latitudes extend down to 50°N.

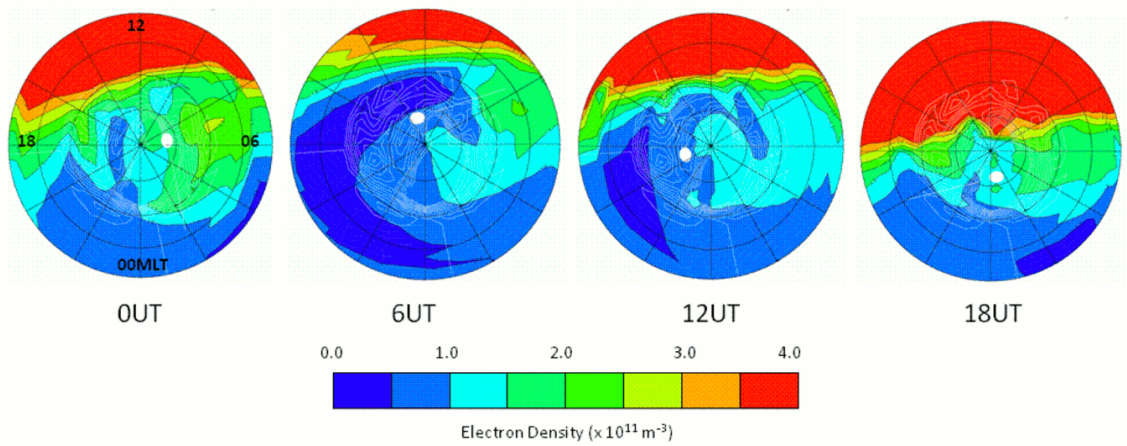

Figure 5.7: IMF Bz positive CTIP output for selected UTs. Each UT is plotted on a magnetic grid at an altitude near the F2 region peak at 270km. Latitudes extend down to 50°N.

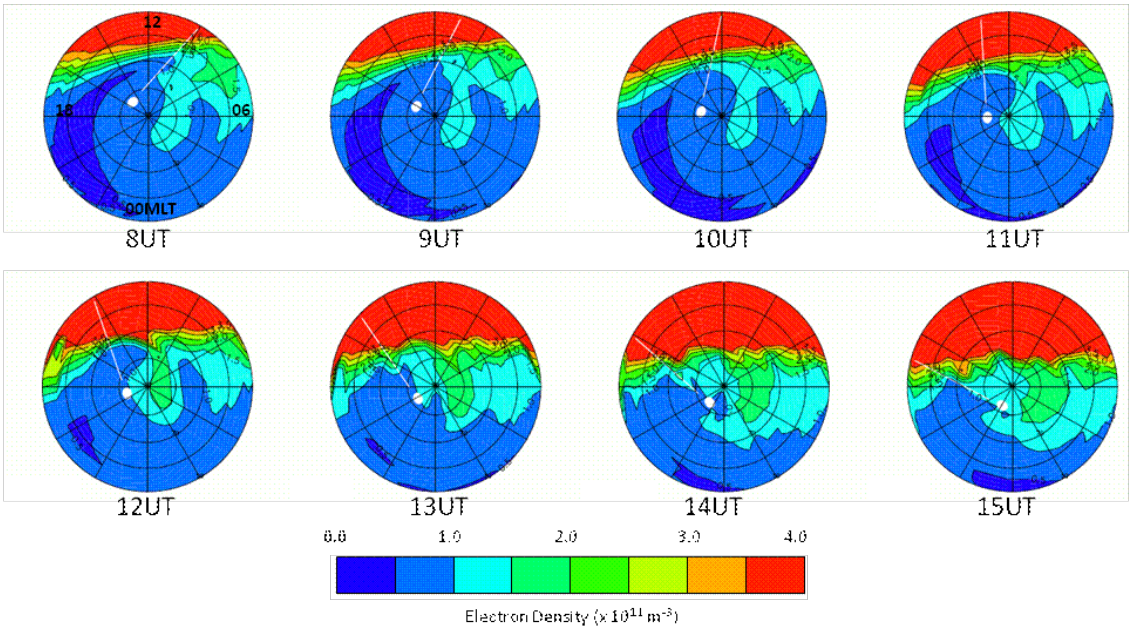

Figure 5.8: CTIP model output showing the electron density change as a result of switching the electric potential pattern from IMF Bz negative to positive.

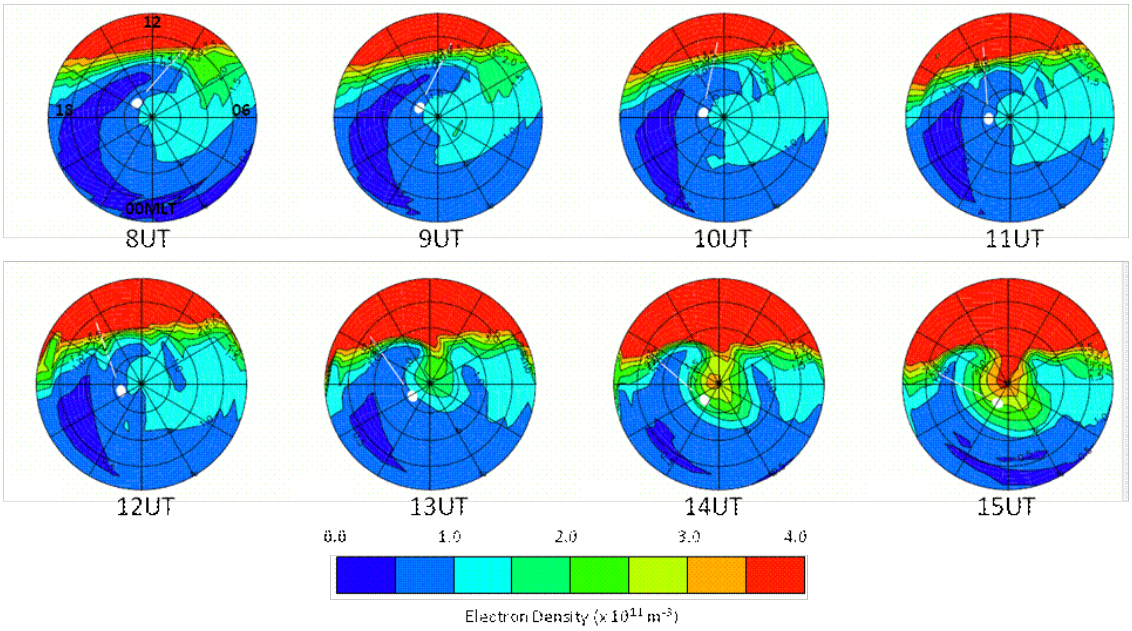

Figure 5.9: CTIP model output showing the electron density change as a result of switching the electric potential pattern from IMF Bz positive to negative.

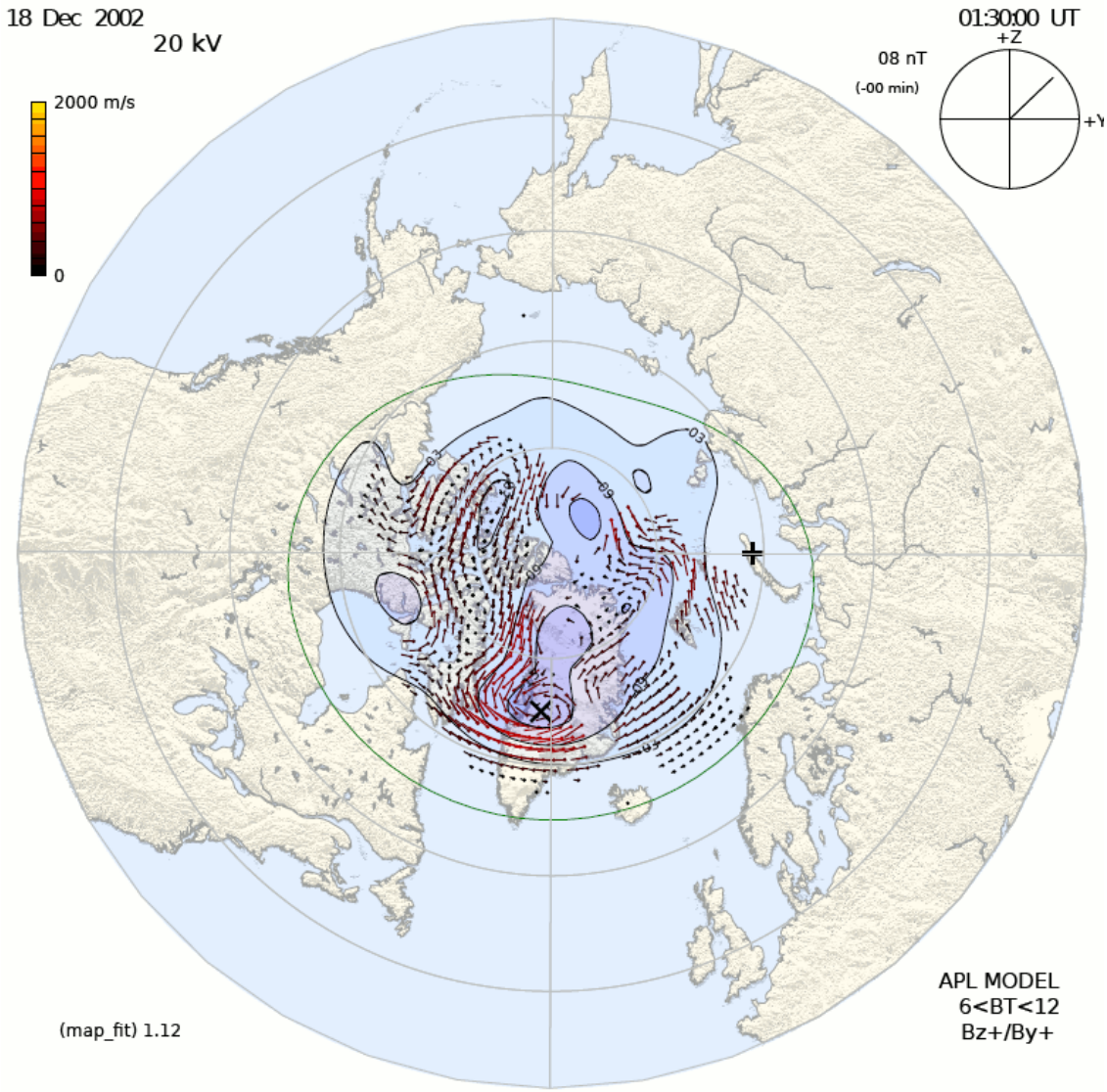

Figure 5.5: IMF Bz positive electric potential pattern from the SuperDARN website. This is the 0130UT electric potential pattern. The latitudinal scale is in 10°MLAT steps.

Figure 6.1: Map showing the locations of the radio receivers of the tomography chains in Scandinavia, UK and Greenland.

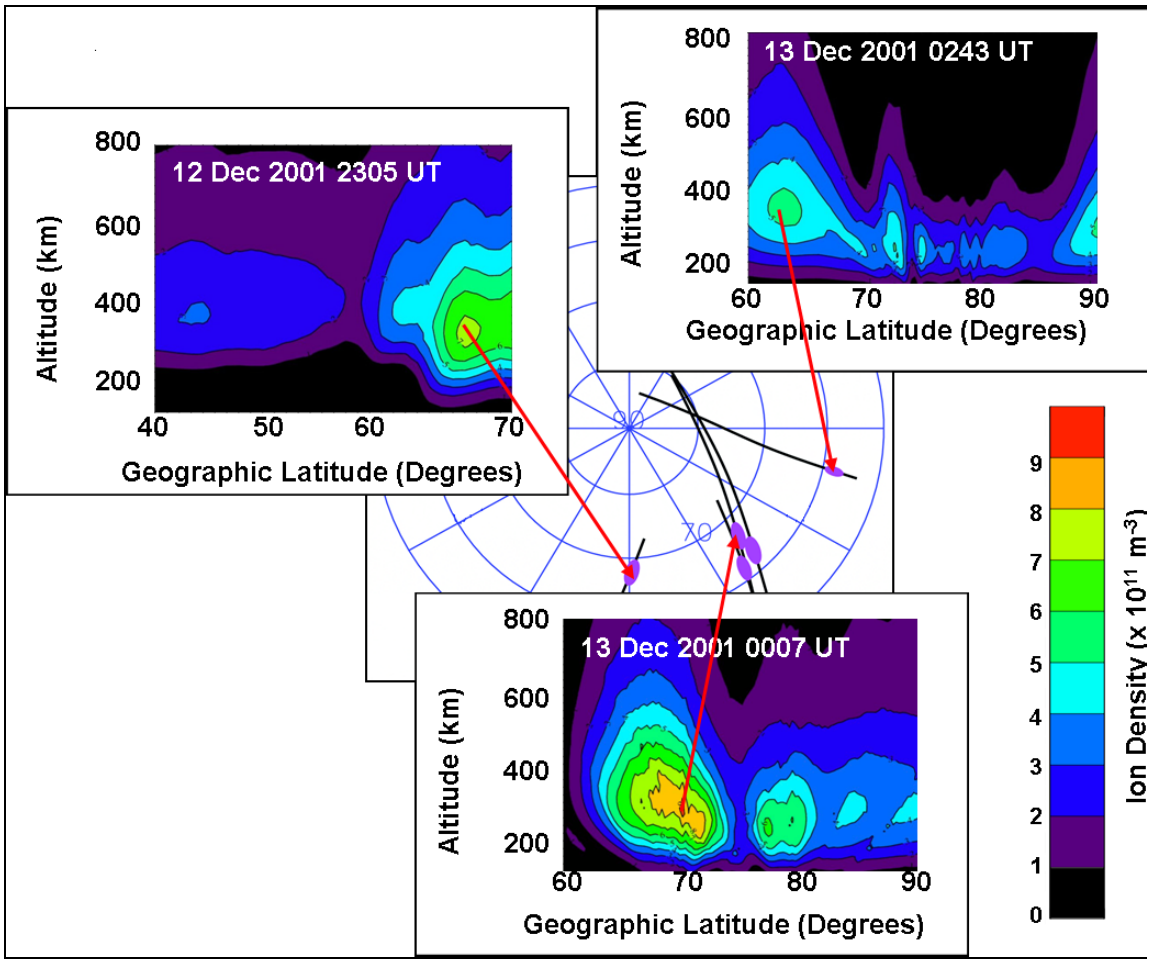

Figure 6.2: Three sample tomography reconstructions for 2305UT (UK), 0007UT (Scandinavia) and 0243UT (Scandinavia) on the evening of 12-13 December 2001. The locations of the maximum electron density of the prominent enhancement in the three reconstructions, and two other reconstructions (not shown), are indicated in the centre panel by the purple dots on a MLAT versus MLT polar plot. Magnetic local midnight is at the bottom of the circles, with 06UT on the right-hand-side.

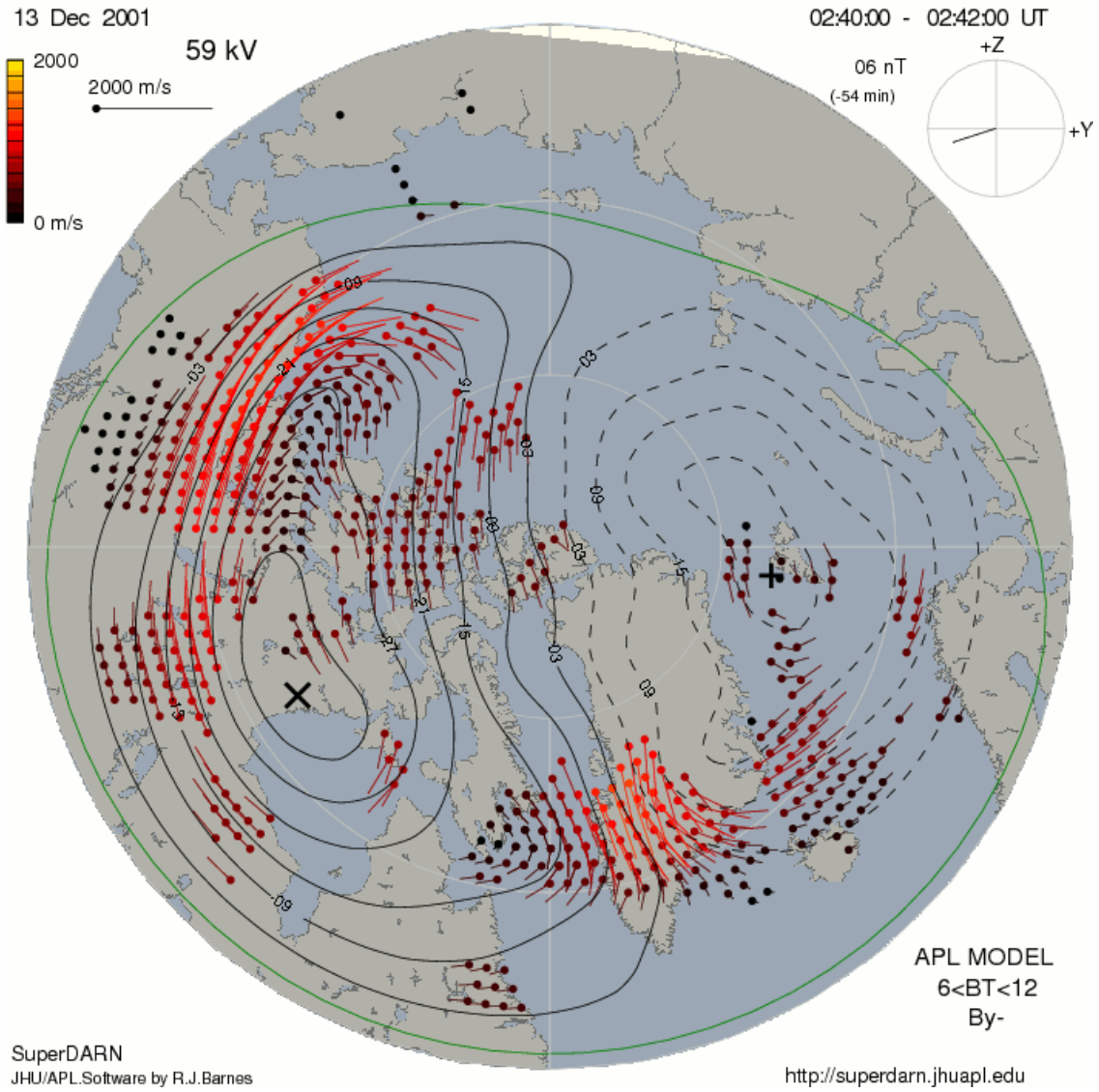

Figure 6.3: Contours of the SuperDARN electric potential pattern for 0240UT on 13 December 2001. The short lines indicate the ionospheric drift velocities measured by the radars with their lengths and colours representing the drift magnitude and their orientations indicating the direction of flow.

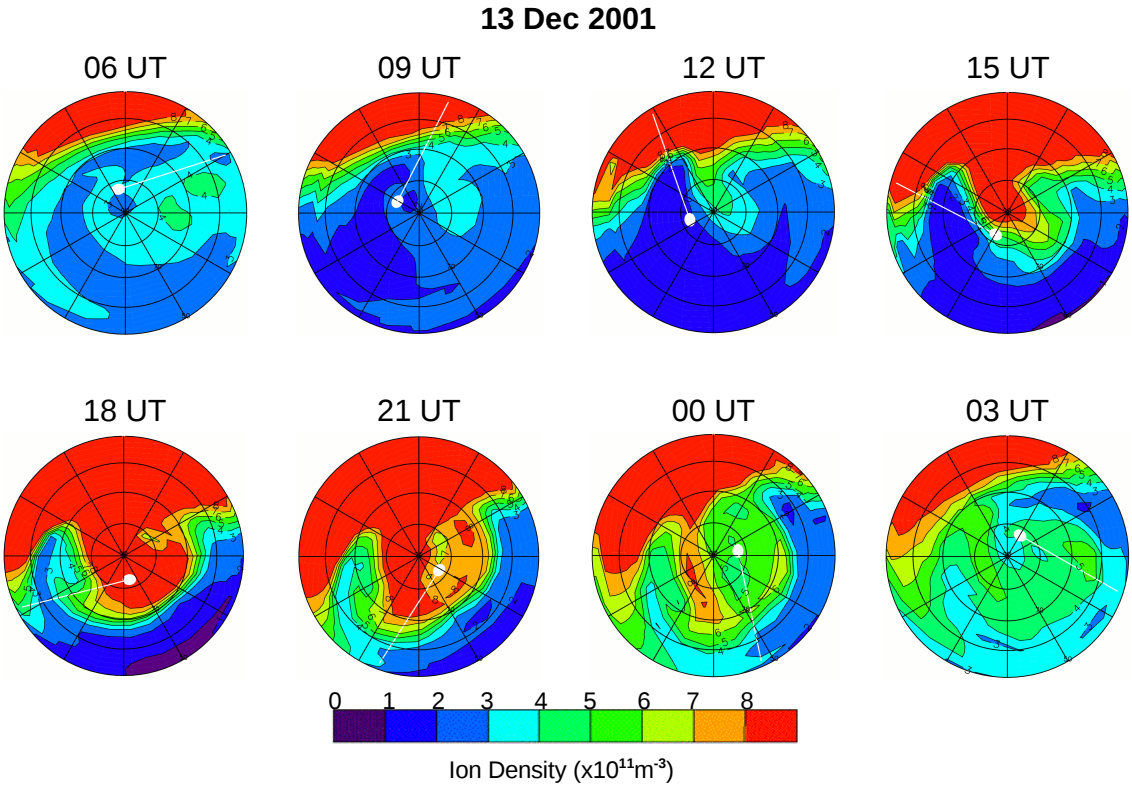

Figure 6.4: Ion densities modelled by CTIP for 13 December 2001. The panels are at 3-hour intervals of UT, with each panel showing the ion density distribution at an altitude of 320km, near the F-region ionisation peak, as a function of MLAT and MLT. Magnetic latitude extends from 50°MLAT at the outer circumference to the magnetic pole in the centre of the circle. Magnetic noon is at the top of each panel with midnight at the bottom, 18MLT is on the left-hand side and 06MLT on the right-hand side. The small white region near the centre encompasses the geographic pole, and the white line shows the 18°E meridian near the longitude of the Scandinavian tomography chain.

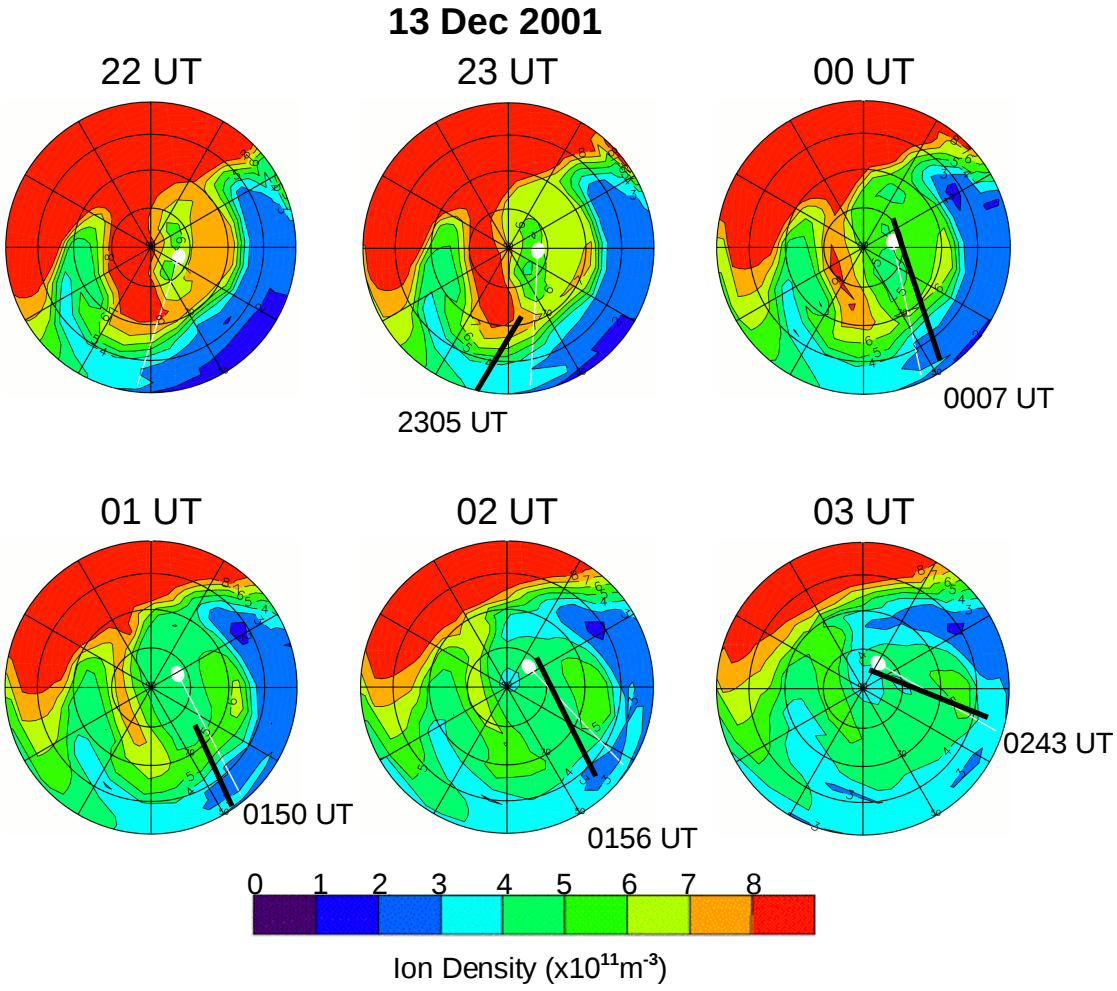

Figure 6.5: Ion densities modelled by CTIP from 22UT to 03UT for 13 December 2001. The panels are at hourly intervals of UT, with each panel showing the ion density distribution at an altitude of 320km, near the F-region ionisation peak, as a function of MLAT and MLT. The format of the panels is the same as for Figure 6.4, with the white line showing the 18°E meridian near the longitude of the Scandinavian tomography chain. The black lines indicate the 300km trajectory intersections of the satellite passes of the reconstructions.

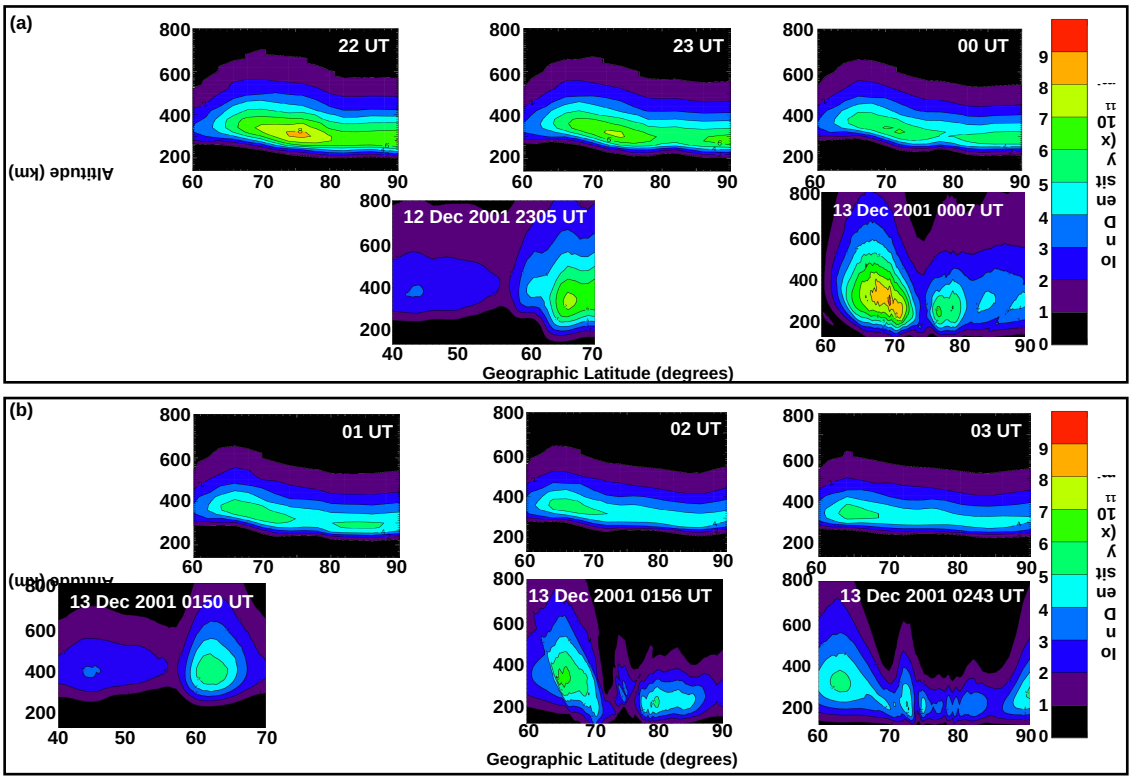

Figure 6.6: Comparison of the CTIP modelled ion density (top row of each panel) and radio tomography observations (bottom row of each panel) on a latitude-versus-altitude grid. The modelled densities are at the 18°E meridian at hourly intervals between 22UT and 00UT in panel (a) and between 01UT and 03UT in panel (b). These are paired with the corresponding tomography images in the bottom row of each panel. The reconstructions from the UK tomography chain are displaced to the left of those for the Scandinavian chain for consistency in the latitudinal placement of the observed ionisation enhancement.

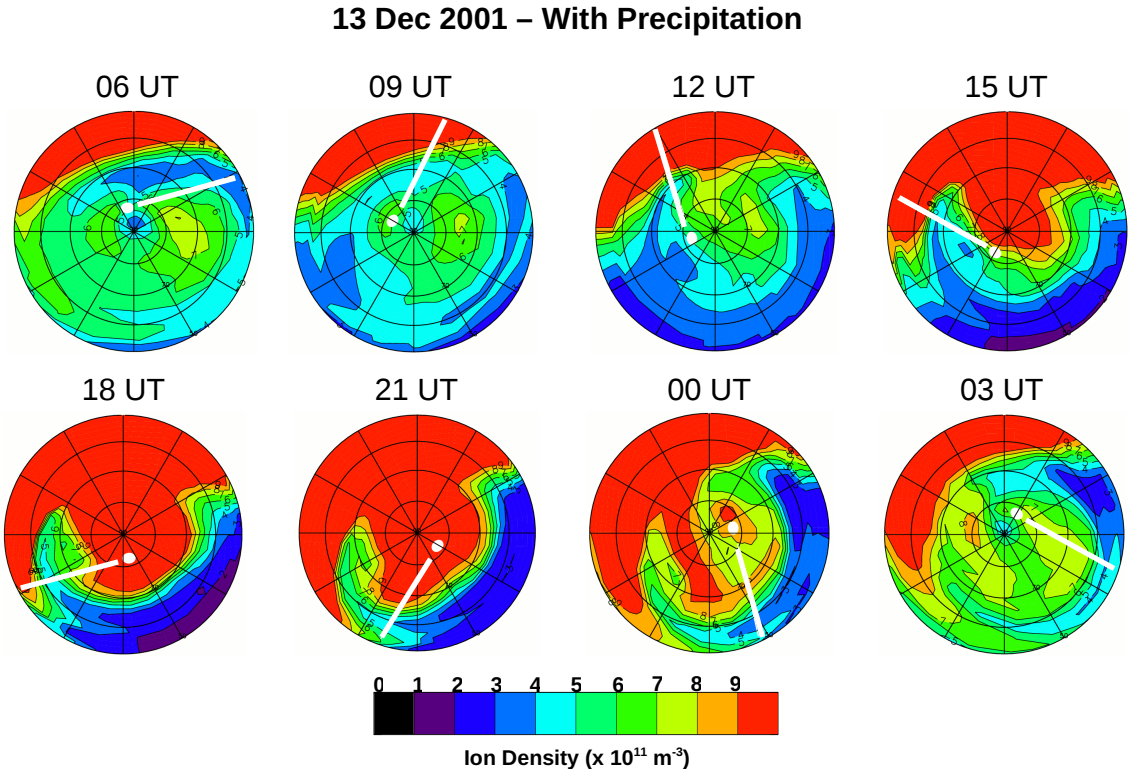

Figure 6.7: Ion densities modelled by CTIP for 13 December 2001, but with precipitation input included in the model. The panels are at 3-hour intervals of UT, with each panel showing the ion density distribution at an altitude of 320km, near the nightside F-region ionisation peak, as a function of MLAT and MLT. The format of the panels is as for Figure 6.4, with the white line showing the 18°E meridian near the longitude of the Scandinavian tomography chain.

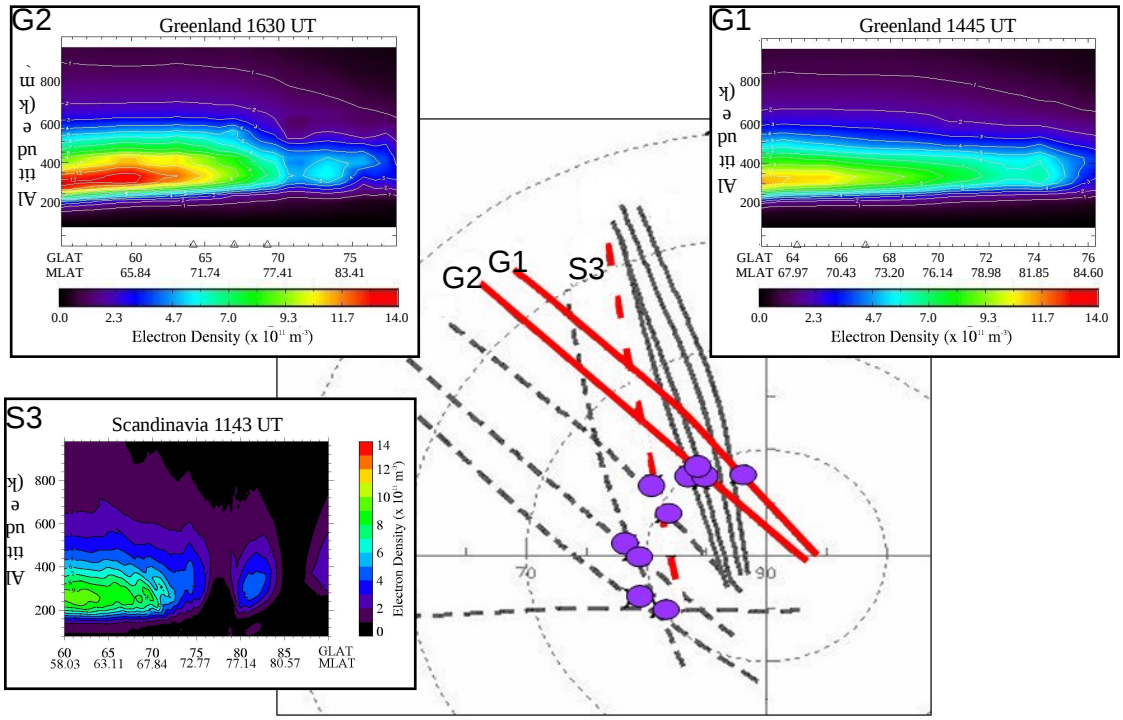

Figure 6.8: Three sample tomography reconstructions for 1445UT (Greenland), 1630UT (Greenland) and 1143UT (Scandinavia) on 26 November 2001. The trajectories of the corresponding three satellite passes are shown in red in the centre panel on a MLAT versus MLT polar plot. The locations of the electron density feature detaching from the main photoionisation for these reconstructions and another seven reconstructions (not shown) are indicated by the purple dots in the centre panel.

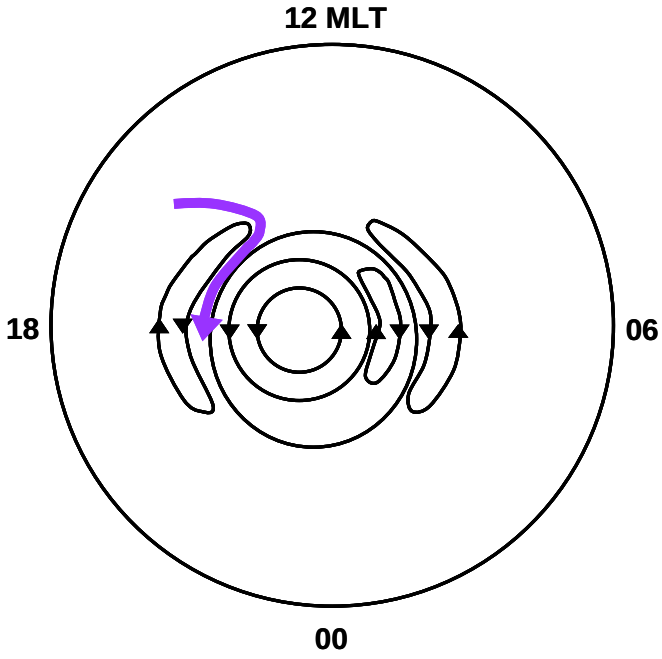

Figure 6.9: Schematic showing the TOI being drawn around the periphery of the polar cap under conditions of IMF Bz positive. The purple curve indicates the TOI, and the streamlines are representative of the plasma convective flow under the pertinent IMF conditions.

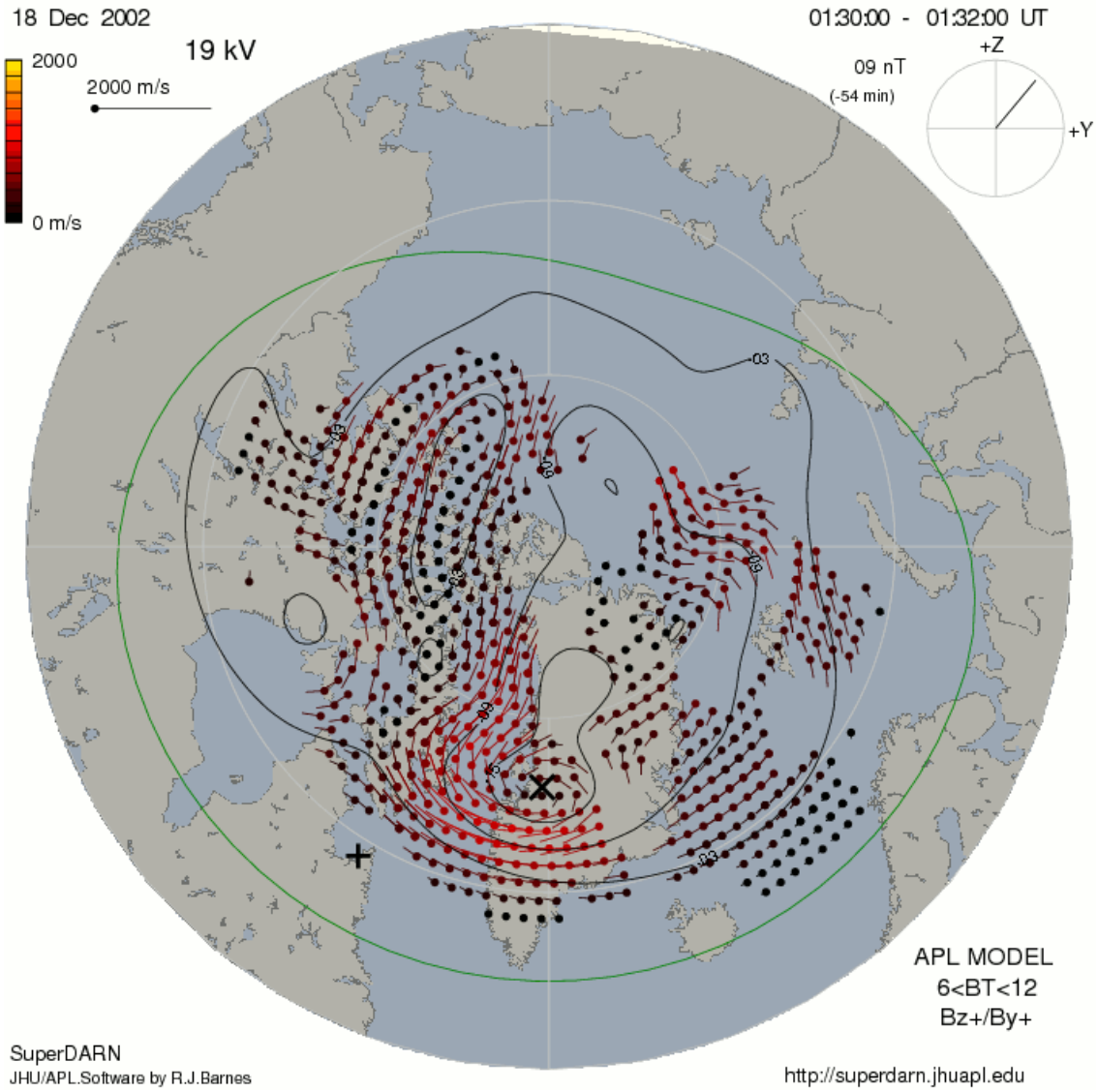

Figure 6.10: Contours of the SuperDARN electric potential pattern for 0130UT on 18 December 2002, showing sunward flow across the polar cap. The short lines indicate the magnitude and direction of the ionospheric drift velocities measured by the radars.

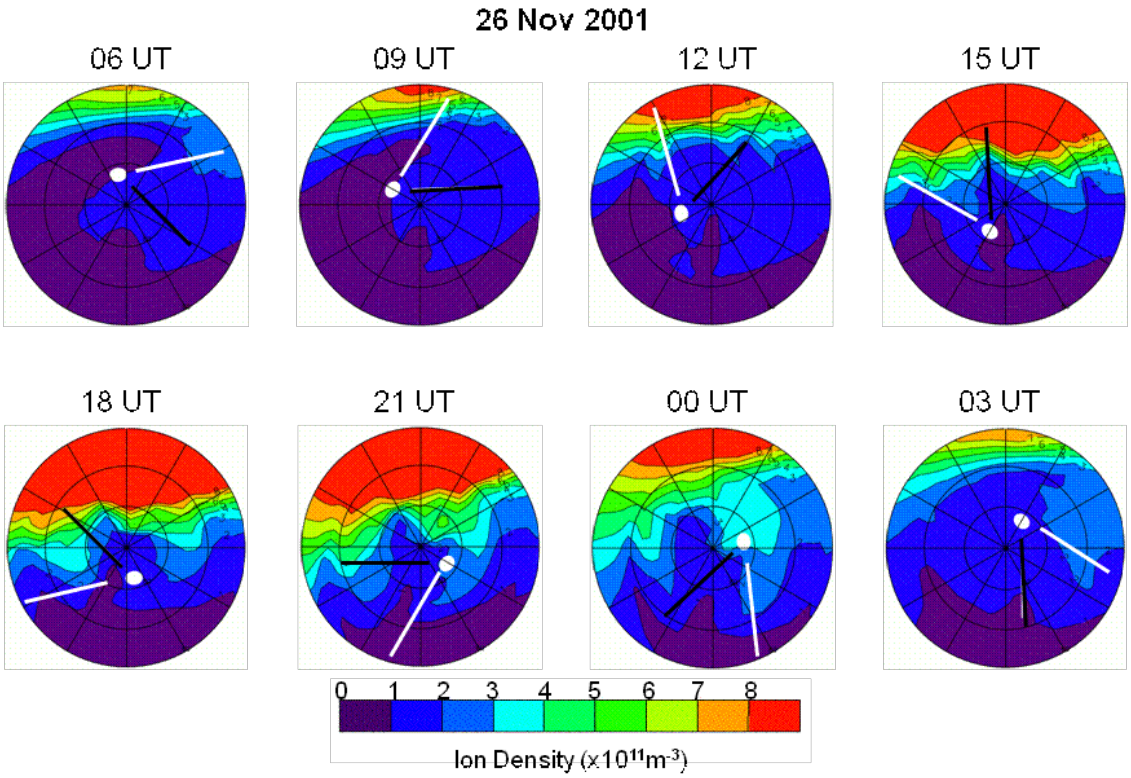

Figure 6.11: Ion densities modelled by CTIP for 26 November 2001. The panels are at 3-hour intervals of UT, with each panel showing the ion density distribution at an altitude of 270km, near the F-region ionisation peak, as a function of MLAT and MLT. The format of the panels is as for Figure 6.4, with the white line showing the 18ºE meridian near the longitude of the Scandinavian tomography chain and the black line indicating the 54ºW meridian near the longitude of the Greenland chain.

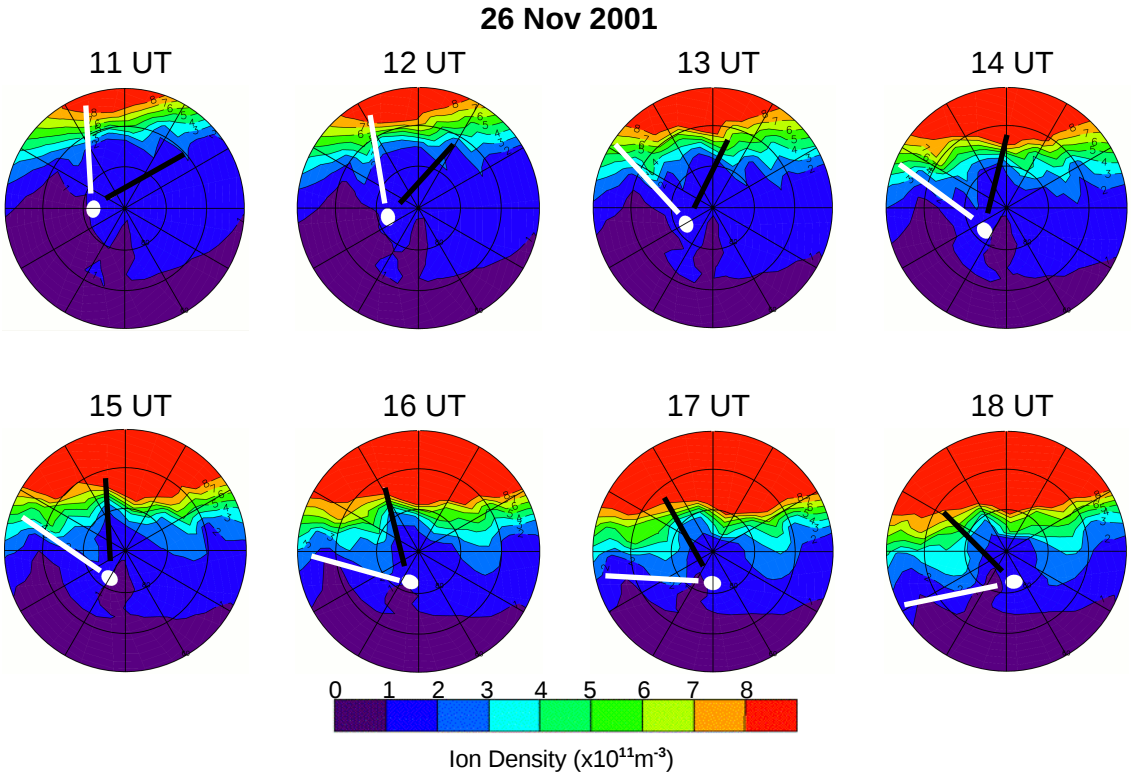

Figure 6.12: Ion densities modelled by CTIP for 26 November 2001. The panels are at 3-hour intervals of UT, with each panel showing the ion density distribution at an altitude of 270km, near the F-region ionisation peak, as a function of MLAT and MLT. The format of the panels is as for Figure 6.4, with the white line showing the 18ºE meridian near the longitude of the Scandinavian tomography chain and the black line indicating the 54ºW meridian near the longitude of the Greenland chain.

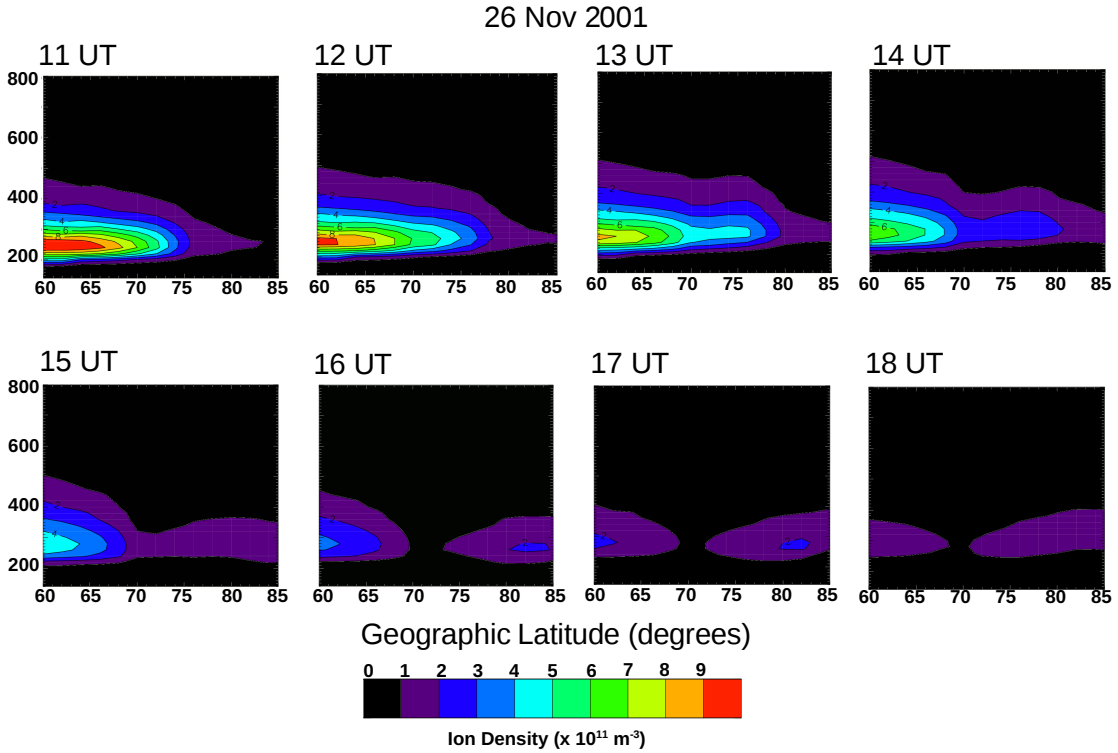

Figure 6.13: CTIP modelled ion densities at hourly intervals between 11UT and 18UT for latitude-versus-altitude planes at the 18°E meridian.

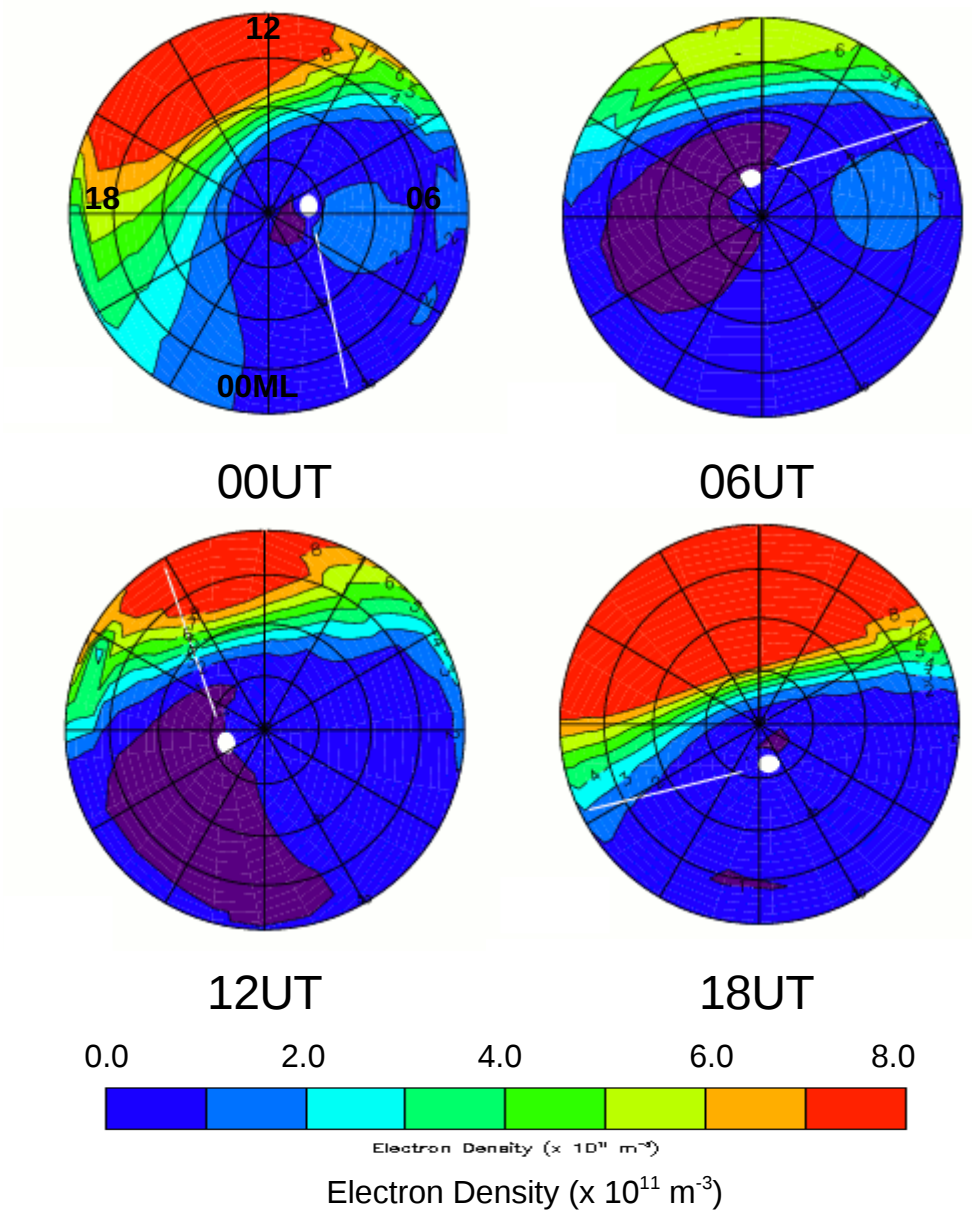

Figure 7.1: CTIP model output for 13 December 2001 (day 347) showing only the electron density for the solar output for 0UT, 6UT, 12UT and 18UT. The F10.7 value is set at 230 and the polar plots are plotted in MLT at a height of 320km. The latitudinal scale extends from 90°MLAT to 50°MLAT in 10° steps.

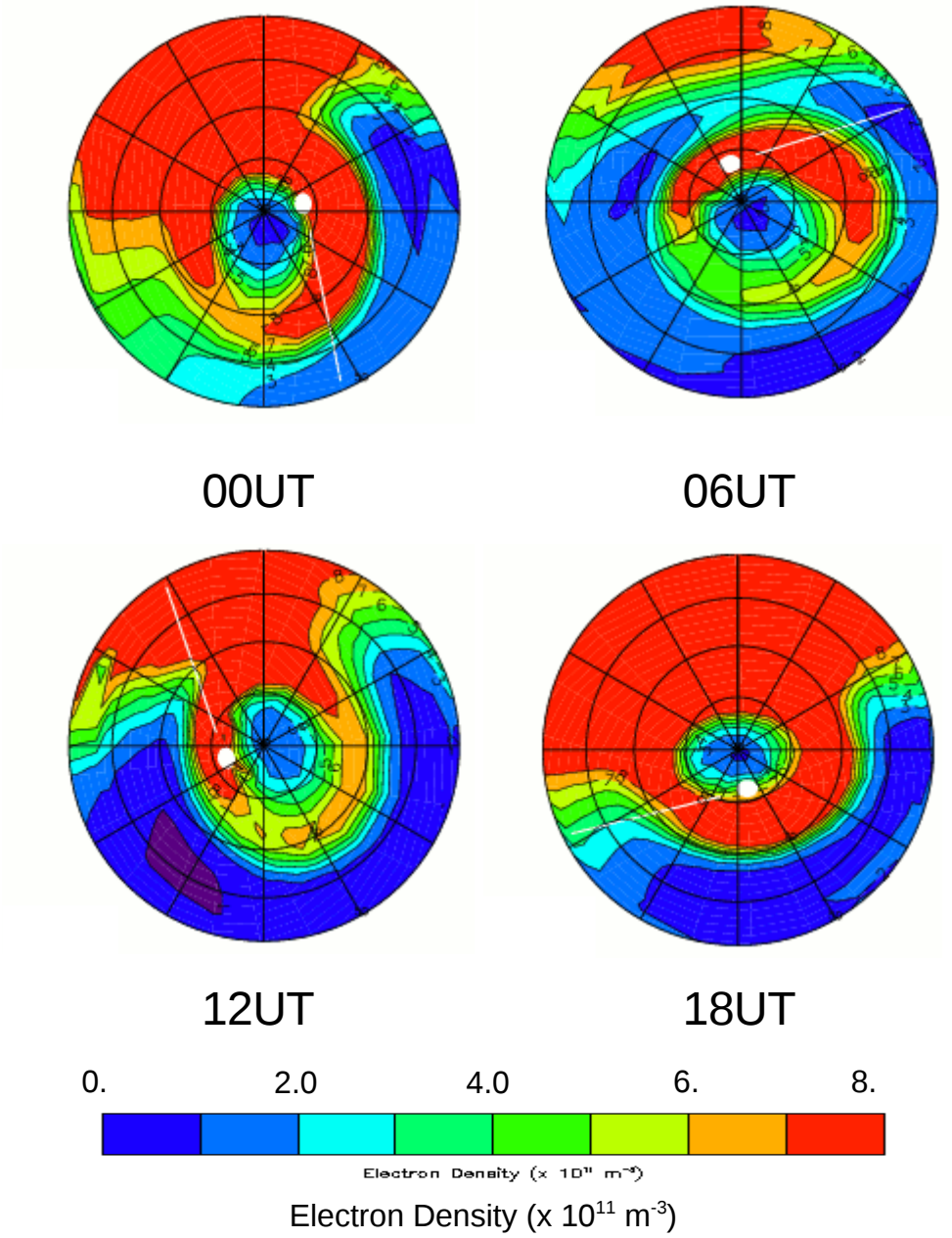

Figure 7.2: CTIP model output for 13 December 2001 (day 347) showing the electron density for the solar output with DMSP precipitation for 0UT, 6UT, 12UT and 18UT. The F10.7 value is set at 230 and the polar plots are plotted in MLT at a height of 320km. The latitudinal scale extends from 90°MLAT to 50°MLAT in 10° steps.

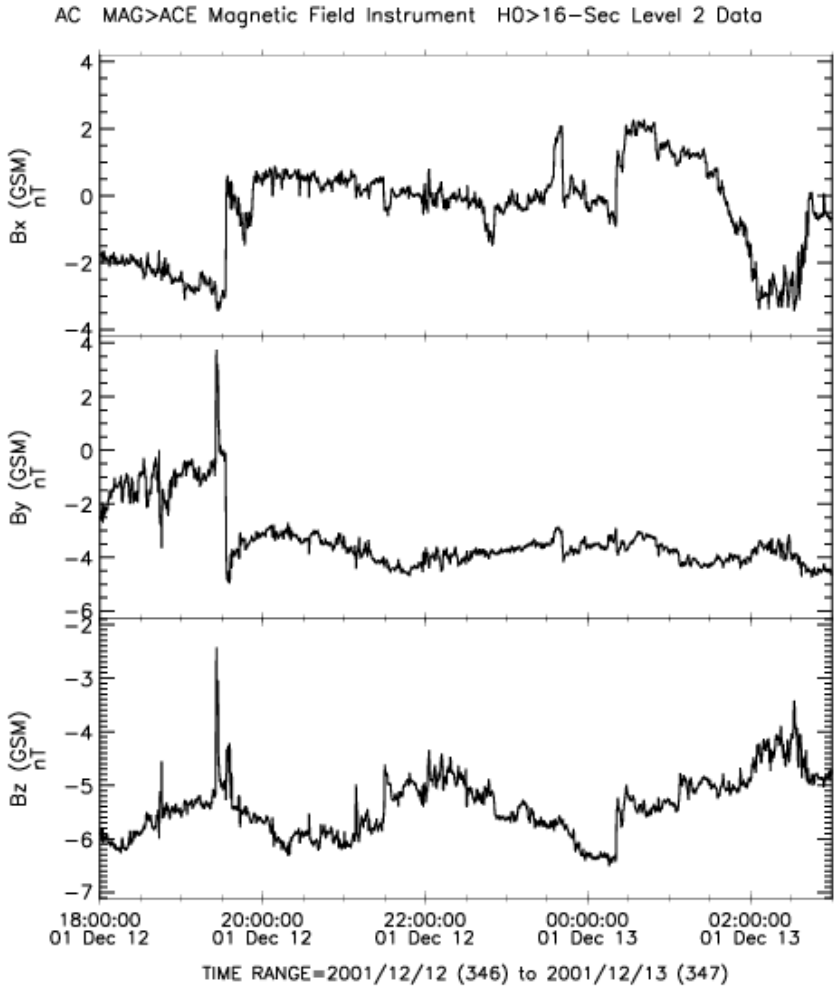

Figure 7.3: ACE plot showing the IMF Bz component to be negative and stable from 18UT on 12 December 2001. *Data courtesy of N. Ness at Bartol Research Institute and CDAWeb.*

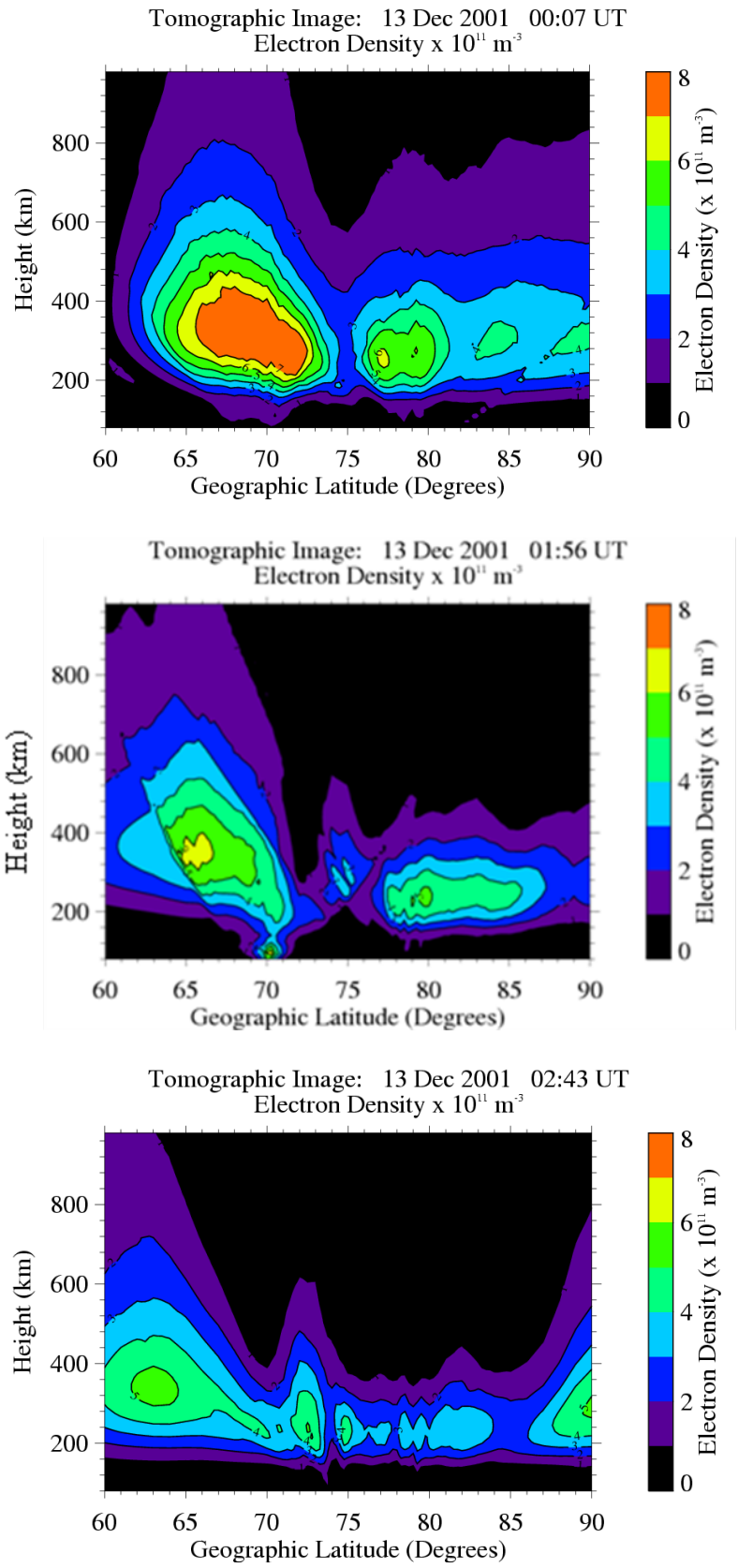

Figure 7.4: IMF Bz negative tomography plots for 000UT, 0156UT and 0243UT on 13 December 2001.

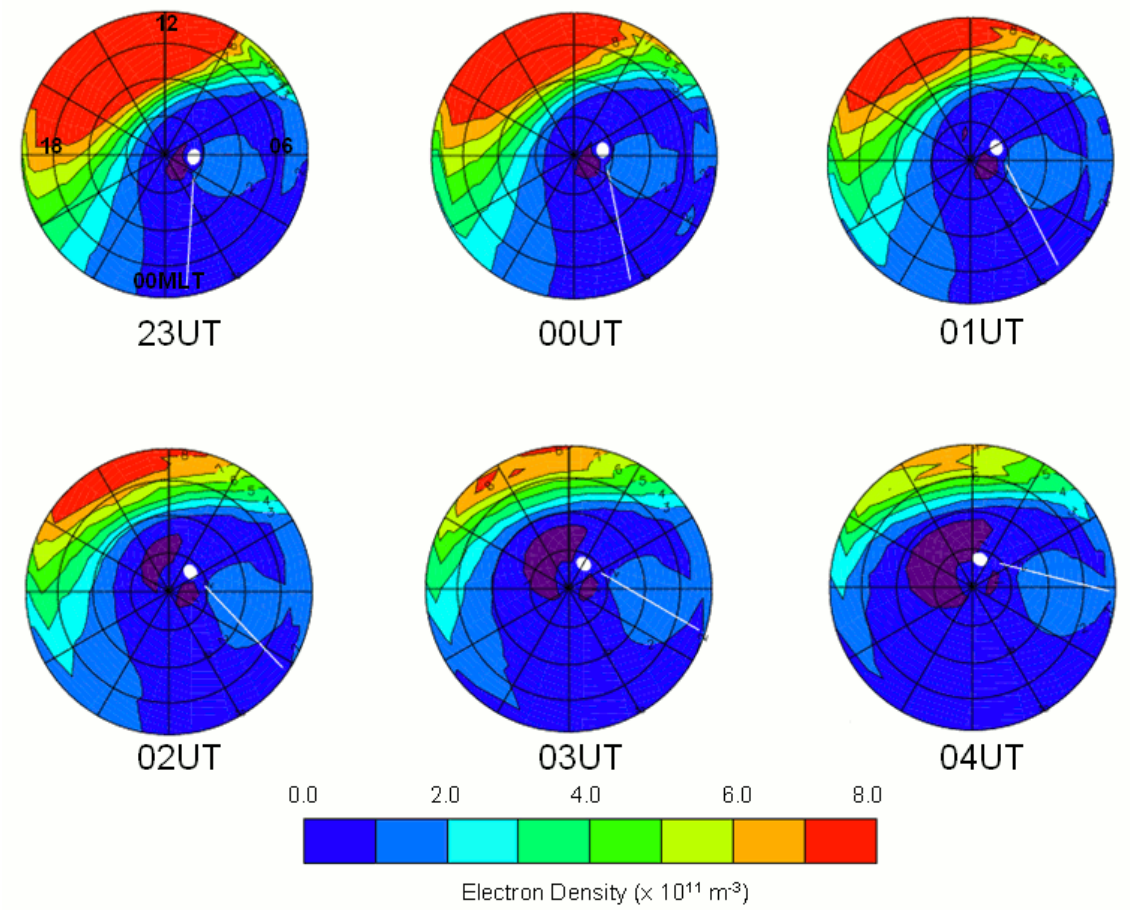

Figure 7.5: CTIP model output for 13 December 2001 showing the electron density due to the solar input at the time of interest. The plots are in a geomagnetic frame of reference with Magnetic Local Time (MLT) and geomagnetic latitude as marked in the first plot. The white line represents the location of the Scandinavian radio tomography chain and the white spot is the geographic pole. For each UT the ion density is at the peak height for this time of interest, which is 320km. The latitudinal scale extends from 90°MLAT to 50°MLAT in 10° steps.

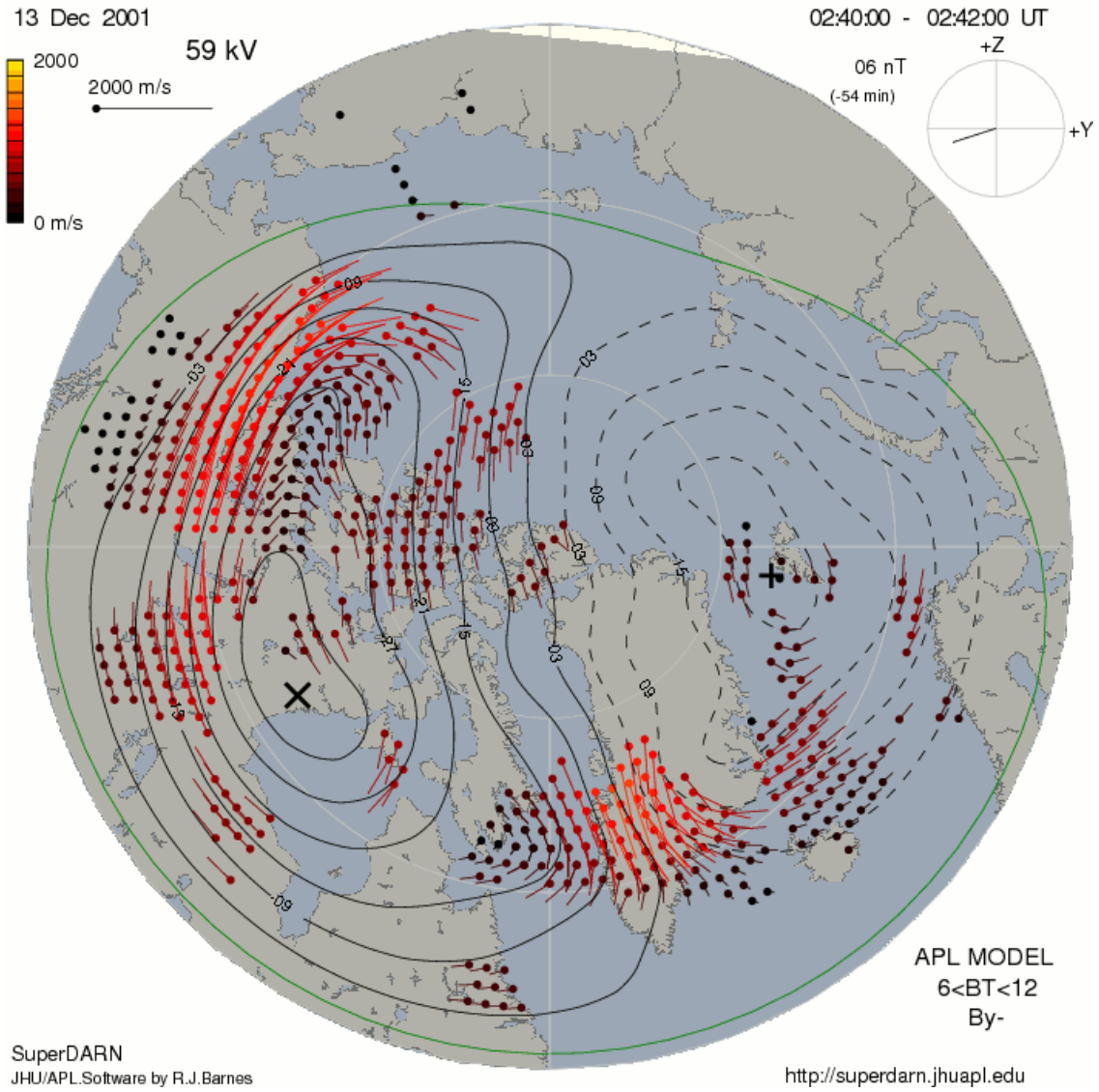

Figure 7.6: Contours of the SuperDARN electric potential pattern for 0240UT on 13 December 2001. The short lines indicate the ionospheric drift velocities measured by the radars with their lengths and colours representing the drift magnitude and their orientations indicating the direction of flow.

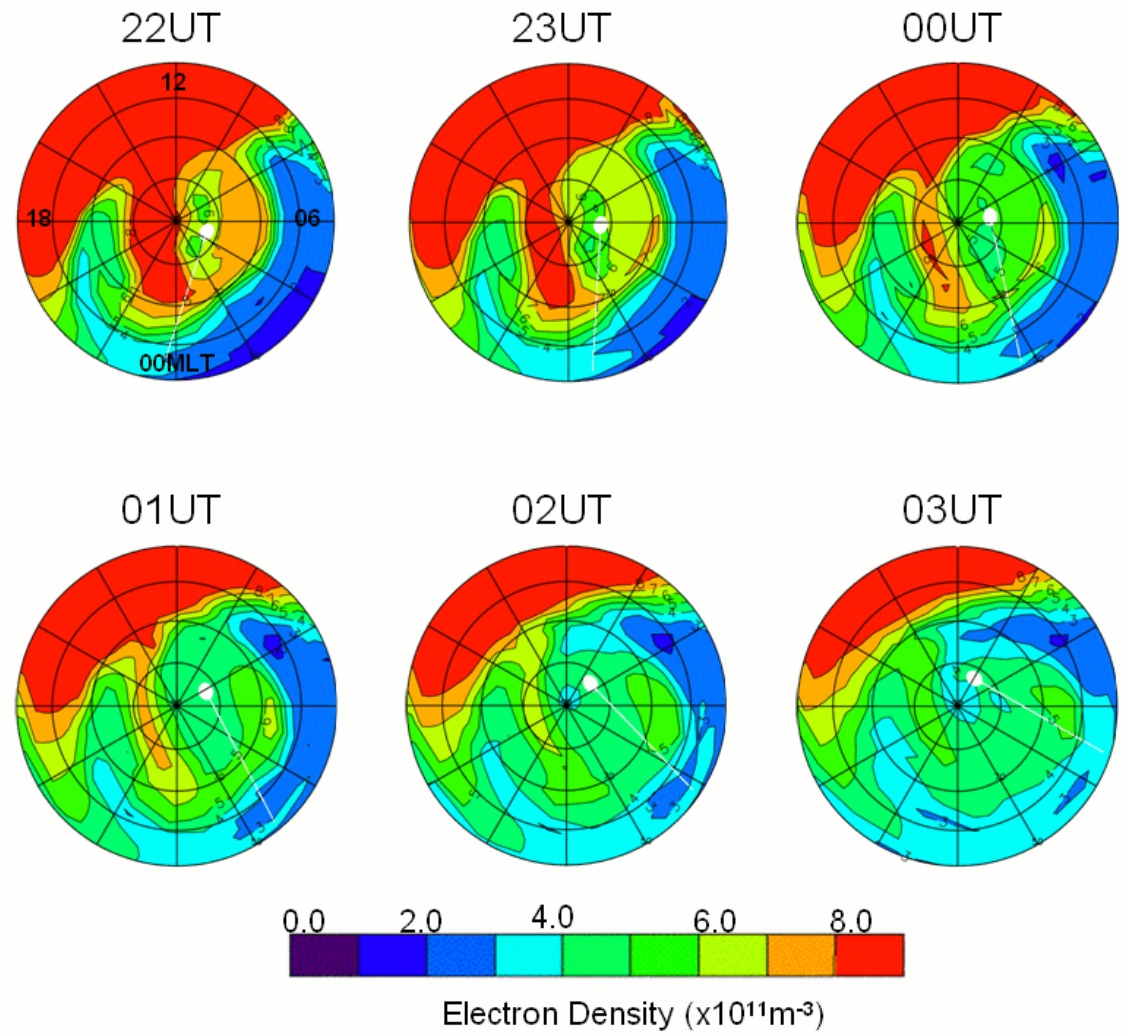

Figure 7.7: CTIP model output for 13 December 2001 showing the electron density due to the solar input at the time of interest. The plots are in a geomagnetic frame of reference with Magnetic Local Time (MLT) and geomagnetic latitude as marked in the first plot. The white line represents the location of the Scandinavian radio tomography chain and the white spot is the geographic pole. For each UT the ion density is at the peak height for this time of interest, which is 320km. The latitudinal scale extends from 90°MLAT to 50°MLAT in 10° steps.

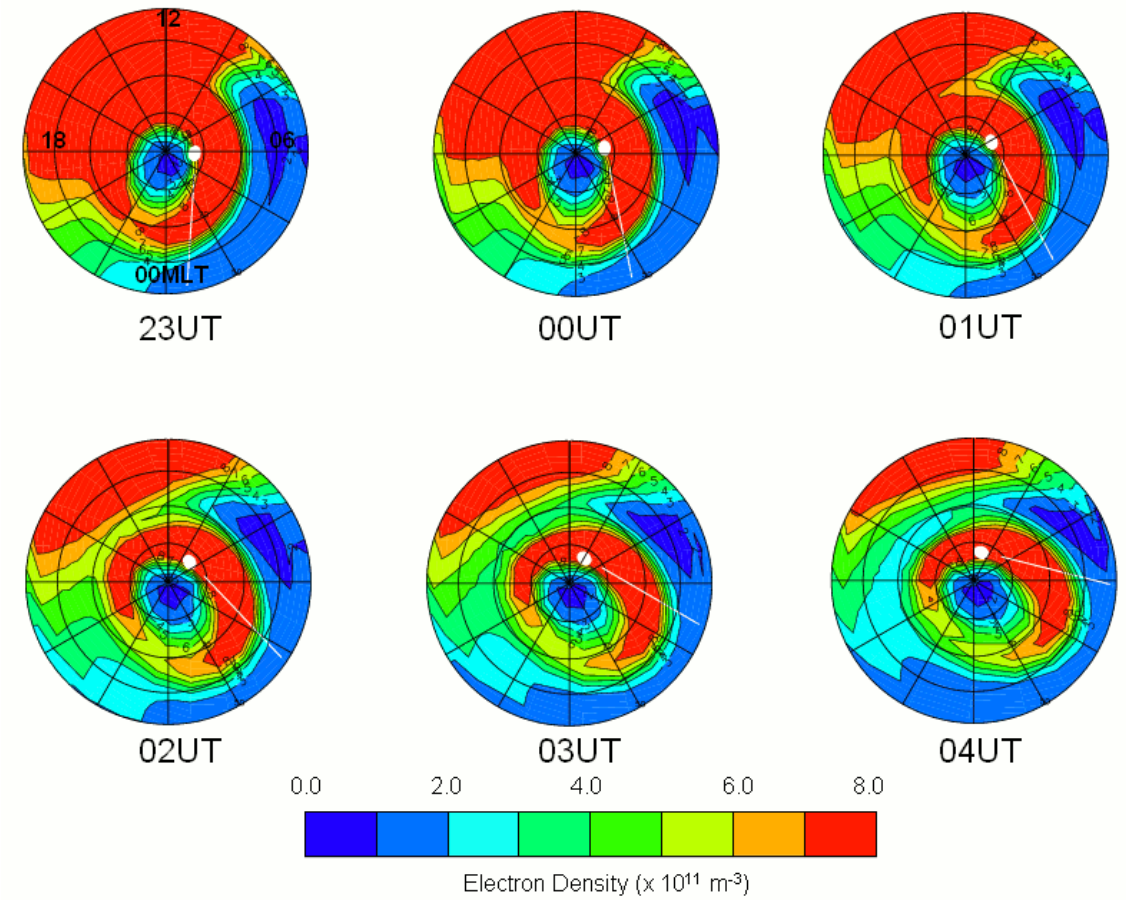

Figure 7.8: CTIP model output for 13 December 2001 showing the electron density due to the solar input and the convection pattern at the time of interest. The plots are in a geomagnetic frame of reference with Magnetic Local Time (MLT) as and geomagnetic latitude as marked in the first plot. The white line represents the location of the Scandinavian radio tomography chain and the white spot is the geographic pole. For each UT the ion density is at the peak height for this time of interest, which is 260km. The latitudinal scale extends from 90°MLAT to 50°MLAT in 10° steps.

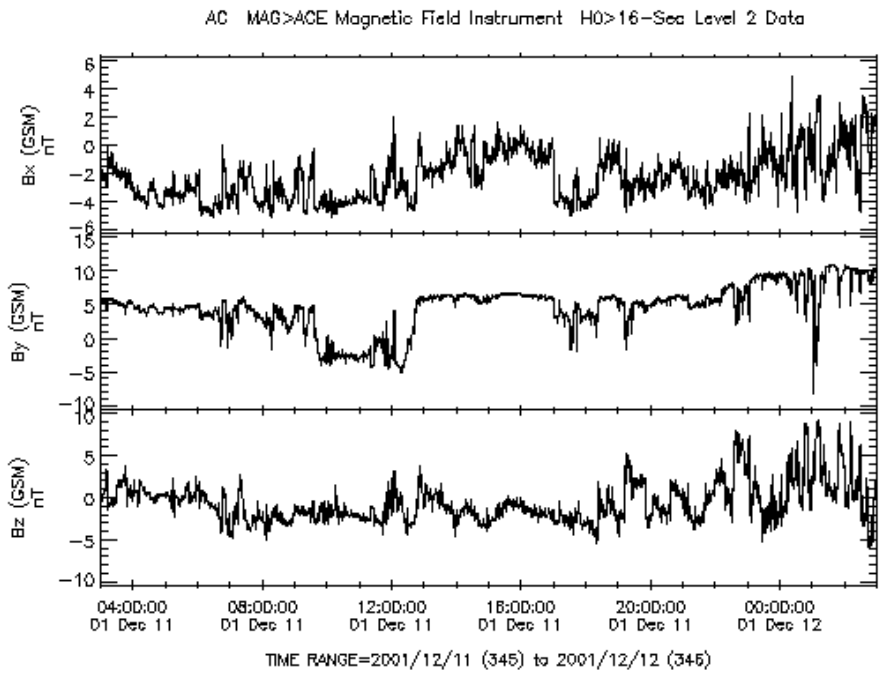

Figure 7.9: ACE plot showing the IMF Bz component to be negative and stable from 03UT on 11 December 2001, 6 hours prior to the time of interest in Alaska. *Data courtesy of N. Ness at Bartol Research Institute and CDAWeb.*

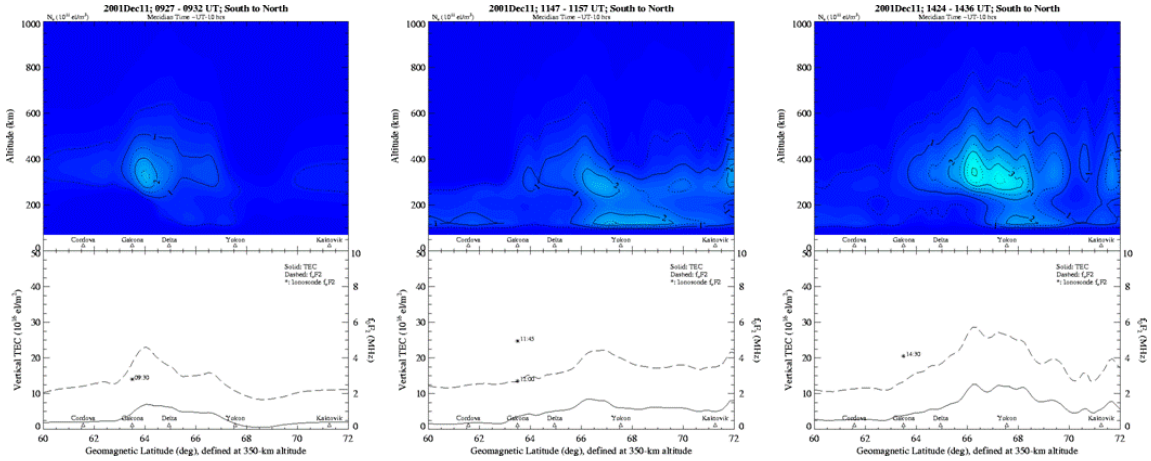

Figure 7.10: IMF Bz negative Alaskan tomography plots from 11 December 2001.

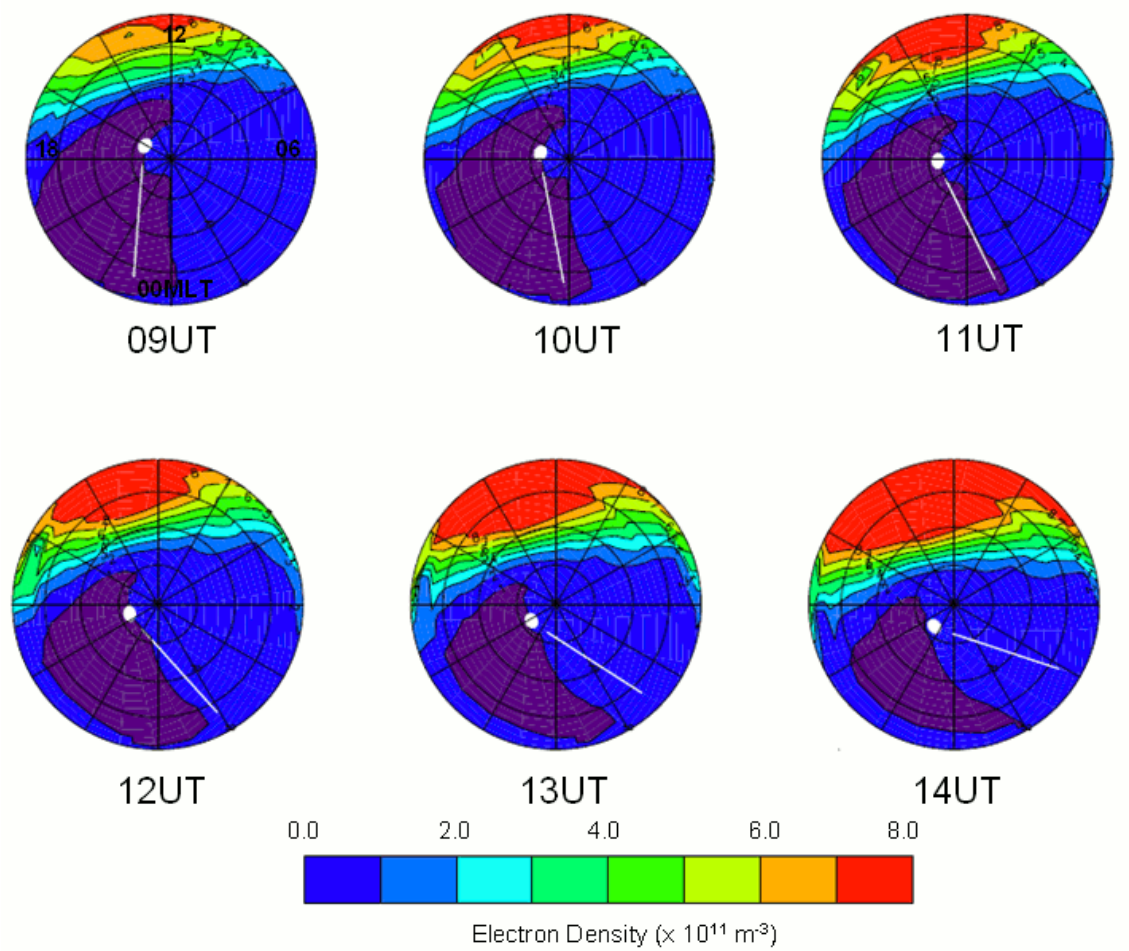

Figure 7.11: CTIP model output for 9-14UT on 11 December 2001 showing the electron density at a peak height of 320km. These plots show only the effect of the solar F10.7 input, which for this day was 230. The white line shows the approximate position of the Alaskan tomography chain. The latitudinal scale extends from 90°MLAT to 50°MLAT in 10° steps.

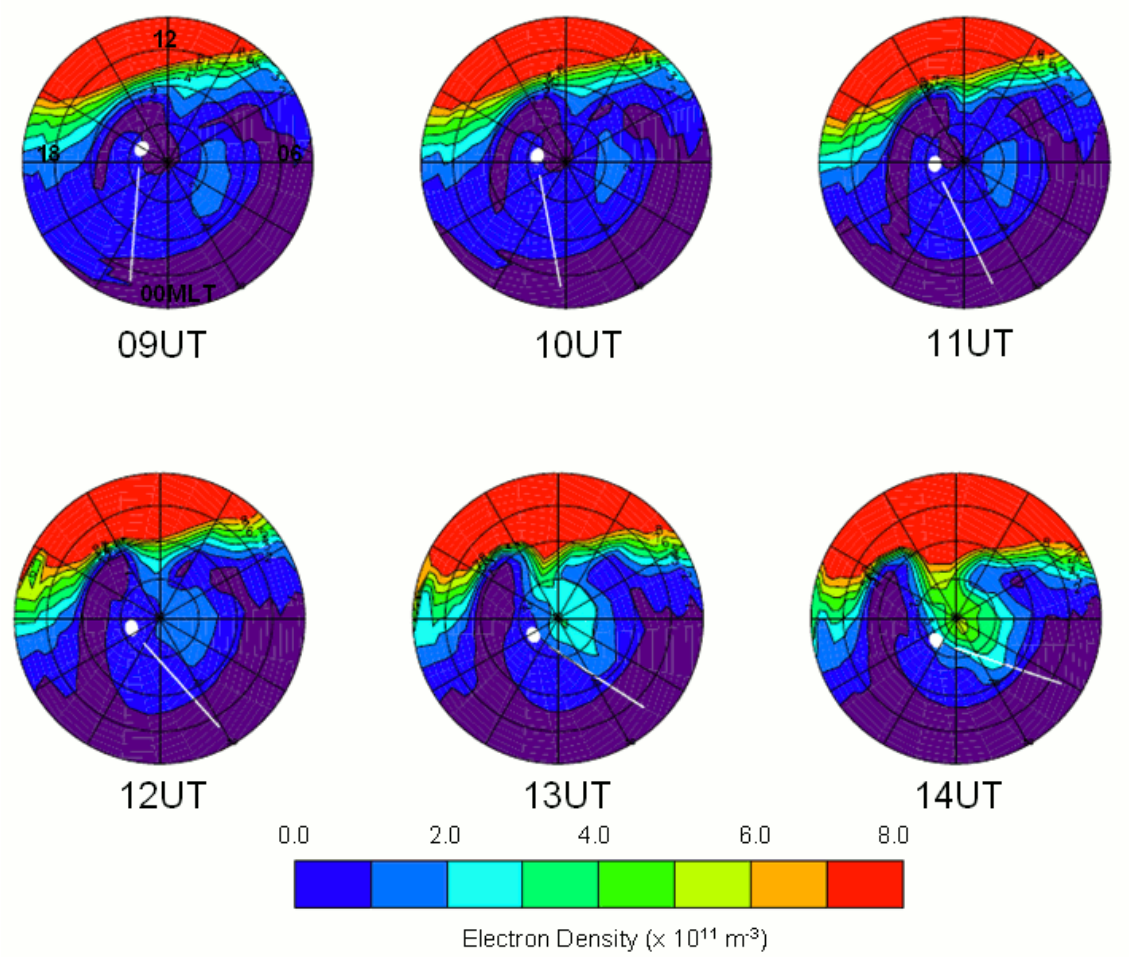

Figure 7.12: CTIP model output for 9-14UT on 11 December 2001 showing the electron density at a peak height of 320km. These plots show the combined effect of the solar F10.7 input, which for this day was 230 and the high-latitude convection input, which was the same SuperDARN pattern as used in the Scandinavian tomography study. The white line on each dial plot shows the approximate position of the Alaskan tomography chain. The latitudinal scale extends from 90°MLAT to 50°MLAT in 10° steps.

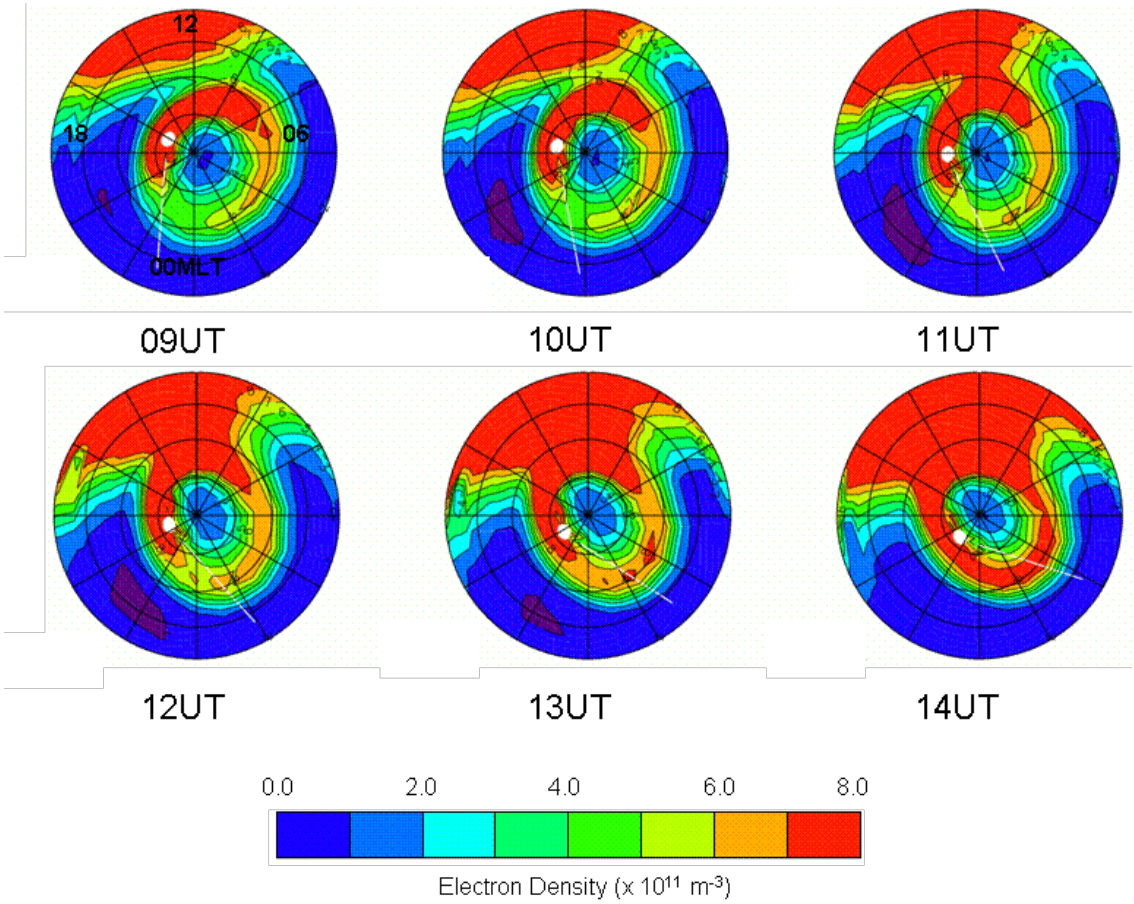

Figure 7.13: CTIP model output for 9-14UT on 11 December 2001 showing the electron density at a peak height of 320km. These plots show the combined effect of the solar F10.7 input, which for this day was 230 and the DMSP precipitation with Kp set to a value of 2. The white line shows the approximate position of the Alaskan tomography chain. The latitudinal scale extends from 90°MLAT to 50°MLAT in 10° steps.

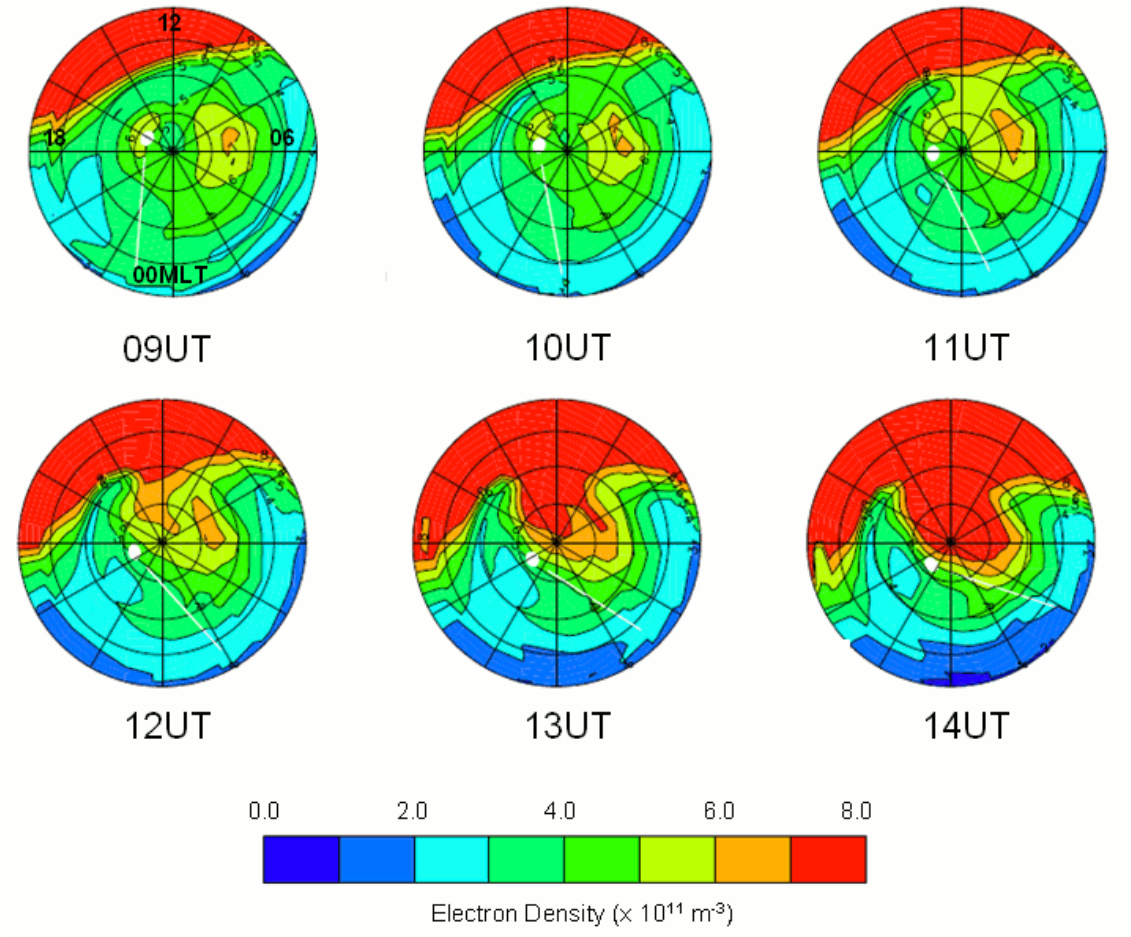

Figure 7.14: CTIP model output for 9-14UT on 11 December 2001 showing the electron density at a peak height of 320km. These plots show the combined effect of the solar F10.7 input, which for this day was 230, the high-latitude convection and the DMSP precipitation with Kp set to a value of 2. The white line shows the approximate position of the Alaskan tomography chain. The latitudinal scale extends from 90°MLAT to 50°MLAT in 10° steps.

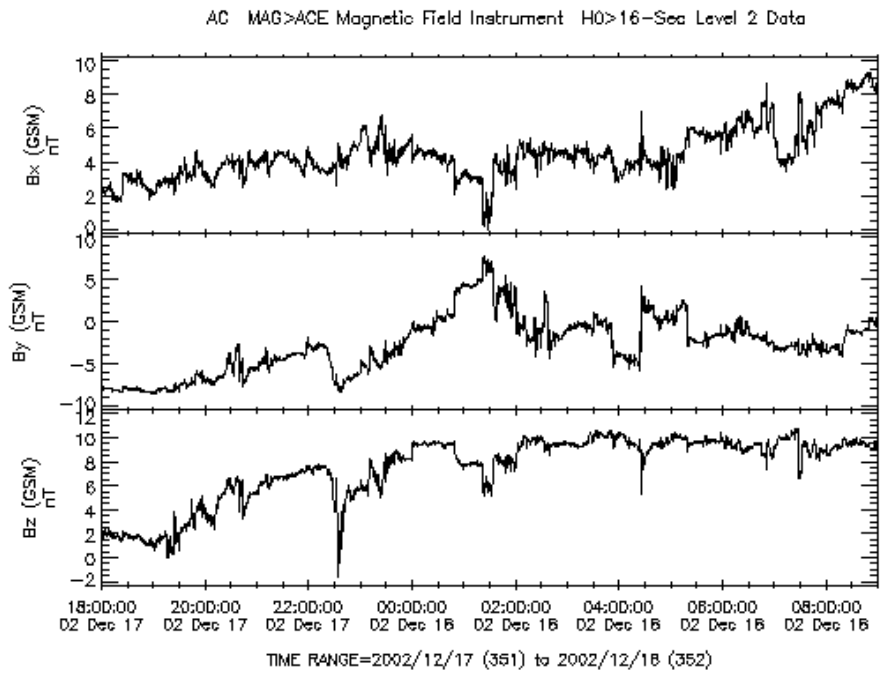

Figure 7.15: ACE plot showing the IMF Bz component to be positive and stable from 18UT on 17 December 2002, 6 hours prior to the time of interest in Scandinavia. *Data courtesy of N. Ness at Bartol Research Institute and CDAWeb.*

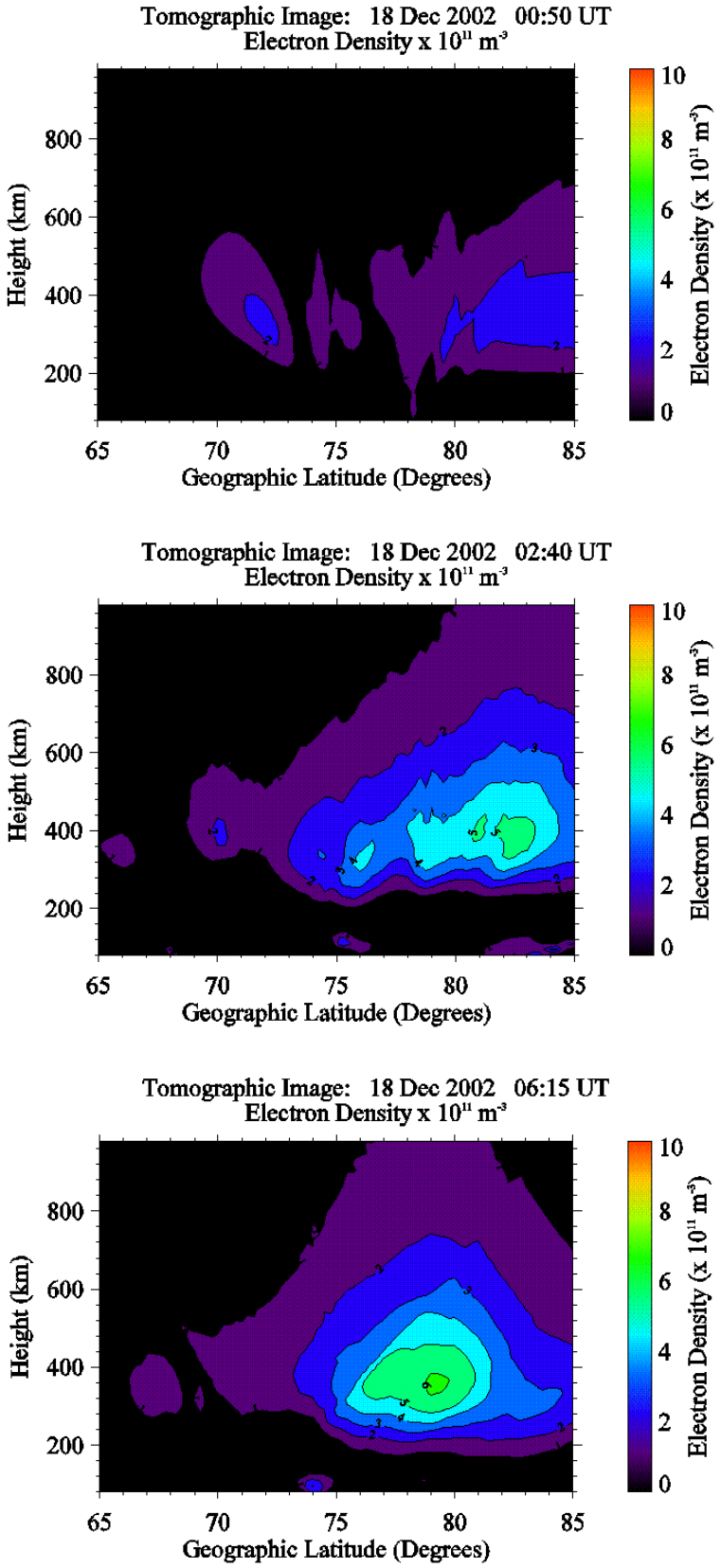

Figure 7.16: IMF Bz positive Scandinavian tomography plots for 0005UT, 0240UT \nx 0615UT on 18 December 2002.

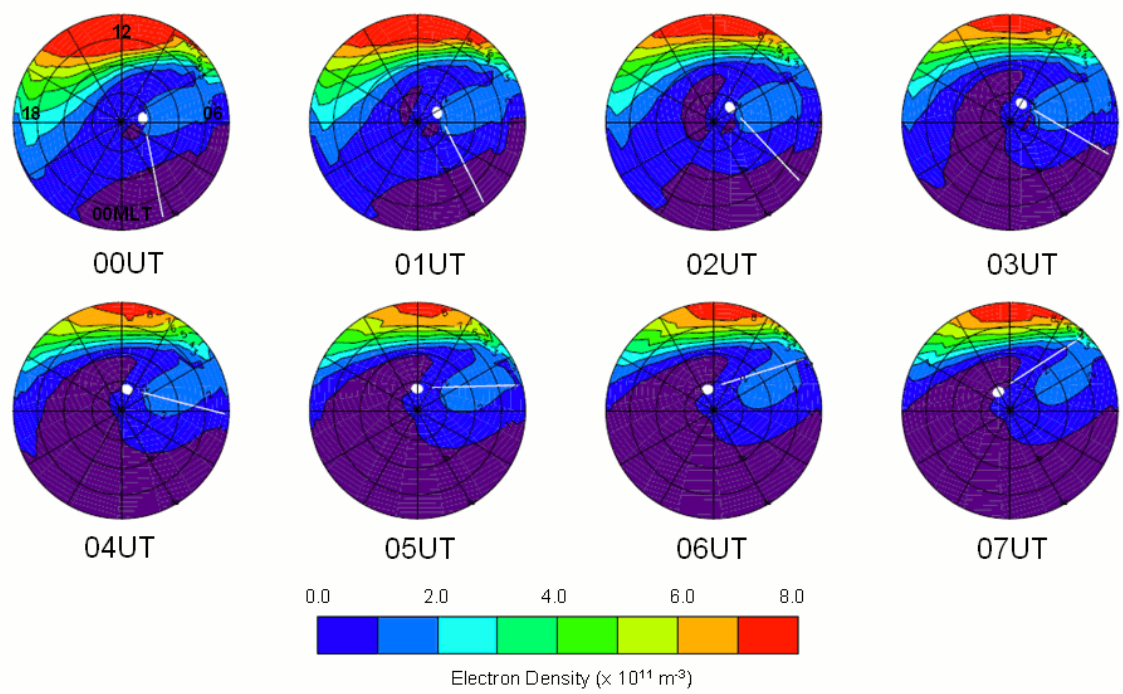

Figure 7.17: CTIP model output for selected UTs from 18 December 2002 showing the effect of the solar input only. The F10.7 value for this day was 190. The white line indicates the approximate location of the Scandinavian tomography chain. The latitudinal scale extends from 90°MLAT to 50°MLAT in 10° steps.

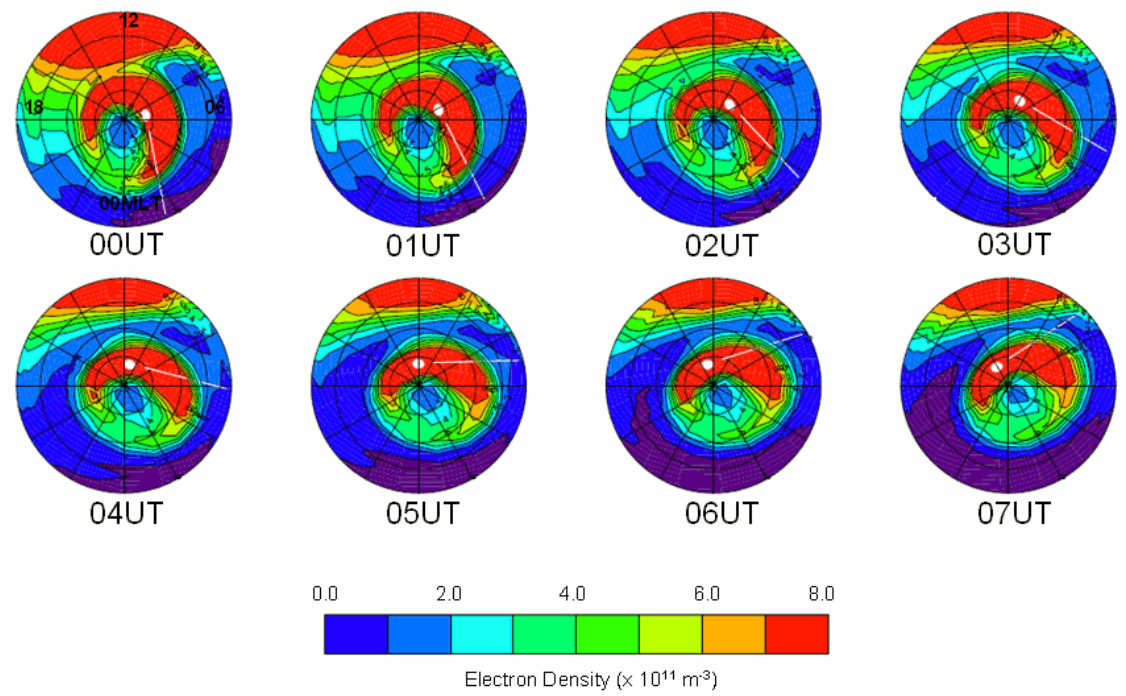

Figure 7.18: CTIP model output for selected UTs from 18 December 2002 showing the effect of the solar input and the DMSP precipitation with a Kp value of 1. The F10.7 value for this day was 190. The white line indicates the approximate location of the Scandinavian tomography chain. The latitudinal scale extends from 90°MLAT to 50°MLAT in 10° steps.

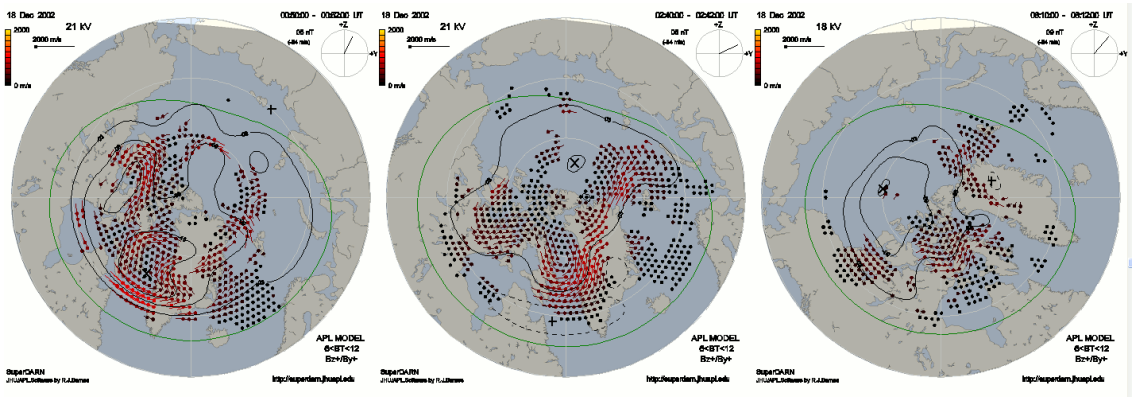

0050UT 0240UT 0615UT

Figure 7.19: IMF Bz positive SuperDARN convection patterns corresponding to the time of each of the three Scandinavian tomography passes.

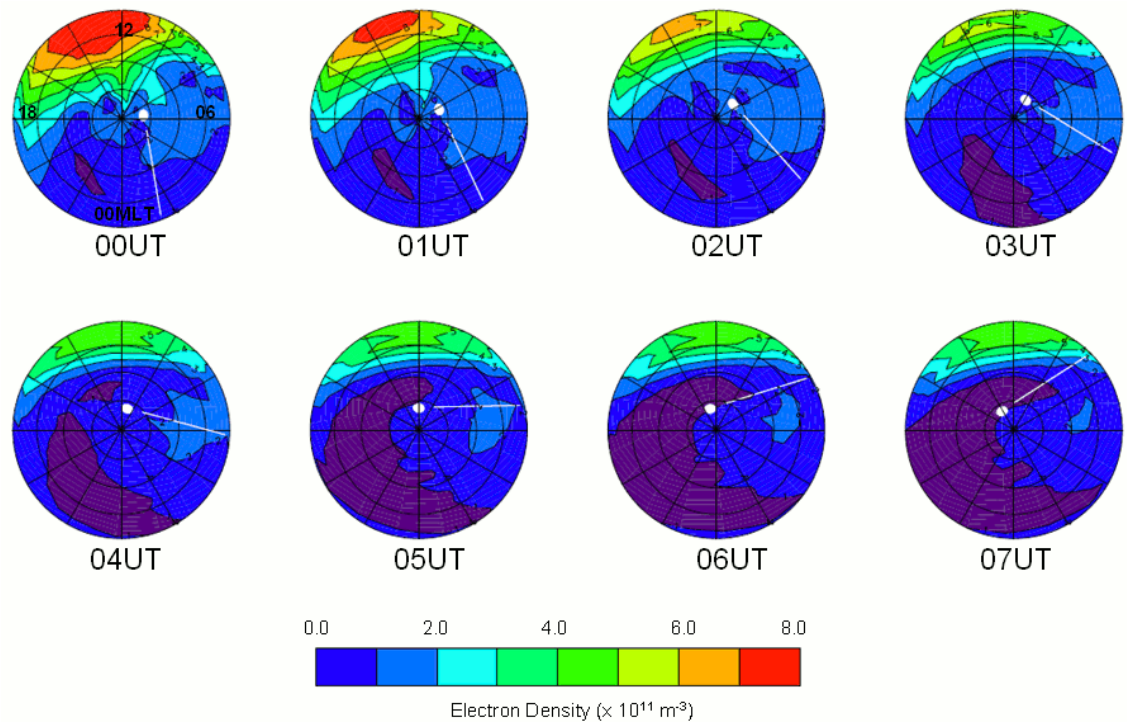

Figure 7.20: CTIP model output for selected UTs from 18 December 2002 showing the effect of the solar input and the 0050UT SuperDARN convection pattern. The F10.7 value for this day was 190. The white line indicates the approximate location of the Scandinavian tomography chain. The latitudinal scale extends from 90°MLAT to 50°MLAT in 10° steps.

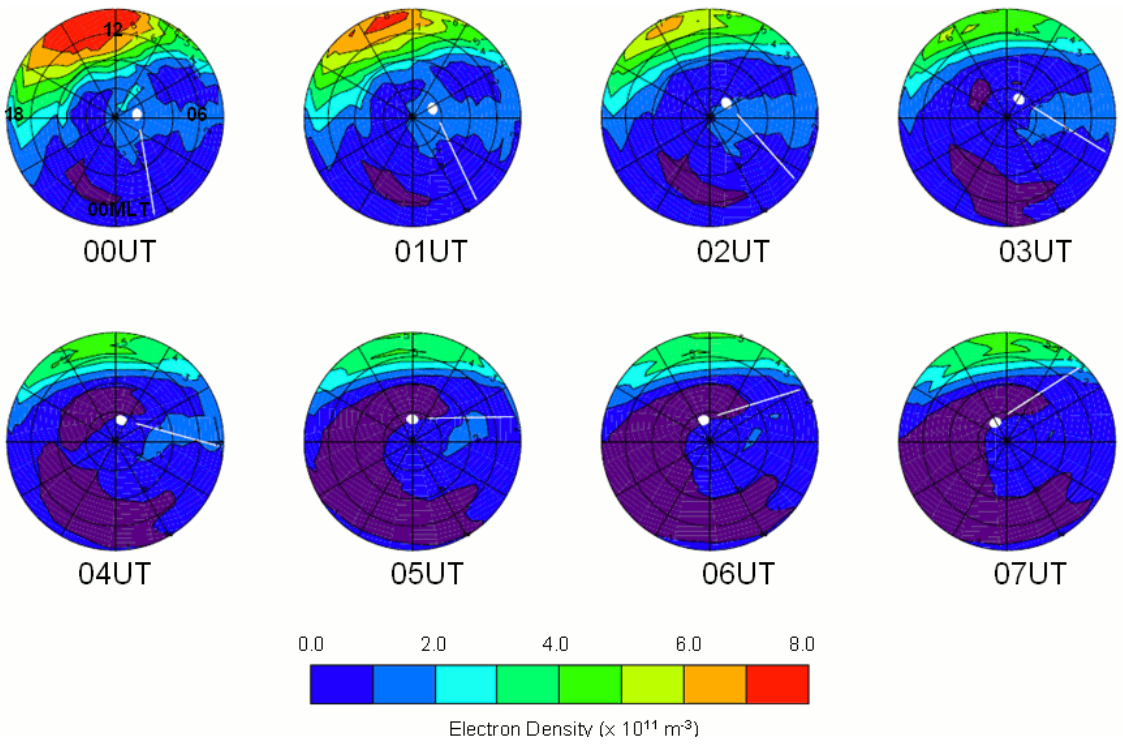

Figure 7.21: CTIP model output for selected UTs from 18 December 2002 showing the effect of the solar input and the 0240UT SuperDARN convection pattern. The F10.7 value for this day was 190. The white line indicates the approximate location of the Scandinavian tomography chain. The latitudinal scale extends from 90°MLAT to 50°MLAT in 10° steps.

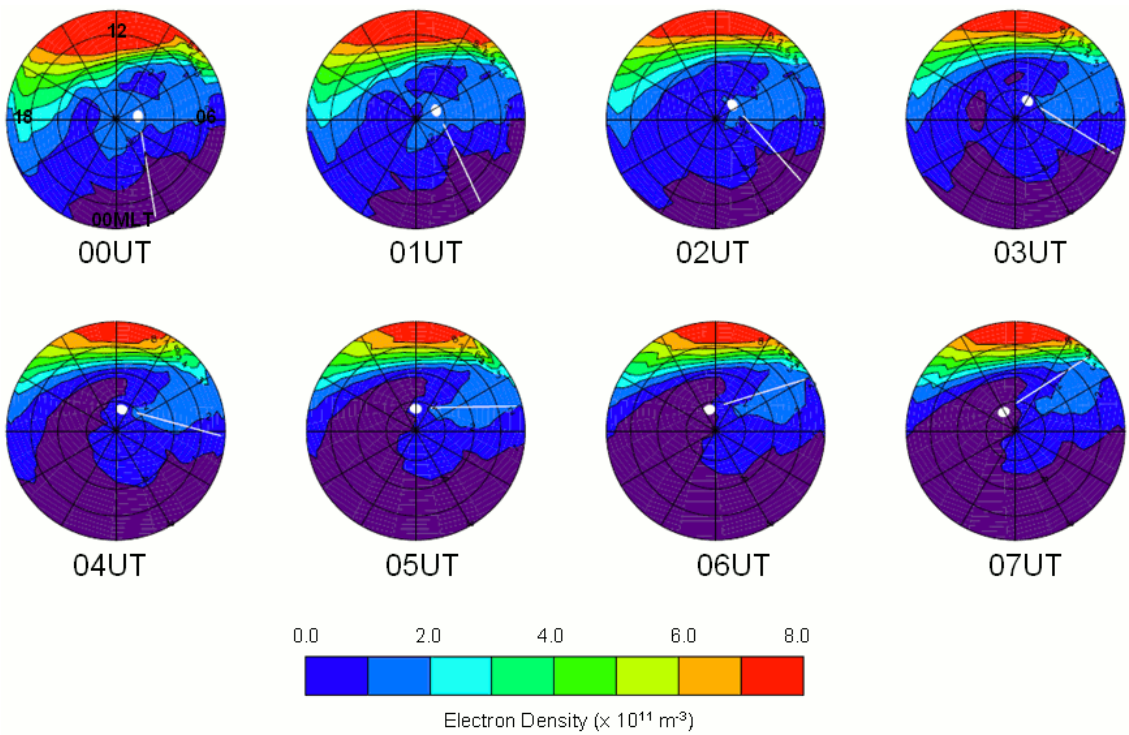

Figure 7.22: CTIP model output for selected UTs from 18 December 2002 showing the effect of the solar input and the 0615UT SuperDARN convection pattern. The F10.7 value for this day was 190. The white line indicates the approximate location of the Scandinavian tomography chain. The latitudinal scale extends from 90°MLAT to 50°MLAT in 10° steps.

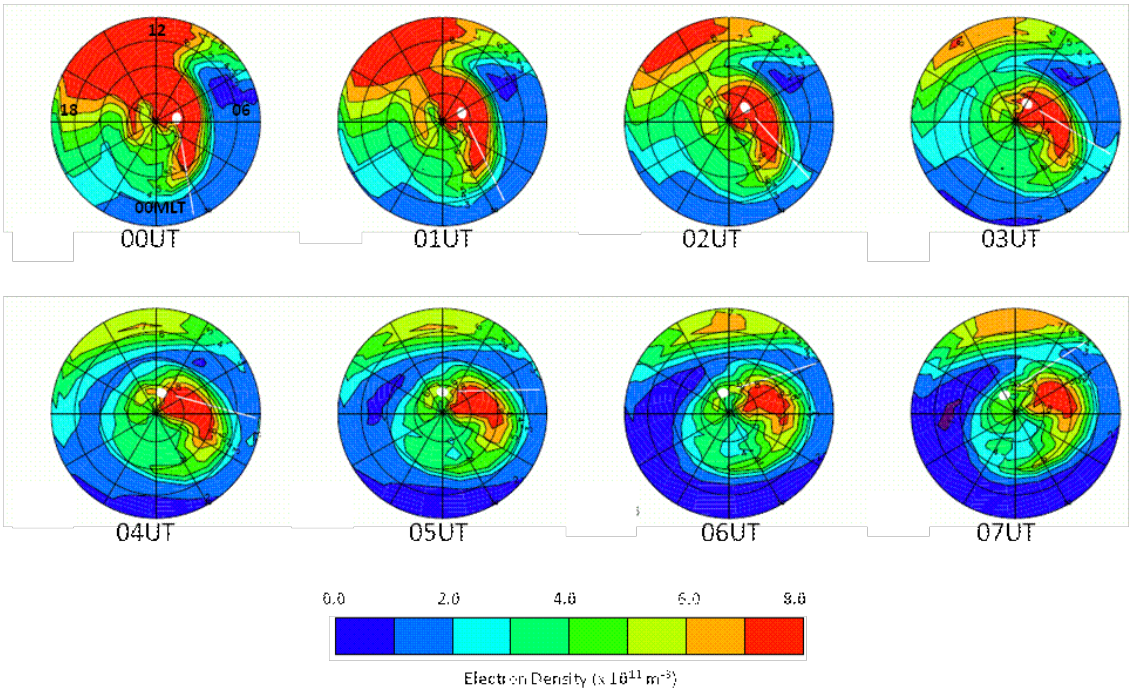

Figure 7.23: CTIP model output for selected UTs from 18 December 2002 showing the effect of the solar input and the 0050UT SuperDARN convection pattern with DMSP precipitation. The F10.7 value for this day was 190 and the Kp value was 1. The white line indicates the approximate location of the Scandinavian tomography chain. The latitudinal scale extends from 90°MLAT to 50°MLAT in 10° steps.

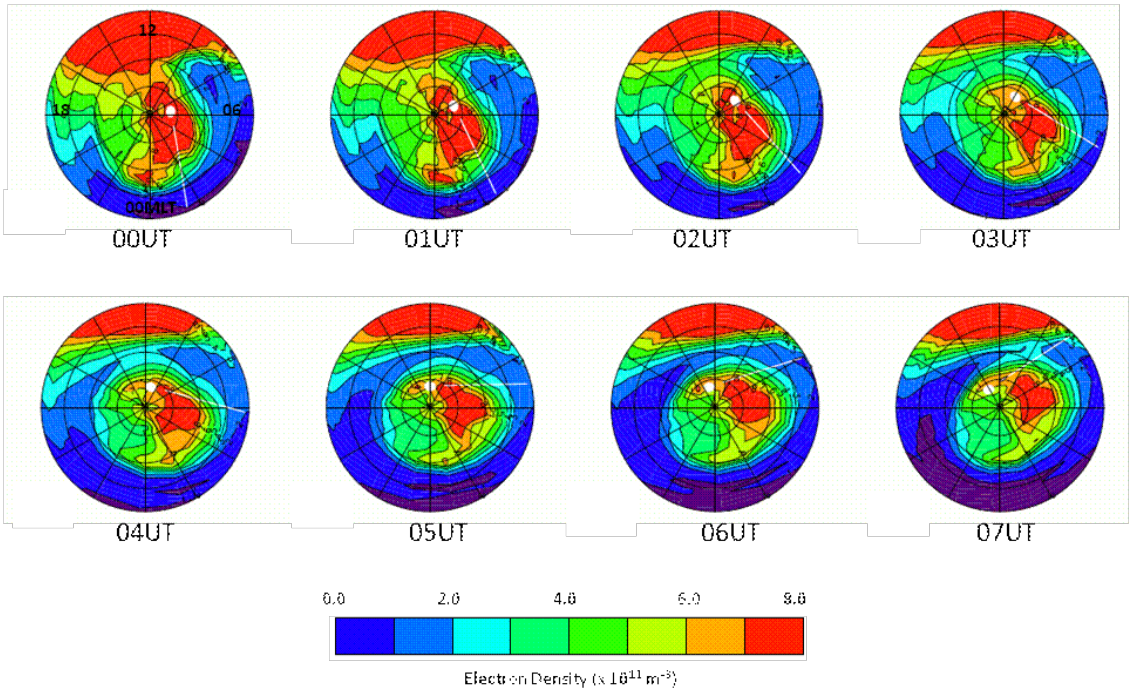

Figure 7.24: CTIP model output for selected UTs from 18 December 2002 showing the effect of the solar input and the 0240UT SuperDARN convection pattern with DMSP precipitation. The F10.7 value for this day was 190 and the Kp value was 1. The white line indicates the approximate location of the Scandinavian tomography chain. The latitudinal scale extends from 90°MLAT to 50°MLAT in 10° steps.

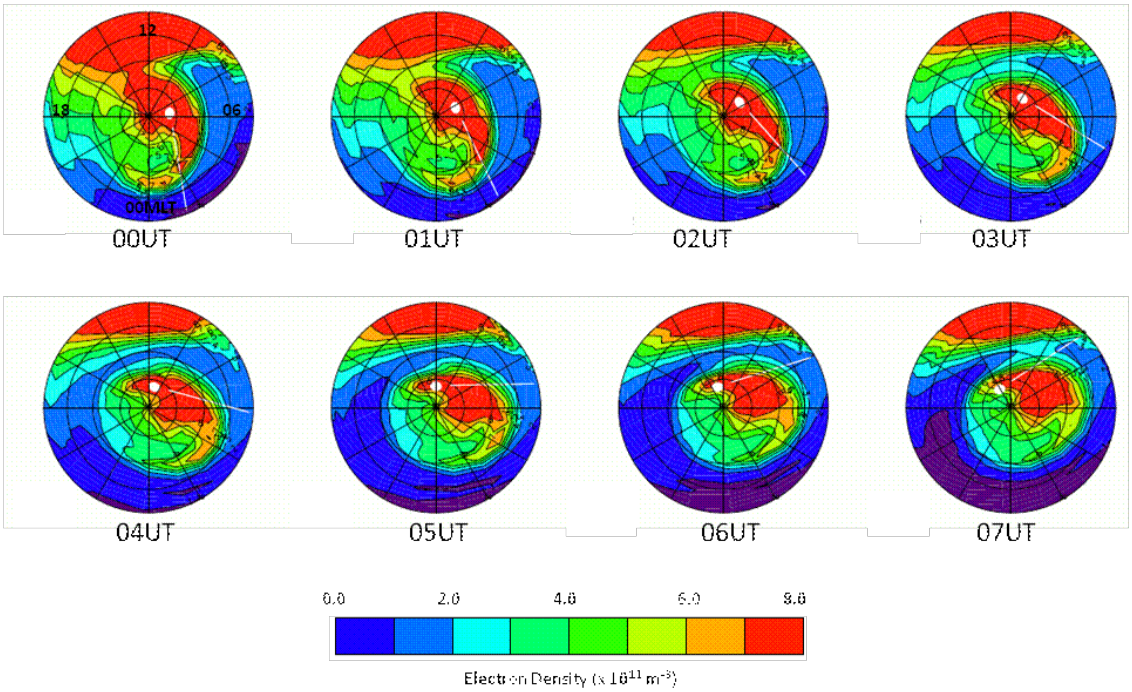

Figure 7.25: CTIP model output for selected UTs from 18 December 2002 showing the effect of the solar input and the 0615UT SuperDARN convection pattern with DMSP precipitation. The F10.7 value for this day was 190 and the Kp value was 1. The white line indicates the approximate location of the Scandinavian tomography chain. The latitudinal scale extends from 90°MLAT to 50°MLAT in 10° steps.

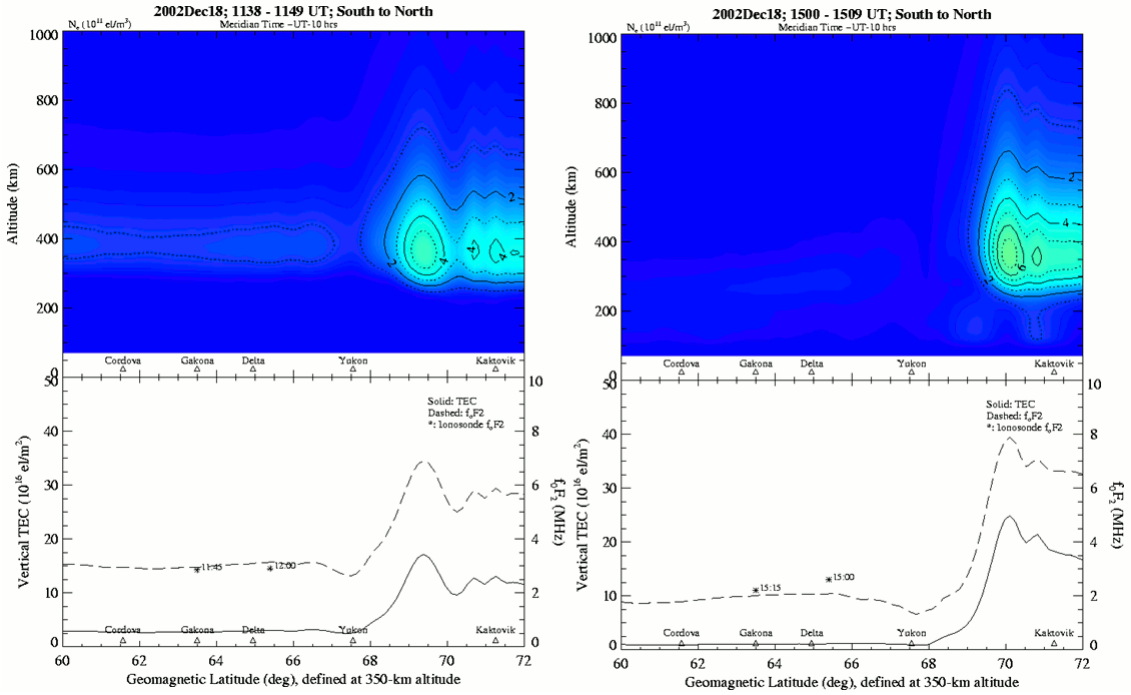

1138UT 1500UT

Figure 7.26: IMF Bz positive Alaskan tomography plots from 18 December 2001.

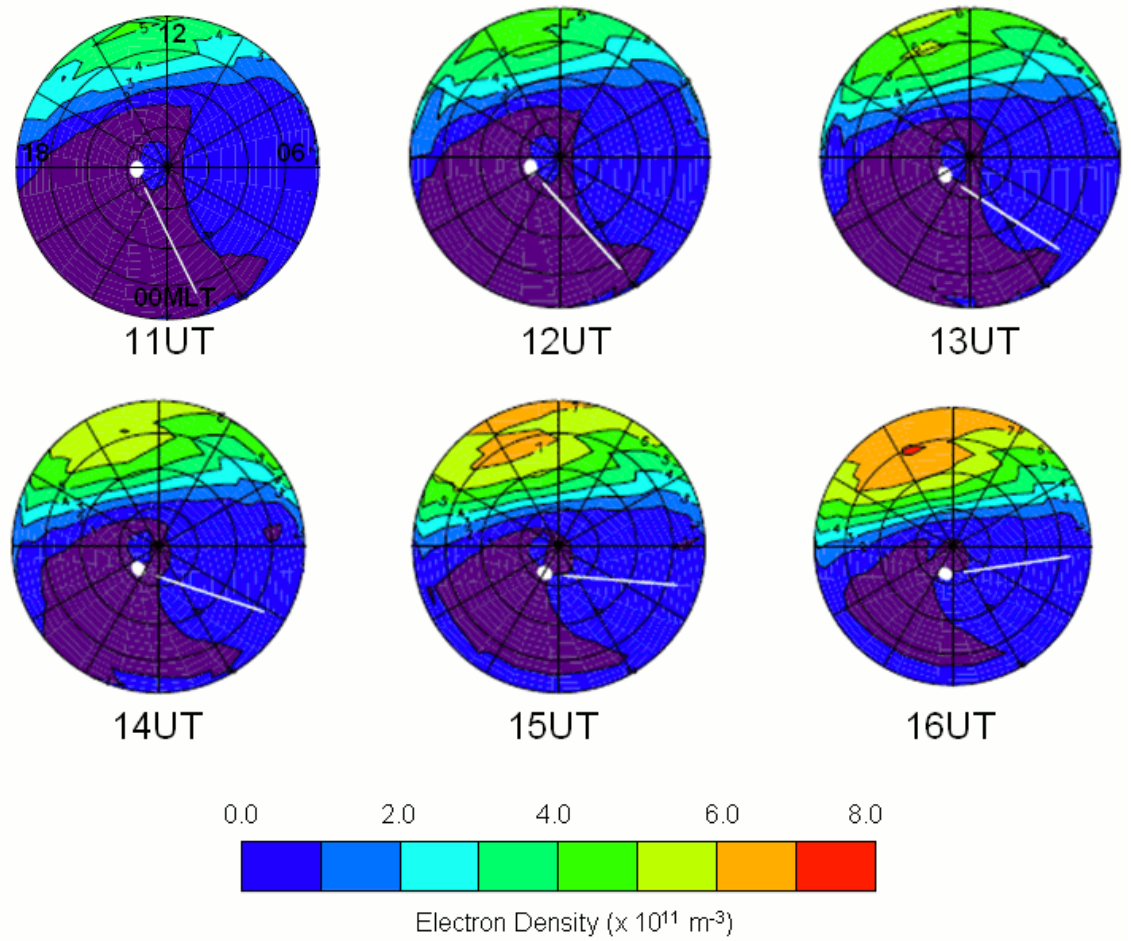

Figure 7.27: CTIP model output for 18 December 2002 showing the effect of the solar input with the Alaskan chain line marked in white. The F10.7 value for this day is 190. The latitudinal scale extends from 90°MLAT to 50°MLAT in 10° steps.

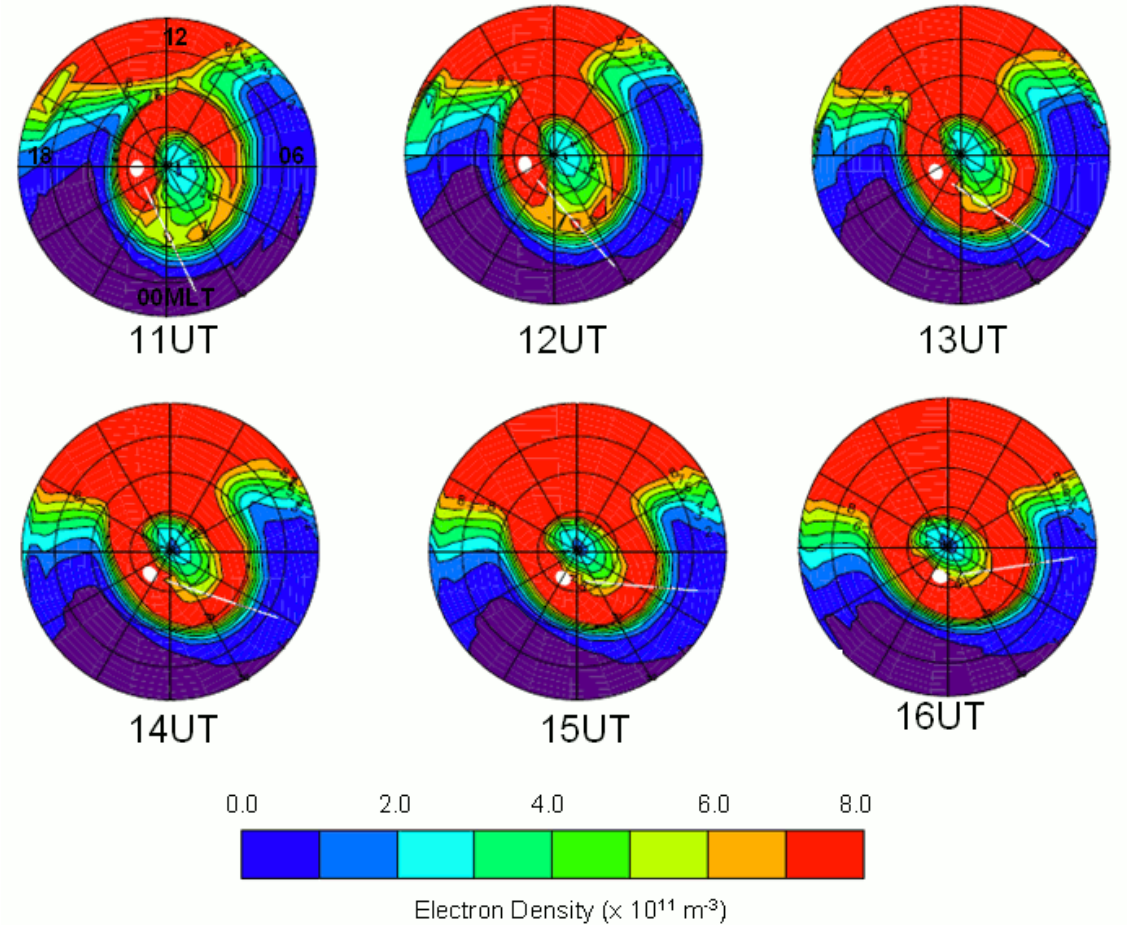

Figure 7.28: CTIP model output for 18 December 2002 showing the effect of the solar input and DMPS precipitation with Kp=1. The Alaskan chain line is marked by the white line. The F10.7 value for this day is 190. The latitudinal scale extends from 90°MLAT to 50°MLAT in 10° steps.

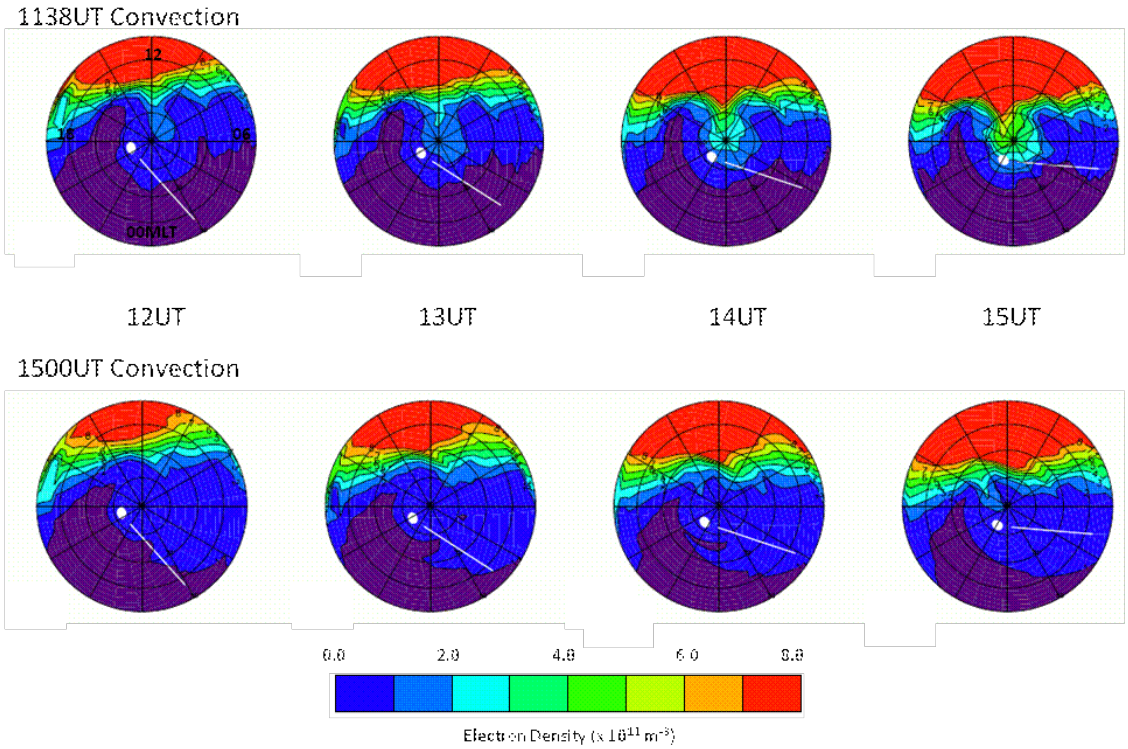

Figure 7.29: CTIP model output for 18 December 2002 showing the effect of the solar input and the corresponding SuperDARN convection pattern for each of the tomography images. The Alaskan chain line marked in white. The F10.7 value for this day is 190. The latitudinal scale extends from 90°MLAT to 50°MLAT in 10° steps.

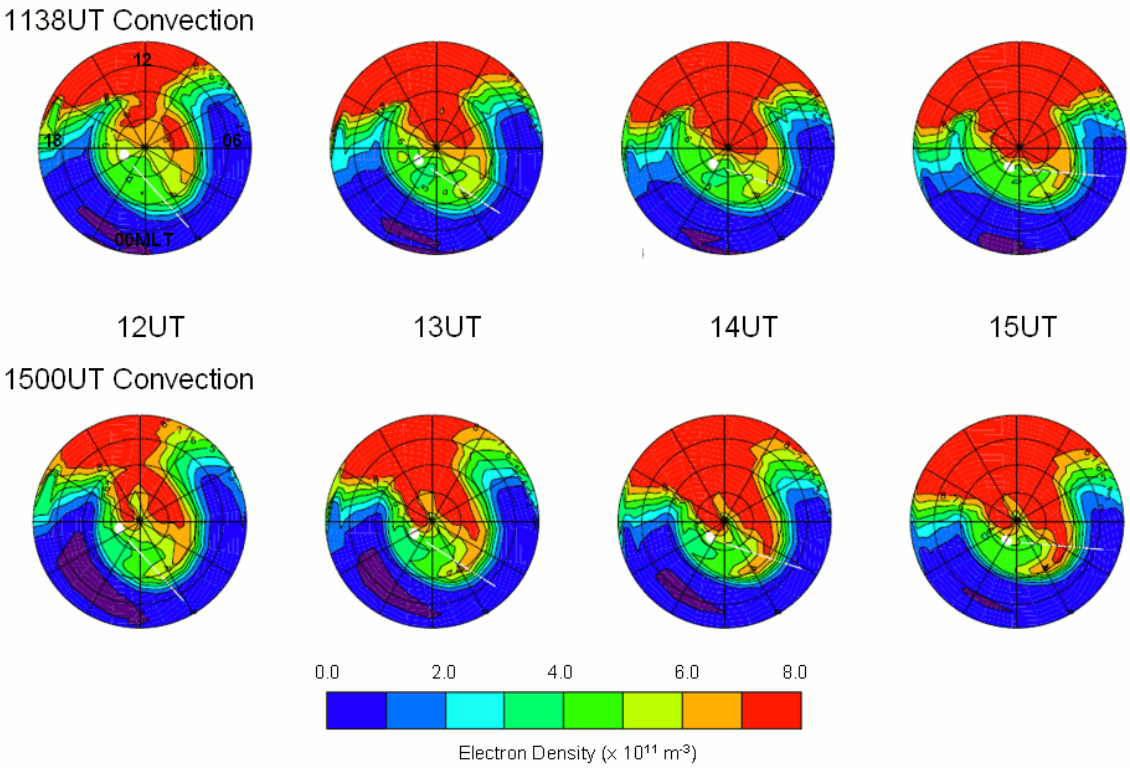

Figure 7.30: CTIP model output for 18 December 2002 showing the effect of the solar input, DMSP precipitation (Kp=1) and the corresponding SuperDARN convection pattern for each of the tomography images. The Alaskan chain line marked in white. The F10.7 value for this day is 190. The latitudinal scale extends from 90°MLAT to 50°MLAT in 10° steps.